

# Simultaneous Measurement of Oscillation Parameters in Beam and Atmospheric Neutrino Data from Tokai-to-Kamioka and Super-Kamiokande Experiments

# Daniel Robert Clement Barrow

# Magdalen College, Oxford University

<sup>10</sup> A Dissertation Submitted to Oxford University

<sup>11</sup> for the Degree of Doctor of Philosophy

<sup>12</sup>

13                   **Simultaneous Measurement of**

14                   **Oscillation Parameters in Beam and**

15                   **Atmospheric Neutrino Data from**

16                   **Tokai-to-Kamioka and**

17                   **Super-Kamiokande Experiments**

18                   *Abstract*

19                   Lorem ipsum dolor sit amet, consectetur adipiscing elit, sed do eiusmod tempor incididunt ut labore et dolore magna aliqua. Nulla aliquet porttitor lacus luctus accumsan tortor posuere. Pulvinar neque laoreet suspendisse interdum. Sem viverra aliquet eget sit. Nunc sed velit dignissim sodales ut eu sem integer vitae. At erat pellentesque adipiscing commodo elit at imperdiet dui accumsan. Fames ac turpis egestas integer eget aliquet nibh. Scelerisque eu ultrices vitae auctor eu augue. Purus non enim praesent elementum facilisis leo vel. Sollicitudin nibh sit amet commodo. Vitae auctor eu augue ut. Vel quam elementum pulvinar etiam. A condimentum vitae sapien pellentesque habitant morbi tristique senectus. Viverra accumsan in nisl nisi scelerisque eu ultrices. Sed viverra ipsum nunc aliquet bibendum enim. Sit amet purus gravida quis. In vitae turpis massa

<sup>32</sup> sed elementum tempus egestas sed sed. Vivamus arcu felis bibendum  
<sup>33</sup> ut tristique et egestas. Senectus et netus et malesuada fames ac turpis.  
<sup>34</sup> Ac auctor augue mauris augue.

## 35 Declaration

36 This dissertation is the result of my own work, except where ex-  
37 plicit reference is made to the work of others, and has not been sub-  
38 mitted for another qualification to this or any other university. This  
39 dissertation does not exceed the word limit for the respective Degree  
40 Committee.

41 Daniel Robert Clement Barrow

42 ©The copyright of this thesis rests with the author and is made available under a Creative  
43 Commons Attribution Non-Commercial No Derivatives licence. Researchers are free to copy,  
44 distribute or transmit the thesis on the condition that they attribute it, that they do not use  
45 it for commercial purposes and that they do not alter, transform or build upon it. For any  
46 reuse or redistribution, researchers must make clear to others the licence terms of this work.

47

## Acknowledgements

48 at pretium nibh ipsum. Eget nunc scelerisque viverra mauris in aliquam. Arcu vitae  
49 elementum curabitur vitae nunc sed velit dignissim. Sed arcu non odio euismod lacinia  
50 at quis risus sed. Vitae tempus quam pellentesque nec nam aliquam sem et tortor.  
51 Viverra aliquet eget sit amet tellus cras adipiscing. Purus sit amet luctus venenatis  
52 lectus magna. In aliquam sem fringilla ut morbi tincidunt augue. Fermentum dui  
53 faucibus in ornare. Aliquam malesuada bibendum arcu vitae elementum curabitur  
54 vitae nunc sed.

55 Ultricies leo integer malesuada nunc vel risus commodo. Tellus cras adipiscing  
56 enim eu turpis egestas pretium. Dictumst quisque sagittis purus sit amet volutpat  
57 consequat mauris nunc. Vitae congue mauris rhoncus aenean vel elit scelerisque  
58 mauris pellentesque. Vel facilisis volutpat est velit egestas dui id ornare. Suscipit  
59 adipiscing bibendum est ultricies. At in tellus integer feugiat scelerisque varius  
60 morbi enim. Cras semper auctor neque vitae tempus. Commodo sed egestas egestas  
61 fringilla phasellus faucibus. Cras pulvinar mattis nunc sed blandit. Pretium viverra  
62 suspendisse potenti nullam ac tortor vitae. Purus sit amet volutpat consequat. Orci  
63 sagittis eu volutpat odio facilisis mauris. Sit amet massa vitae tortor condimentum  
64 lacinia quis. Commodo sed egestas egestas fringilla phasellus. Sed libero enim sed  
65 faucibus turpis. Vitae tempus quam pellentesque nec.

66 Blandit massa enim nec dui. Viverra tellus in hac habitasse platea dictumst vestibulu-  
67 lum. Bibendum enim facilisis gravida neque convallis. Sagittis nisl rhoncus mattis  
68 rhoncus urna neque. Nisl rhoncus mattis rhoncus urna neque. Ac tortor vitae purus  
69 faucibus ornare. Aenean sed adipiscing diam donec adipiscing tristique risus. Sapien  
70 nec sagittis aliquam malesuada bibendum. Et leo duis ut diam quam nulla. Tellus  
71 rutrum tellus pellentesque eu tincidunt tortor aliquam nulla facilisi. Fermentum leo

<sup>72</sup> vel orci porta non pulvinar neque. Eget sit amet tellus cras adipiscing enim eu. Sed  
<sup>73</sup> viverra tellus in hac habitasse platea dictumst vestibulum.

<sup>74</sup> Sit amet consectetur adipiscing elit. At varius vel pharetra vel turpis nunc eget  
<sup>75</sup> lorem. Elit scelerisque mauris pellentesque pulvinar pellentesque habitant morbi  
<sup>76</sup> tristique senectus. Odio euismod lacinia at quis risus sed vulputate odio. Vitae suscipit  
<sup>77</sup> tellus mauris a diam maecenas sed enim ut. Dignissim convallis aenean et tortor at  
<sup>78</sup> risus viverra. Diam sollicitudin tempor id eu. Erat velit scelerisque in dictum. Blandit  
<sup>79</sup> cursus risus at ultrices. Ac tortor vitae purus faucibus ornare suspendisse sed.

# **Contents**

81	<b>1 Neutrino Oscillation Physics</b>	1
82	1.1 Discovery of Neutrinos . . . . .	1
83	1.2 Theory of Neutrino Oscillation . . . . .	3
84	1.2.1 Three Flavour Oscillations . . . . .	3
85	1.2.2 The MSW Effect . . . . .	7
86	1.3 Neutrino Oscillation Measurements . . . . .	9
87	1.3.1 Solar Neutrinos . . . . .	9
88	1.3.2 Atmospheric Neutrinos . . . . .	12
89	1.3.3 Accelerator Neutrinos . . . . .	15
90	1.3.4 Reactor Neutrinos . . . . .	18
91	1.4 Summary . . . . .	19
92	<b>2 T2K and SK Experiment Overview</b>	22
93	2.1 The Super-Kamiokande Experiment . . . . .	23
94	2.1.1 The SK Detector . . . . .	24
95	2.1.2 Calibration . . . . .	27
96	2.1.3 Data Acquisition and Triggering . . . . .	30
97	2.1.4 Cherenkov Radiation . . . . .	32
98	2.2 The Tokai to Kamioka Experiment . . . . .	34
99	2.2.1 The Neutrino Beam . . . . .	35
100	2.2.2 The Near Detector at 280m . . . . .	40
101	2.2.2.1 Fine Grained Detectors . . . . .	42
102	2.2.2.2 Time Projection Chambers . . . . .	43
103	2.2.2.3 $\pi^0$ Detector . . . . .	44
104	2.2.2.4 Electromagnetic Calorimeter . . . . .	46

105	2.2.2.5 Side Muon Range Detector . . . . .	47
106	2.2.3 The Interactive Neutrino GRID . . . . .	47
107	<b>3 Bayesian Statistics and Markov Chain Monte Carlo Techniques</b>	50
108	3.1 Bayesian Statistics . . . . .	51
109	3.2 Monte Carlo Simulation . . . . .	53
110	3.2.1 Markov Chain Monte Carlo . . . . .	54
111	3.2.2 Metropolis-Hastings Algorithm . . . . .	57
112	3.2.3 MCMC Optimisation . . . . .	58
113	3.3 Understanding the MCMC Results . . . . .	62
114	3.3.1 Marginalisation . . . . .	62
115	3.3.2 Parameter Estimation and Credible Intervals . . . . .	64
116	3.3.3 Bayesian Model Comparisons . . . . .	65
117	3.3.4 Comparison of MCMC Output to Expectation . . . . .	67
118	<b>4 Simulation, Reconstruction and Event Selections</b>	69
119	4.1 Simulation . . . . .	69
120	4.2 Event Reconstruction at SK . . . . .	74
121	4.3 Event Selection at SK . . . . .	84
122	<b>5 Oscillation Probability Calculation</b>	89
123	5.1 Overview . . . . .	90
124	5.2 Treatment of Fast Oscillations . . . . .	97
125	5.3 Calculation Engine . . . . .	106
126	5.4 Matter Density Profile . . . . .	107
127	5.5 Production Height Averaging . . . . .	114
128	<b>Bibliography</b>	118
129	<b>List of Figures</b>	129





<sup>132</sup> **Chapter 1**

<sup>133</sup> **Neutrino Oscillation Physics**

<sup>134</sup> When first proposed, neutrinos were expected to be massless fermions that only in-  
<sup>135</sup> teract through weak and gravitational forces. This meant they were very difficult to  
<sup>136</sup> detect as they can pass through significant amounts of matter without interacting. De-  
<sup>137</sup> spite this, experimental neutrino physics has developed with many different detection  
<sup>138</sup> techniques and neutrino sources being used today. In direct tension with **the** standard  
<sup>139</sup> model physics, neutrinos have been determined to oscillate between different lepton  
<sup>140</sup> flavours, requiring them to have mass.

<sup>141</sup> **The observation techniques which lead to the discovery of the neutrino are doc-**  
<sup>142</sup> **umented in section 1.1.** The theory underpinning neutrino oscillation is described in  
<sup>143</sup> section 1.2. This section includes the approximations which can be made to simplify  
<sup>144</sup> the understanding of neutrino oscillation in a two-flavour approximation as well  
<sup>145</sup> as how the medium in which neutrinos propagate can manipulate the oscillation  
<sup>146</sup> probability. **Past**, current, and future neutrino experiments are detailed in section 1.3,  
<sup>147</sup> including the reactor, atmospheric, and long-baseline accelerator neutrino sources that  
<sup>148</sup> have been used to successfully constrain oscillation **parameters determination**.

<sup>149</sup> **1.1 Discovery of Neutrinos**

<sup>150</sup> At the start of the 20<sup>th</sup> century, the electrons emitted from the  $\beta$ -decay of the nucleus  
<sup>151</sup> were found to have a continuous energy spectrum [1,2]. This observation seemingly  
<sup>152</sup> broke the energy conservation invoked within that period's nuclear models. Postulated

in 1930 by Pauli as the solution to this problem, the neutrino (originally termed “neutron”) was theorized to be an electrically neutral spin-1/2 fermion with a mass of the same order of magnitude as the electron [3]. This neutrino was to be emitted with the electron in  $\beta$ -decay to alleviate the apparent breaking of energy conservation. As a predecessor of **the today's** weak interaction model, Fermi's theory of  $\beta$ -decay developed the understanding by coupling the four constituent particles; electron, proton, neutron, and neutrino, into a consistent model [4].

Whilst Pauli was not convinced of the ability to detect neutrinos, **the first observations of the particle were made in the mid-1950s when neutrinos from a reactor were observed via the inverse  $\beta$ -decay (IBD) process,  $\bar{\nu}_e + p \rightarrow n + e^+$  [5, 6]. The detector consisted of two parts: a neutrino interaction medium and a liquid scintillator.** The interaction medium was built from two water tanks. These were loaded with cadmium chloride to allow increased efficiency of neutron capture. The positron emitted from IBD annihilates,  $e^+ + e^- \rightarrow 2\gamma$ , generating a prompt signal and the neutron is captured on the cadmium via  $n + ^{108}Cd \rightarrow ^{109^*}Cd \rightarrow ^{109}Cd + \gamma$ , producing a delayed signal. **The experiment observed an increase in the neutrino event rate when the reactor was operating compared to when it was switched off, in much the same way as modern reactor neutrino experiments operate. An increase in the coincidence rate was observed when the reactor was operating which was interpreted as interactions from neutrinos generated in the reactor.**

After the discovery of the  $\nu_e$ , the natural question of how many flavours of neutrino exist was asked. In 1962, a measurement of the  $\nu_\mu$  was conducted at the Brookhaven National Laboratory [7]. A proton beam was directed at a beryllium target, generating a  $\pi$ -dominated beam which then decayed via  $\pi^\pm \rightarrow \mu^\pm + (\nu_\mu, \bar{\nu}_\mu)$ , and the subsequent interactions of the  $\nu_\mu$  were observed. **As the subsequent interaction of the neutrino generates muons rather than electrons, it was determined the**

<sup>179</sup>  **$\nu_\mu$  was fundamentally different from  $\nu_e$ .** The final observation to be made was  
<sup>180</sup> that of the  $\nu_\tau$  from the DONUT experiment [8]. Three neutrinos seem the obvi-  
<sup>181</sup> ous solution as it mirrors the known number of charged lepton (as they form weak  
<sup>182</sup> isospin doublets) but there could be evidence of more. Several neutrino experi-  
<sup>183</sup> ments have found anomalous results [9, 10] which could be attributed to sterile  
<sup>184</sup> neutrinos . **However, however** cosmological observations indicate the number of  
<sup>185</sup> neutrino species  $N_{eff} = 2.99 \pm 0.17$  [11], as measured from the cosmic microwave  
<sup>186</sup> background power spectrum, and Stanford Linear Accelerator found the number  
<sup>187</sup> of active neutrino flavours to be  $N_\nu 2.9840 \pm 0.0082$  [12] from measurements of the  
<sup>188</sup> Z-decay width.

## <sup>189</sup> 1.2 Theory of Neutrino Oscillation

<sup>190</sup> As direct evidence of beyond Standard Model physics, a neutrino generated with  
<sup>191</sup> lepton flavour  $\alpha$  can change into a different lepton flavour  $\beta$  after propagating some  
<sup>192</sup> distance. This phenomenon is called neutrino oscillation and requires that neutrinos  
<sup>193</sup> must have a non-zero mass (as seen in subsection 1.2.1). This **observation** is direct  
<sup>194</sup> evidence of beyond standard model physics. This behaviour has been characterised  
<sup>195</sup> by the Pontecorvo-Maki-Nakagawa-Sakata (PMNS) [13–15] mixing matrix which  
<sup>196</sup> describes how the flavour and mass of neutrinos are associated. This is analogous to  
<sup>197</sup> the Cabibbo-Kobayashi-Maskawa (CKM) [16] matrix measured in quark physics.

### <sup>198</sup> 1.2.1 Three Flavour Oscillations

<sup>199</sup> The PMNS parameterisation defines three flavour eigenstates,  $\nu_e$ ,  $\nu_\mu$  and  $\nu_\tau$  (indexed  
<sup>200</sup>  $\nu_\alpha$ ), which are **assigned based upon** eigenstates of the weak interaction **flavour states**

201 and three mass eigenstates,  $\nu_1$ ,  $\nu_2$  and  $\nu_3$  (indexed  $\nu_i$ ). Each mass eigenstate is the  
202 superposition of all three flavour states,

$$|\nu_i\rangle = \sum_{\alpha} U_{\alpha i} |\nu_{\alpha}\rangle. \quad (1.1)$$

203 Where  $U$  is the PMNS matrix which **is unitary and connects correlates** the mass  
204 and flavour eigenstates.

205 ~~Neutrinos interact with leptons of the same weak flavour eigenstate rather than~~  
206 ~~mass eigenstate. The weak interaction couples to flavour eigenstates so neutrinos~~  
207 ~~interact with leptons of the same flavour.~~ The propagation of a neutrino flavour  
208 eigenstate, in a vacuum, can be re-written as a plane-wave solution to the time-  
209 dependent Schrödinger equation,

$$|\nu_{\alpha}(t)\rangle = \sum_i U_{\alpha i}^{*} |\nu_i\rangle e^{-i\phi_i}. \quad (1.2)$$

210 The probability of observing a neutrino of flavour eigenstate  $\beta$  from one which  
211 originated as flavour  $\alpha$  can be calculated as,

$$P(\nu_{\alpha} \rightarrow \nu_{\beta}) = |\langle \nu_{\beta} | \nu_{\alpha}(t) \rangle|^2 = \sum_{i,j} U_{\alpha i}^{*} U_{\beta i} U_{\alpha j} U_{\beta j}^{*} e^{-i(\phi_j - \phi_i)} \quad (1.3)$$

212 The  $\phi_i$  term can be expressed in terms of the energy,  $E_i$ , and magnitude of the  
213 three momenta,  $p_i$ , of the neutrino,  $\phi_i = E_i t - p_i x$  ( $t$  and  $x$  being time and position  
214 coordinates). Therefore,

$$\phi_j - \phi_i = E_j t - E_i t - p_j x + p_i x. \quad (1.4)$$

<sup>215</sup> For a relativistic particle,  $E_i \gg m_i$ ,

$$p_i = \sqrt{E_i^2 - m_i^2} \approx E_i - \frac{m_i^2}{2E_i}. \quad (1.5)$$

<sup>216</sup> Making the approximations that neutrinos are relativistic, the mass eigenstates  
<sup>217</sup> were created with the same energy and that  $x = L$ , where  $L$  is the distance traveled by  
<sup>218</sup> the neutrino, Equation 1.4 then becomes

$$\phi_j - \phi_i = \frac{\Delta m_{ij}^2 L}{2E}, \quad (1.6)$$

<sup>219</sup> where  $\Delta m_{ij}^2 = m_i^2 - m_j^2$ . This, **teamed combined** with further use of unitarity  
<sup>220</sup> relations results in Equation 1.3 becoming

$$\begin{aligned} P(\nu_\alpha \rightarrow \nu_\beta) &= \delta_{\alpha\beta} - 4 \sum_{i>j} \Re \left( U_{\alpha i}^* U_{\beta i} U_{\alpha j} U_{\beta j}^* \right) \sin^2 \left( \frac{\Delta m_{ij}^2 L}{4E} \right) \\ &\quad + (-) 2 \sum_{i>j} \Im \left( U_{\alpha i}^* U_{\beta i} U_{\alpha j} U_{\beta j}^* \right) \sin \left( \frac{\Delta m_{ij}^2 L}{2E} \right). \end{aligned} \quad (1.7)$$

<sup>221</sup> Where  $\delta_{\alpha\beta}$  is the Kronecker delta function and the negative sign **on the last term** is  
<sup>222</sup> included for the oscillation probability of antineutrinos.

<sup>223</sup> Typically, the PMNS matrix is parameterised into three mixing angles, a charge  
<sup>224</sup> parity (CP) violating phase  $\delta_{CP}$ , and two Majorana phases  $\alpha_{1,2}$ ,

$$U = \underbrace{\begin{pmatrix} 1 & 0 & 0 \\ 0 & c_{23} & s_{23} \\ 0 & -s_{23} & c_{23} \end{pmatrix}}_{\text{Atmospheric, Accelerator}} \underbrace{\begin{pmatrix} c_{13} & 0 & s_{13}e^{-i\delta_{CP}} \\ 0 & 1 & 0 \\ -s_{13}e^{-i\delta_{CP}} & 0 & c_{13} \end{pmatrix}}_{\text{Reactor, Accelerator}} \underbrace{\begin{pmatrix} c_{12} & s_{12} & 0 \\ -s_{12} & c_{12} & 0 \\ 0 & 0 & 1 \end{pmatrix}}_{\text{Reactor, Solar}} \underbrace{\begin{pmatrix} e^{i\alpha_1/2} & 0 & 0 \\ 0 & e^{i\alpha_2/2} & 0 \\ 0 & 0 & 1 \end{pmatrix}}_{\text{Majorana}}. \quad (1.8)$$

<sup>225</sup> Where  $s_{ij} = \sin(\theta_{ij})$  and  $c_{ij} = \cos(\theta_{ij})$ . The oscillation parameters are often  
<sup>226</sup> grouped; (1,2) as “solar”, (2,3) as “atmospheric” and (1,3) as “reactor”. Many  
<sup>227</sup> neutrino experiments aim to measure the PMNS parameters from a wide array of  
<sup>228</sup> origins, as is the purpose of this thesis.

<sup>229</sup> The Majorana phase,  $\alpha_{1,2}$ , **containing matrix** included within **the fourth matrix**  
<sup>230</sup> **in** Equation 1.8 is only included for completeness. For an oscillation analysis ex-  
<sup>231</sup> periment, **any term in this oscillation probability calculation containing this phase**  
<sup>232</sup> **disappears any terms containing thtis phase disappear** due to taking the expectation  
<sup>233</sup> value of the PMNS matrix. **Measurements of these phases are typically performed**  
<sup>234</sup> **by experiments searching for neutrino-less double  $\beta$ -decay [17].**

<sup>235</sup> A two flavour approximation can be **attained obtained** when one assumes the third  
<sup>236</sup> mass eigenstate is degenerate with another. As discussed in section 1.3, it is found  
<sup>237</sup> that  $\Delta m_{21}^2 \ll |\Delta m_{31}^2|$ . This results in the two flavour approximation being reasonable  
<sup>238</sup> for understanding the features of the oscillation. In this two flavour case, the mixing  
<sup>239</sup> matrix becomes,

$$U_{2 \text{ Flav.}} = \begin{pmatrix} \cos(\theta) & \sin(\theta) \\ -\sin(\theta) & \cos(\theta) \end{pmatrix}. \quad (1.9)$$

<sup>240</sup> This culminates in the oscillation probability,

$$\begin{aligned} P(\nu_\alpha \rightarrow \nu_\alpha) &= 1 - \sin^2(2\theta) \sin^2\left(\frac{\Delta m^2 L}{4E}\right), \\ P(\nu_\alpha \rightarrow \nu_\beta) &= \sin^2(2\theta) \sin^2\left(\frac{\Delta m^2 L}{4E}\right). \end{aligned} \quad (1.10)$$

<sup>241</sup> **For Where**  $\alpha \neq \beta$ . For a fixed neutrino energy, the oscillation probability is a sinu-  
<sup>242</sup> soidal function depending upon the distance over which the neutrino propagates. The  
<sup>243</sup> frequency and amplitude of oscillation are dependent upon **the ratio of the**  $\Delta m^2 / 4E$   
<sup>244</sup> and  $\sin^2 2\theta$ , respectively. **The oscillation probabilities presented thus far assume**  
<sup>245</sup> **c = 1, where c is the speed of light in vacuum. In more familiar units**, the maxi-  
<sup>246</sup> mum oscillation probability for a fixed value of  $\theta$  is given at  $L[\text{km}] / E[\text{GeV}] \sim 1.27 / \Delta m^2$ .  
<sup>247</sup> It is this calculation that determines the best  $L/E$  value for a given experiment to be  
<sup>248</sup> designed around for measurements of a specific value of  $\Delta m^2$ .

### <sup>249</sup> 1.2.2 The MSW Effect

<sup>250</sup> The theory of neutrino oscillation in a vacuum **is has been** described in subsection 1.2.1.  
<sup>251</sup> However, the beam neutrinos and atmospheric neutrinos originating from below the  
<sup>252</sup> horizon propagate through matter in the Earth. The coherent scattering of neutrinos  
<sup>253</sup> from a material target modifies the Hamiltonian of the system. This results in a change  
<sup>254</sup> in the oscillation probability. Notably, charged current scattering ( $\nu_e + e^- \rightarrow \nu_e + e^-$ ,

255 propagated by a  $W$  boson) only affects electron neutrinos **compared to whereas** the  
256 neutral current scattering ( $\nu_l + l^- \rightarrow \nu_l + l^-$ , propagated by a  $Z^0$  boson) interacts  
257 through all neutrino flavours equally. In the two-flavour **limit approximation**, the  
258 effective mixing parameter becomes

$$\sin^2(2\theta) \rightarrow \sin^2(2\theta_m) = \frac{\sin^2(2\theta)}{(A/\Delta m^2 - \cos(2\theta))^2 + \sin^2(2\theta)}, \quad (1.11)$$

259 where  $A = 2\sqrt{2}G_F N_e E$ , **with**  $N_e$  is the electron density of the medium and  $G_F$  is  
260 Fermi's constant. It is clear to see that there exists a value of  $A = \Delta m^2 \cos(2\theta)$  for  
261  $\Delta m^2 > 0$  which results in a divergent mixing parameter. This resonance is **due to**  
262 **termed** the Mikheyev-Smirnov-Wolfenstein (MSW) effect (or more colloquially, the  
263 matter resonance) which regenerates the electron neutrino component of the neutrino  
264 flux [18–20]. The density at which the resonance occurs is given by

$$N_e = \frac{\Delta m^2 \cos(2\theta)}{2\sqrt{2}G_F E}. \quad (1.12)$$

265 At densities lower than this critical value, the oscillation probability will be much  
266 closer to that of vacuum oscillation. **For antineutrinos,  $N_e \rightarrow -N_e$**  [21]. The reso-  
267 nance occurring from the MSW effect depends on the sign of  $\Delta m^2$ . Therefore, any  
268 neutrino oscillation experiment which observes neutrinos and antineutrinos which  
269 have propagated through matter can have some sensitivity to the ordering of the  
270 neutrino mass eigenstates.

## <sup>271</sup> 1.3 Neutrino Oscillation Measurements

<sup>272</sup> As evidence of beyond standard model physics, the 2015 Nobel Prize in Physics was  
<sup>273</sup> awarded to the Super-Kamiokande (SK) [22] and Sudbury Neutrino Observatory  
<sup>274</sup> (SNO) [23] collaborations for the first definitive observation of solar and atmospheric  
<sup>275</sup> neutrino oscillation [24]. Since then, the field has seen a wide array of oscillation  
<sup>276</sup> measurements from a variety of neutrino sources. As seen in subsection 1.2.1, the  
<sup>277</sup> neutrino oscillation probability is dependent on the ratio of the propagation baseline,  $L$ ,  
<sup>278</sup> to the neutrino energy,  $E$ . It is this ratio that determines the type of neutrino oscillation  
<sup>279</sup> a particular experiment is sensitive to.

<sup>280</sup> As illustrated in Figure 1.1, there are many neutrino sources that span a wide  
<sup>281</sup> range of energies. The least energetic neutrinos are from diffuse supernovae and  
<sup>282</sup> terrestrial neutrinos at  $O(1)$ MeV whereas the most energetic neutrinos originate from  
<sup>283</sup> atmospheric and galactic neutrinos of  $> O(1)$ TeV.

### <sup>284</sup> 1.3.1 Solar Neutrinos

<sup>285</sup> Solar neutrinos are emitted from fusion reaction chains at the center of the Sun. The  
<sup>286</sup> solar neutrino flux, given as a function of neutrino energy for different fusion and  
<sup>287</sup> decay chains, is illustrated in Figure 1.2. Whilst proton-proton fusion generates the  
<sup>288</sup> largest flux of neutrinos, the neutrinos are of low energy and are difficult to reconstruct  
<sup>289</sup> due to the IBD interaction threshold of 1.8MeV. Consequently, most experiments focus  
<sup>290</sup> on the neutrinos from the decay of  $^8B$  (via  $^8B \rightarrow ^8Be^* + e^+ + \nu_e$ ), which are higher  
<sup>291</sup> energy.

<sup>292</sup> The first measurements of solar neutrinos observed a significant reduction in the  
<sup>293</sup> event rate compared to predictions from the Standard Solar Model [27, 28]. The

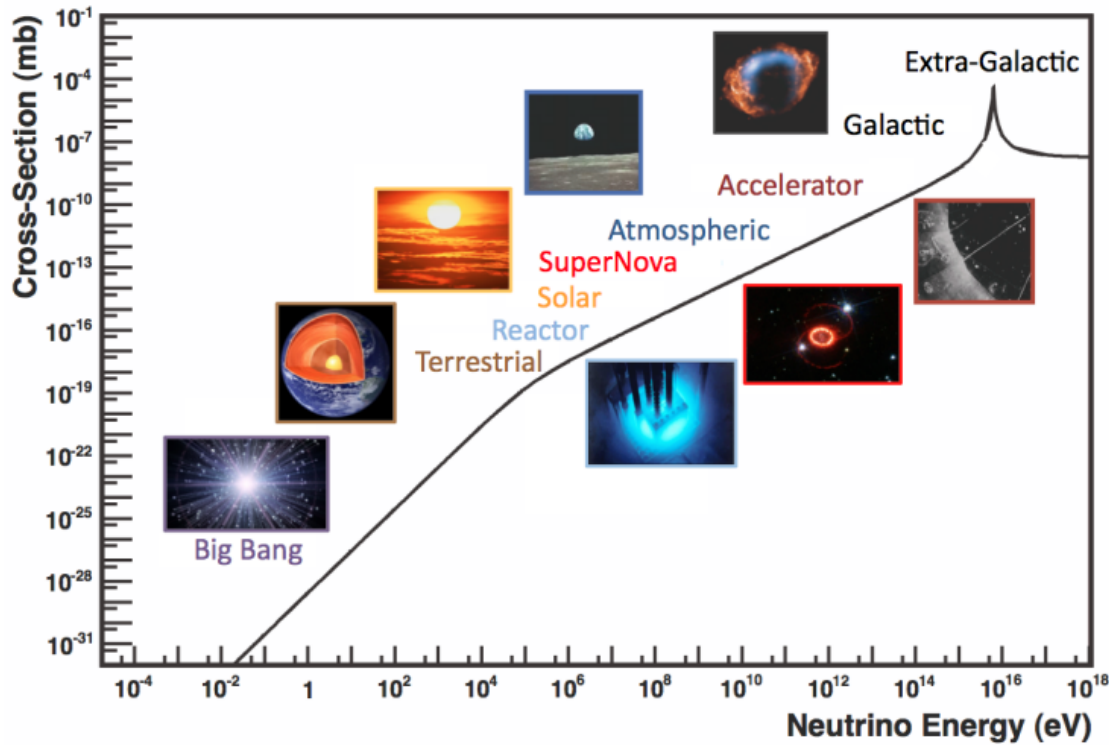


**Figure 1.1:** The cross-section of neutrinos from various natural and man-made sources as a function of neutrino energy. Taken from [25]

294 proposed solution to this “solar neutrino problem” was  $\nu_e \leftrightarrow \nu_\mu$  oscillations in a  
 295 precursory version of the PMNS model [29]. The Kamiokande [30], Gallex [31] and  
 296 Sage [32] experiments confirmed the  $\sim 0.5$  factor deficit of solar neutrinos.

297 The conclusive solution to this problem was determined by the SNO collabora-  
 298 tion [33]. Using a deuterium water target to observe  ${}^8B$  neutrinos, the event rate of  
 299 charged current (CC), neutral current (NC), and elastic scattering (ES) interactions  
 300 (Given in Equation 1.13) was simultaneously measured. CC events can only occur  
 301 for electron neutrinos, whereas the ~~other interaction NC channels are~~ is agnostic  
 302 to neutrino flavour (~~Although , and~~ the ES reaction ~~is more sensitive has a slight~~  
 303 ~~excess sensitivity~~ to electron neutrino interactions). This meant that there were direct  
 304 measurements of the  $\nu_e$  and  $\nu_x$  neutrino flux. It was concluded that the CC and ES  
 305 interaction rates were consistent with the deficit previously observed. Most impor-

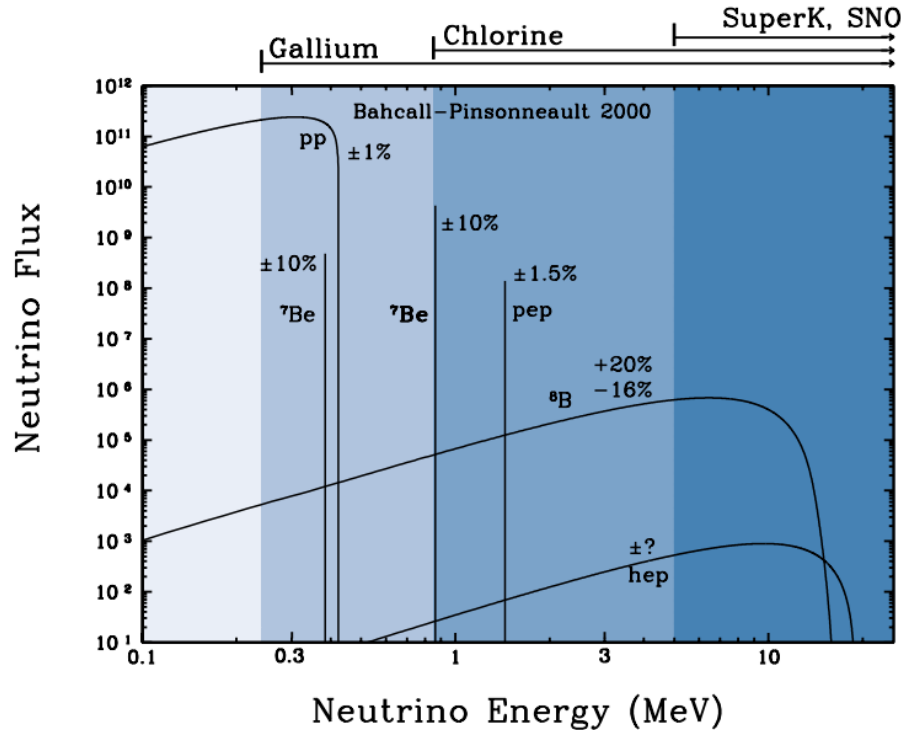
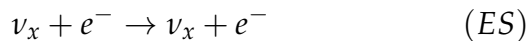
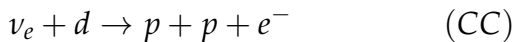


**Figure 1.2:** The solar neutrino flux as a function of neutrino energy for various fusion reactions and decay chains as predicted by the Standard Solar Model. Taken from [26].

tantly, the NC reaction rate was only consistent with the others under the hypothesis of flavour transformation.



Many experiments have since measured the neutrino flux of different interaction chains within the sun [34–36]. The most recent measurement was that of CNO neutrinos which were recently observed with  $5\sigma$  significance by the Borexino collaboration. Future neutrino experiments aim to further these spectroscopic measurements of different fusion chains within the Sun [37–39]. Solar neutrinos act as an irreducible

<sup>313</sup> background for dark matter experiments like DARWIN but oscillation parameter  
<sup>314</sup> measurements can be made [40].

### <sup>315</sup> 1.3.2 Atmospheric Neutrinos

<sup>316</sup> The interactions of primary cosmic ray protons in Earth's upper atmosphere generate  
<sup>317</sup> showers of energetic hadrons. These are mostly pions and kaons which when they  
<sup>318</sup> decay produce a natural source of neutrinos spanning energies of MeV to TeV [41].

<sup>319</sup> **This** The main decay is via

$$\begin{aligned} \pi^\pm &\rightarrow \mu^\pm + (\nu_\mu, \bar{\nu}_\mu) \\ \mu^\pm &\rightarrow e^\pm + (\nu_\mu, \bar{\nu}_\mu) + (\nu_e, \bar{\nu}_e) \end{aligned} \tag{1.14}$$

<sup>320</sup> such that for a single pion decay, three neutrinos are typically produced. The  
<sup>321</sup> atmospheric neutrino flux energy spectra as predicted by the Bartol [42], Honda  
<sup>322</sup> [43–45], and FLUKA [46] models are illustrated in Figure 1.3. The flux distribution  
<sup>323</sup> peaks at an energy of  $O(10)\text{GeV}$ . The uncertainties associated with these models  
<sup>324</sup> are dominated by the hadronic production of kaon and pions as well as the primary  
<sup>325</sup> cosmic flux.

<sup>326</sup> Unlike long-baseline experiments which have a fixed baseline, the distance at-  
<sup>327</sup> mospheric neutrinos propagate is dependent upon the zenith angle at which they  
<sup>328</sup> interact. This is illustrated in Figure 1.4. Neutrinos that are generated directly above  
<sup>329</sup> the detector ( $\cos(\theta) = 1.0$ ) have a baseline equivalent to the height of the atmosphere  
<sup>330</sup> whereas neutrinos that interact directly below the detector ( $\cos(\theta) = -1.0$ ) have to  
<sup>331</sup> travel a length equal to the diameter of the Earth. This means atmospheric neutrinos  
<sup>332</sup> have a baseline that varies from  $O(20)\text{km}$  to  $O(6 \times 10^3)\text{km}$ . Any neutrino generated

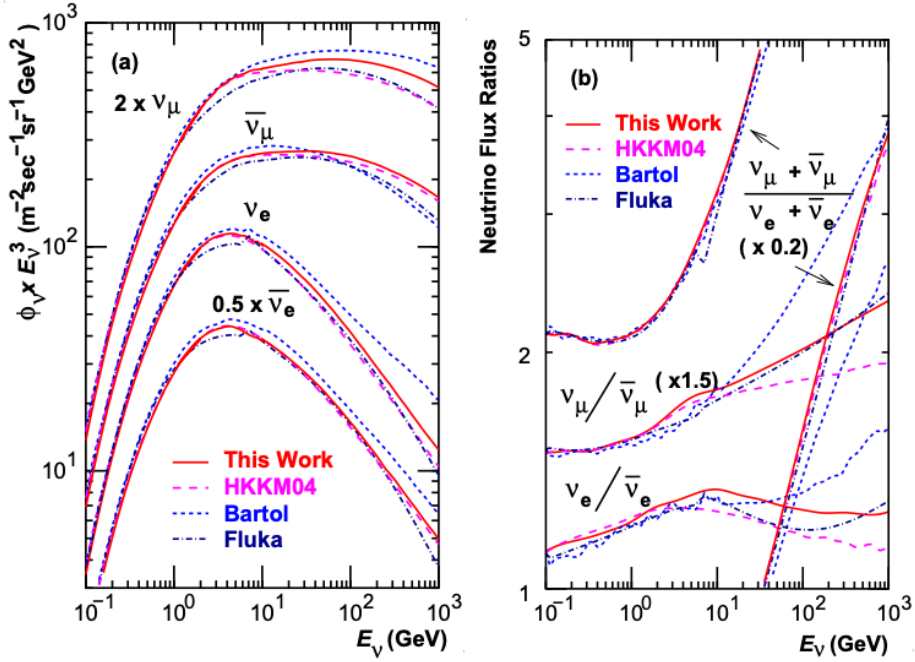


**Figure 1.3:** Left panel: The atmospheric neutrino flux for different neutrino flavours as a function of neutrino energy as predicted by the 2007 Honda model (“This work”) [43], the 2004 Honda model (“HKKM04”) [44], the Bartol model [42] and the FLUKA model [46]. Right panel: The ratio of the muon to electron neutrino flux as predicted by all the quoted models. Both figures taken from [43].

333 at or below the horizon will be subject to matter effects as they propagate through the

334 Earth.

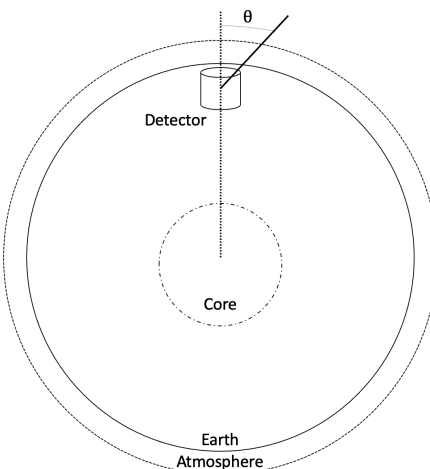


**Figure 1.4:** A diagram illustrating the definition of zenith angle as used in the Super Kamiokande experiment [47].

Figure 1.5 highlights the neutrino flux as a function of the zenith angle for different slices of neutrino energy. For medium to high-energy neutrinos (and to a lesser degree for low-energy neutrinos), the flux is approximately symmetric around  $\cos(\theta) = 0$ . To the accuracy of this approximation, the systematic uncertainties associated with atmospheric flux for comparing upward-going and down-going neutrino cancels. This allows the down-going events, which are mostly insensitive to oscillation probabilities, to act as an unoscillated prediction (similar to a near detector in an accelerator neutrino experiment).

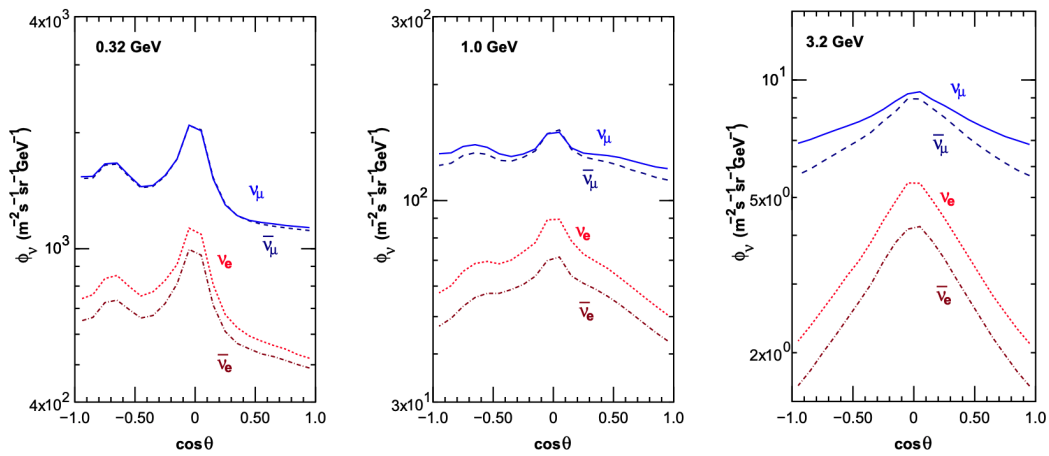


**Figure 1.5:** Prediction of  $\nu_e, \bar{\nu}_e, \nu_\mu, \bar{\nu}_\mu$  fluxes as a function of zenith angle as calculated by the HKKM model [45]. The left, middle and right panels represent three values of neutrino energy, 0.32GeV, 1.0GeV and 3.2GeV respectively. Predictions for other models including Bartol [42], Honda [43] and FLUKA [46] are given in [47].

Precursory hints of atmospheric neutrinos were observed in the mid-1960s searching for  $(\bar{\nu}_\mu + X \rightarrow X^* + \mu^\pm)$  [48], although it was called an anomaly at the time of measurement. This was succeeded with the IMB-3 [49] and Kamiokande [50] experiments which measured the ratio of muon neutrinos compared to electron neutrinos  $R(\nu_\mu/\nu_e)$ . Both experiments were found to have a consistent deficit of muon neutrinos, with  $R(\nu_\mu/\nu_e) = 0.67 \pm 0.17$  and  $R(\nu_\mu/\nu_e) = 0.60^{+0.07}_{-0.06} \pm 0.05$ . Super-Kamiokande (SK) [47] extended this analysis by fitting oscillation parameters in  $P(\nu_\mu \rightarrow \nu_\tau)$  which found best fit parameters  $\sin^2(2\theta) > 0.92$  and  $1.5 \times 10^{-3} < \Delta m^2 < 3.4 \times 10^{-3}$  eV<sup>2</sup>.

Since then, atmospheric neutrino experiments have been making precision measurements of the  $\sin^2(\theta_{23})$  and  $\Delta m_{32}^2$  oscillation parameters. Atmospheric neutrino oscillation is dominated by  $P(\nu_\mu \rightarrow \nu_\tau)$ , where SK observed a  $4.6\sigma$  discovery of  $\nu_\tau$  appearance [51]. Figure 1.6 illustrates the current estimates on the atmospheric mixing parameters from a wide range of atmospheric and accelerator neutrino observatories.

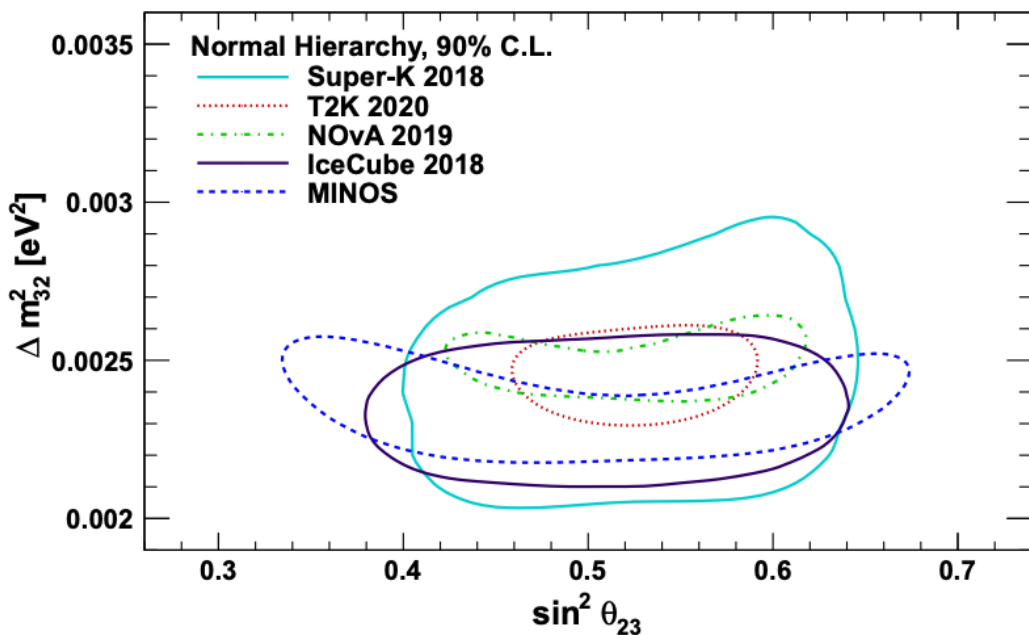


**Figure 1.6:** Constraints on the atmospheric oscillation parameters,  $\sin^2(\theta_{23})$  and  $\Delta m_{32}^2$ , from atmospheric and long baseline experiments: SK [52], T2K [53], NOvA [54], IceCube [55] and MINOS [56]. Figure taken from [57].

### 1.3.3 Accelerator Neutrinos

The concept of using a man-made “neutrino beam” was first realised in 1962 [58]. Since then, many experiments have followed which all use the same fundamental concepts. Typically, a proton beam is aimed at a target producing charged mesons that decay to neutrinos. The mesons can be sign-selected by the use of magnetic focusing horns to generate a neutrino or antineutrino beam. Pions are the primary meson that decay and depending on the orientation of the magnetic field, a muon

363 (anti-)neutrino beam is generated via  $\pi^+ \rightarrow \mu^+ + \nu_\mu$  or  $\pi^- \rightarrow \mu^- + \bar{\nu}_\mu$ . The decay of  
364 muons and kaons does result in an irreducible intrinsic electron neutrino background.  
365 In T2K, this background contamination is  $O(< 1\%)$  [59]. There is also an approxi-  
366 mately  $\sim 5\%$  “wrong-sign” neutrino background of  $\bar{\nu}_\mu$  generated via the same decays.  
367 **As the beam is generated by proton interactions (rather than anti-proton interac-**  
368 **tions), the wrong-sign component of the neutrino beam is larger when operating**  
369 **in antineutrino mode.**

370 ~~The energy of each neutrino in the beam is dependent on the energy of the~~  
371 ~~initial proton beam. Therefore, tuning the proton energy allows Tuning the proton~~  
372 ~~energy in the beam and using beam focusing techniques allows~~ the neutrino energy  
373 to be set to a value that maximises the disappearance oscillation probability in the  $L/E$   
374 term in Equation 1.10. This means that accelerator experiments are typically more  
375 sensitive to the mixing parameters as compared to a natural neutrino source. However,  
376 the disadvantage compared to atmospheric neutrino experiments is that the baseline  
377 has to be shorter due to the lower flux. Consequently, there is typically less sensitivity  
378 to matter effects and the ordering of the neutrino mass eigenstates.

379 A neutrino experiment measures

$$R(\vec{x}) = \Phi(E_\nu) \times \sigma(E_\nu) \times \epsilon(\vec{x}) \times P(\nu_\alpha \rightarrow \nu_\beta), \quad (1.15)$$

380 where  $R(\vec{x})$  is the event rate of neutrinos at position  $\vec{x}$ ,  $\Phi(E_\nu)$  is the flux of neutrinos  
381 with energy  $E_\nu$ ,  $\sigma(E_\nu)$  is the cross-section of the neutrino interaction and  $\epsilon(\vec{x})$  is the  
382 efficiency **and resolution** of the detector. In order to leverage the most out of an  
383 accelerator neutrino experiment, the flux and cross-section systematics need to be  
384 constrained. This is typically done via the use of a “near detector”, situated at a baseline

385 of  $O(1)$ km. This detector observes the unoscillated neutrino flux and constrains the  
386 parameters used within the flux and cross-section model.

387 The first accelerator experiments to precisely measure oscillation parameters were  
388 MINOS [60] and K2K [61]. These experiments confirmed the  $\nu_\mu \rightarrow \nu_\mu$  **oscillations**  
389  $\nu_\mu$  **disappearance** seen in atmospheric neutrino experiments by finding consistent  
390 **mixing** parameter values for  $\sin^2(\theta_{23})$  and  $\Delta m_{23}^2$ . The current generation of accelera-  
391 tor neutrino experiments, T2K and NO $\nu$ A extended this field by observing  $\bar{\nu}_\mu \rightarrow \bar{\nu}_e$   
392 and lead the sensitivity to atmospheric mixing parameters as seen in Figure 1.6 [62].  
393 The two experiments differ in their peak neutrino energy, baseline, and detection  
394 technique. The NO $\nu$ A experiment is situated at a baseline of 810km from the NuMI  
395 beamline which delivers 2GeV neutrinos. The T2K neutrino beam is peaked around  
396 0.6GeV and propagates 295km. The NO $\nu$ A experiment also uses functionally iden-  
397 tical detectors (near and far) which allow the approximate cancellation of detector  
398 systematics whereas T2K uses a plastic scintillator technique at the near detector and  
399 a water Cherenkov far detector. The future generation experiments DUNE [63] and  
400 Hyper-Kamiokande [64] will succeed these experiments as the high-precision era of  
401 neutrino oscillation parameter measurements develops.

402 Several anomalous results have been observed in the LSND [9] and MiniBooNE [10]  
403 detectors which were designed with purposefully short baselines. Parts of the neu-  
404 trino community attributed these results to oscillations induced by a fourth “sterile”  
405 neutrino [65] but several searches in other experiments, MicroBooNE [66] and KAR-  
406 MEN [67], found no hints of additional neutrino species. The solution to the anomalous  
407 results **are is** still being determined.

### <sup>408</sup> 1.3.4 Reactor Neutrinos

<sup>409</sup> As illustrated in the first discovery of neutrinos (section 1.1), nuclear reactors are a very  
<sup>410</sup> useful man-made source of electron antineutrinos. For reactors that use low-enriched  
<sup>411</sup> uranium  $^{235}\text{U}$  as fuel, the antineutrino flux is dominated by the  $\beta$ -decay fission of  $^{235}\text{U}$ ,  
<sup>412</sup>  $^{238}\text{U}$ ,  $^{239}\text{Pu}$  and  $^{241}\text{Pu}$  [68] as illustrated in Figure 1.7.

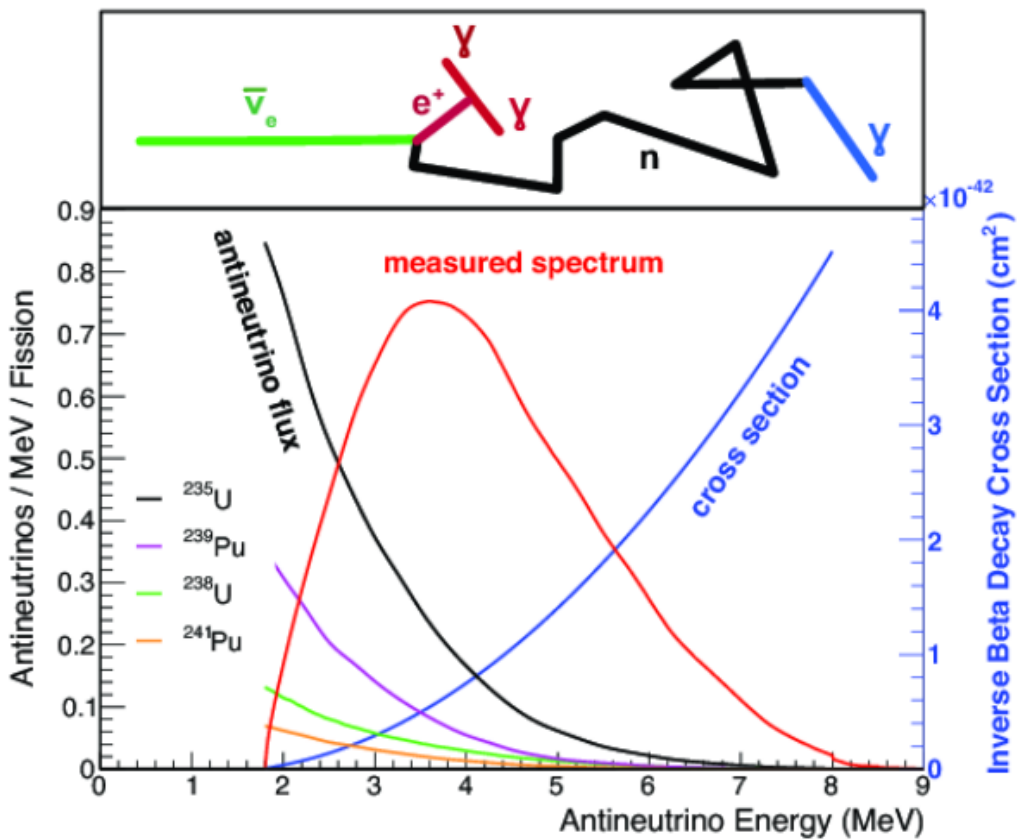


**Figure 1.7:** Reactor electron antineutrino fluxes for  $^{235}\text{U}$  (Black),  $^{238}\text{U}$  (Green),  $^{239}\text{Pu}$  (Purple), and  $^{241}\text{Pu}$  (Orange) isotopes. The inverse  $\beta$ -decay cross-section (Blue) and corresponding measurable neutrino spectrum (Red) are also given. Top panel: Schematic of Inverse  $\beta$ -decay interaction including the eventual capture of the emitted neutron. This capture emits a  $\gamma$ -ray which provides a second signal of the event. Taken from [69].

<sup>413</sup> Due to their low energy, reactor electron antineutrinos predominantly interact  
<sup>414</sup> via the inverse  $\beta$ -decay (IBD) interaction. The typical signature contains two signals  
<sup>415</sup> delayed by  $O(200)\mu\text{s}$ ; firstly the prompt photons from positron annihilation, and

<sup>416</sup> secondly the photons emitted ( $E_{tot}^\gamma = 2.2\text{MeV}$ ) from de-excitation after neutron capture  
<sup>417</sup> on hydrogen. Searching for both signals improves the detector's ability to distinguish  
<sup>418</sup> between background and signal events [70]. Recently, SK included gadolinium dopants  
<sup>419</sup> into the ultra-pure water to increase the energy released from the photon cascade to  
<sup>420</sup>  $\sim 8\text{MeV}$  and reduce the time of the delayed signal to  $\sim 28\mu\text{s}$ .

<sup>421</sup> There are many short baseline experiments ( $L \sim O(1)\text{km}$ ) that have measured the  
<sup>422</sup>  $\sin^2(\theta_{13})$  and  $\Delta m_{23}^2$  oscillation parameters. Daya Bay [71], RENO [72] and Double  
<sup>423</sup> Chooz [73] have all provided precise measurements, with the first discovery of a  
<sup>424</sup> non-zero  $\theta_{13}$  made by Daya Bay and RENO (and ~~complimented complemented~~ by  
<sup>425</sup> T2K [73]). The constraints on  $\sin^2(\theta_{13})$  by the reactor experiments lead the field and  
<sup>426</sup> are often used as external inputs to accelerator neutrino experiments to improve their  
<sup>427</sup> sensitivity to  $\delta_{CP}$  and mass hierarchy determination. JUNO-TAO [74], a small collabora-  
<sup>428</sup> ration within the larger JUNO experiment, is a next-generation reactor experiment that  
<sup>429</sup> aims to precisely measure the isotopic antineutrino yields from the different fission  
<sup>430</sup> chains. Alongside this, it aims to explain the '5MeV excess' [75–77] by conducting a  
<sup>431</sup> search for sterile neutrinos with a mass scale of around 1eV.

<sup>432</sup> Kamland [78] is the only experiment to have observed reactor neutrinos using a  
<sup>433</sup> long baseline (flux weighted averaged baseline of  $L \sim 180\text{km}$ ) which allows it to have  
<sup>434</sup> sensitivity to  $\Delta m_{12}^2$ . Combined with the SK solar neutrino experiment, the combined  
<sup>435</sup> analysis puts the most stringent constraint on  $\Delta m_{12}^2$  [79] ~~which is used as a prior~~  
<sup>436</sup> ~~uncertainty within accelerator neutrino experiments.~~

## <sup>437</sup> 1.4 Summary

<sup>438</sup> Since observing the first evidence of neutrino oscillations in the late 1990's, numerous  
<sup>439</sup> measurements of the mixing parameters have been made. Many experiments use

<sup>440</sup> neutrinos as a tool for discovery of new physics (diffuse supernova background,  
<sup>441</sup> neutrinoless double beta decay and others) so the PMNS parameters are summarised  
<sup>442</sup> in the Particle Data Group (PDG) review tables. The analysis presented in this thesis  
<sup>443</sup> focuses on the 2020 T2K oscillation analysis presented in [80] where the 2018 PDG  
<sup>444</sup> constraints [81] were used. These constraints are outlined in Table 1.1.

Parameter	2018 Constraint
$\sin^2(\theta_{12})$	$0.307 \pm 0.013$
$\Delta m_{21}^2$	$(7.53 \pm 0.18) \times 10^{-5} \text{ eV}^2$
$\sin^2(\theta_{13})$	$(2.12 \pm 0.08) \times 10^{-2}$
$\sin^2(\theta_{23})$ (I.H., Q1)	$0.421^{+0.033}_{-0.025}$
$\sin^2(\theta_{23})$ (I.H., Q2)	$0.592^{+0.023}_{-0.030}$
$\sin^2(\theta_{23})$ (N.H., Q1)	$0.417^{+0.025}_{-0.028}$
$\sin^2(\theta_{23})$ (N.H., Q2)	$0.597^{+0.024}_{-0.030}$
$\Delta m_{32}^2$ (I.H.)	$(-2.56 \pm 0.04) \times 10^{-3} \text{ eV}^2$
$\Delta m_{32}^2$ (N.H.)	$(2.51 \pm 0.05) \times 10^{-3} \text{ eV}^2$

**Table 1.1:** The 2018 Particle Data Group constraints of the oscillation parameters taken from [81]. The value of  $\Delta m_{23}^2$  is given for both normal hierarchy (N.H.) and inverted hierarchy (I.H.) and  $\sin^2(\theta_{23})$  is broken down by whether its value is below (Q1) or above (Q2) 0.5.

<sup>445</sup> The  $\sin^2(\theta_{13})$  measurement stems from the electron antineutrino disappearance,  
<sup>446</sup>  $P(\bar{\nu}_e \rightarrow \bar{\nu}_e)$ , and is take as the average best-fit from the combination of Daya Bay,  
<sup>447</sup> Reno and Double Chooz. It is often used as a prior uncertainty within other neu-  
<sup>448</sup> trino oscillation experiments, typically termed the reactor constraint. The  $\sin^2(\theta_{12})$   
<sup>449</sup> parameter is predominantly measured through electron neutrino disappearance,  
<sup>450</sup>  $P(\nu_e \rightarrow \nu_{\mu,\tau})$ , in solar neutrino experiments. The long-baseline reactor neutrino ex-  
<sup>451</sup> periment Kamland also has sensitivity to this parameter and is used in a joint fit to  
<sup>452</sup> solar data from SNO and SK, using the reactor constraint. Measurements of  $\sin^2(\theta_{23})$   
<sup>453</sup> are made by long-baseline and atmospheric neutrino experiments. The PDG value  
<sup>454</sup> is a joint fit of T2K, NO $\nu$ A, MINOS and IceCube DeepCore experiments. The latest  
<sup>455</sup> T2K-only measurement, provided at Neutrino2020 and is the basis of this thesis, is

given as  $\sin^2(\theta_{23}) = 0.546^{+0.024}_{-0.046}$  [80]. The PDG constraint on  $\Delta m_{12}^2$  is provided by the KamLAND experiment using solar and geoneutrino data. This measurement utilised a  $\sin^2(\theta_{13})$  constraint from accelerator (T2K, MINOS) and reactor neutrino (Daya Bay, RENO, Double Chooz) experiments. Accelerator measurements make some of the most stringent constraints on  $\Delta m_{23}^2$  although atmospheric experiments have more sensitivity to the mass hierarchy determination. The PDG performs a joint fit of accelerator and atmospheric data, in both normal and inverted hierarchy separately. The latest T2K-only result is  $\Delta m_{32}^2 = 2.49^{+0.058}_{-0.082} \times 10^{-3} \text{ eV}^2$  favouring normal hierarchy [80]. The value of  $\delta_{CP}$  is largely undetermined. CP-conserving values of 0 and  $\pi$  were rejected with  $\sim 2\sigma$  intervals, as published in Nature, although more recent analysis have reduced the rejection intervals to 90%. Since the 2018 PDG publication, there has been a new measurement of  $\sin^2(\theta_{13}) = (2.20 \pm 0.07) \times 10^{-2}$  [82], alongside updated  $\Delta m_{23}^2$  and  $\sin^2(\theta_{23})$  measurements.

469

## Chapter 2

470

### T2K and SK Experiment Overview

471 As the successor of the Kamiokande experiment, the Super-Kamiokande (SK) collaboration has been leading atmospheric neutrino oscillation analyses for over two decades.  
472 The detector has provided some of the strongest constraints on proton decay **limits** and **as well as** the first precise measurements of the  $\Delta m_{23}^2$  and  $\sin^2(\theta_{23})$  neutrino oscillation parameters. **Despite this, the The** ability of the detector to low-energy neutrino events has been significantly improved with the recent gadolinium doping of the ultra-pure water target. **section 2.1 describes the history, detection technique, and operation of the SK detector. The history, detection technique, and operation of the SK detector is described in section 2.1.**

480 The Tokai-to-Kamioka (T2K) experiment was one of the first long-baseline experiments to use both neutrino and antineutrino beams to precisely measure the charge parity violation within the neutrino sector. With the SK detector observing the oscillated neutrino flux, the T2K experiment observed the first hints of a non-zero  $\sin^2(\theta_{13})$  measurement and continues to lead the field with the constraints it provides on  $\sin^2(\theta_{13})$ ,  $\sin^2(\theta_{23})$ ,  $\Delta m_{23}^2$  and  $\delta_{CP}$ . **section 2.2 documents the The** techniques which T2K uses in generating its neutrino beam as well as the near-detector used to constrain the flux and cross-section parameters **invoked within the systematic models used in this analysis are documented in section 2.2.**

---

## <sup>489</sup> 2.1 The Super-Kamiokande Experiment

<sup>490</sup> The SK experiment began taking data in 1996 [83] and has had many modifications  
<sup>491</sup> throughout its lifespan. There have been seven defined periods of data taking as  
<sup>492</sup> noted in Table 2.1. Data taking began in SK-I which ran for five years. Between the  
<sup>493</sup> SK-I and SK-II periods, a significant proportion of the PMTs were damaged during  
<sup>494</sup> maintenance. Those that survived were equally distributed throughout the detector  
<sup>495</sup> in the SK-II era, which resulted in a reduced photo-coverage. From SK-III onwards,  
<sup>496</sup> repairs to the detector meant the full suite of PMTs was operational. Before the  
<sup>497</sup> start of SK-IV, the data acquisition and electronic systems were upgraded. Between  
<sup>498</sup> SK-IV and SK-V, a significant effort was placed into tank open maintenance and  
<sup>499</sup> repair/replacement of defective PMTs, a task for which the author of this thesis was  
<sup>500</sup> required. Consequently, the detector conditions were significantly different between  
<sup>501</sup> the two operational periods. SK-VI saw the start of the 0.01% gadolinium doped water.  
<sup>502</sup> SK-VII, which started during the writing of this thesis, has increased the gadolinium  
<sup>503</sup> concentration to 0.03% for continued operation [84].

Period	Start Date	End Date	Live-time (days)
I	April 1996	July 2001	1489.19
II	October 2002	October 2005	798.59
III	July 2006	September 2008	518.08
IV	September 2008	May 2018	3244.4
V	January 2019	July 2020	461.02
VI	July 2020	May 2022	583.3
VII	May 2022	Ongoing	N/A

**Table 2.1:** The various SK periods and respective live-time. The SK-VI live-time is calculated until 1<sup>st</sup> April 2022. SK-VII started during the writing of this thesis.

### 504 2.1.1 The SK Detector

505 The basic structure of the Super-Kamiokande (SK) detector is a cylindrical tank with a  
 506 diameter 39.3m and height 41.1m filled with ultrapure water [85]. A diagram of the  
 507 significant components of the SK detector is [illustrated given](#) in Figure 2.1. The SK  
 508 detector is situated in the Kamioka mine in Gifu, Japan. The mine is underground with  
 509 roughly 1km rock overburden (2.7km water equivalent overburden) [86]. At this depth,  
 510 the rate of cosmic ray muons is significantly decreased to a value of  $\sim 2\text{Hz}$ . The top of  
 511 the tank is covered with stainless steel which is designed as a working platform for  
 512 maintenance, calibration, and location for high voltage and data acquisition electronics.

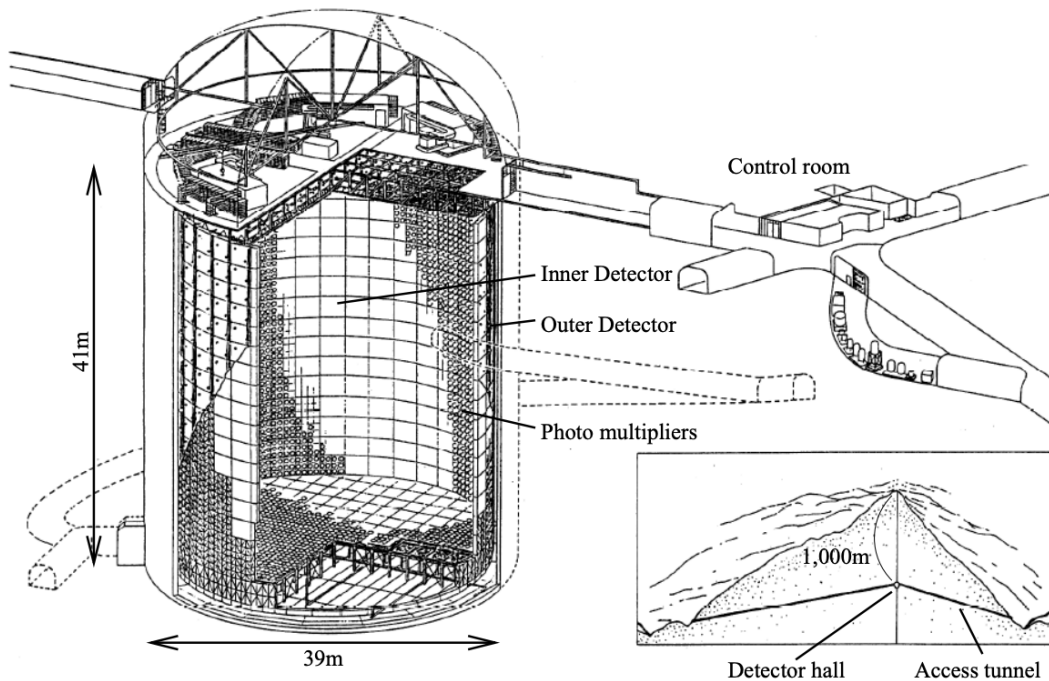


**Figure 2.1:** A schematic diagram of the Super-Kamiokande Detector. Taken from [87].

513 A smaller cylindrical structure (36.2m diameter, 33.8m height) is situated inside the  
 514 tank, with an approximate 2m gap between this structure and the outer tank wall. The  
 515 purpose of this structure is to support the photomultiplier tubes (PMTs). The volume  
 516 inside and outside the support structure is referred to as the inner detector (ID) and

517 outer detector (OD), respectively. In the SK-IV era, the ID and OD are instrumented  
518 by 11,129 50cm and 1,885 20cm PMTs respectively [85]. The ID contains a 32kton  
519 mass of water. Many analyses performed at SK use a “fiducial volume” defined by the  
520 volume of water inside the ID excluding some distance to the ID wall. This reduces the  
521 volume of the detector which is sensitive to neutrino events but reduces radioactive  
522 backgrounds and allows for better reconstruction performance. The nominal fiducial  
523 volume is defined as the area contained inside 2m from the ID wall for a total of  
524 22.5kton water [88].

525 The two regions of the detector (ID and OD) are optically separated with opaque  
526 black plastic. The purpose of this is to determine whether a track entered or exited  
527 the ID. This allows cosmic ray muons and partially contained events to be tagged and  
528 separated from neutrino events entirely contained within the ID. This black plastic is  
529 also used to cover the area between the ID PMTs to reduce photon reflection from the  
530 ID walls. Opposite to this, the OD is lined with a reflective material to allow photons to  
531 reflect around inside the OD until collected by one of the PMTs. Furthermore, each OD  
532 PMT is backed with  $50 \times 50\text{cm}$  plates of wavelength shifting acrylic which increases  
533 the efficiency of light collection [86].

534 In the SK-IV data-taking period, the photocathode coverage of the detector, or the  
535 fraction of the ID wall instrumented with PMTs, is  $\sim 40\%$  [86]. The PMTs have a  
536 quantum efficiency (the ratio of detected electrons to incident photons) of  $\sim 21\%$  for  
537 photons with wavelengths of  $360\text{nm} < \lambda < 390\text{nm}$ . The proportion of photoelectrons  
538 that produce a signal in the dynode of a PMT, termed the collection efficiency, is  
539  $> 70\%$  [86]. The PMTs used within SK are most sensitive to photons with wavelength  
540  $300\text{nm} \leq \lambda \leq 600\text{nm}$  [86]. One disadvantage of using PMTs as the detection media  
541 is that the Earth’s geomagnetic field can modify its response. Therefore, a set of

compensation coils is built around the inner surface of the detector to mitigate this effect [89].

As mentioned, the SK detector is filled with ultrapure water, which in a perfect world would contain no impurities. However, bacteria and organic compounds can significantly degrade the water quality. This decreases the attenuation length, which reduces the total number of photons that hit a PMT. To combat this, a sophisticated water treatment system has been developed [86, 90]. UV lights, mechanical filters, and membrane degasifiers are used to reduce the bacteria, suspended particulates, and radioactive materials from the water. The flow of water within the tank is also critical as it can remove stagnant bacterial growth or build-up of dust on the surfaces within the tank. Gravity drifts impurities in the water towards the bottom of the tank which, if left uncontrolled, can create asymmetric water conditions between the top and bottom of the tank. Typically, the water entering the tank is cooled below the ambient temperature of the tank to control convection and inhibit bacteria growth. Furthermore, the **rate of** dark noise hits within PMTs is sensitive to the PMT temperature [91] so controlling the temperature gradients within the tank is beneficial for stable measurements.

SK-VI is the first phase of the SK experiment to use gadolinium dopants within the ultrapure water [84]. As such, the SK water system had to be replaced to avoid removing the gadolinium concentrate from the ultrapure water [92]. For an inverse  $\beta$ -decay (IBD) interaction in a water target, the emitted neutron is thermally captured on hydrogen. This process releases 2.2MeV  $\gamma$  rays which are difficult to detect **due to as the resulting** Compton scattered electrons ~~from a  $\gamma$  ray of this energy is are~~ very close to the Cherenkov threshold, limiting the number of photons produced. Thermal capture of neutrons on gadolinium generates  $\gamma$  rays with higher energy (8MeV [70]) meaning they are more easily detected. SK-VI has 0.01% Gd loading

568 (0.02% gadolinium sulphate by mass) which causes  $\approx 50\%$  of neutrons emitted by IBD  
569 to be captured on gadolinium [93, 94]. Whilst predominantly useful for low energy  
570 analyses, Gd loading allows better  $\nu/\bar{\nu}$  separation for atmospheric neutrino event  
571 selections [95]. Efforts are currently in place to increase the gadolinium concentrate  
572 to 0.03% for  $\approx 75\%$  neutron capture efficiency on gadolinium [96]. The final stage of  
573 loading targets 0.1% concentrate.

### 574 2.1.2 Calibration

575 The calibration of the SK detector is documented in [85] and summarised below. The  
576 analysis presented within this thesis is dependent upon ‘high energy events’ (Charged  
577 particles with  $O(> 100)\text{MeV}$  momenta). These are events that are expected to generate  
578 a larger number of photons such that each PMT will be hit with multiple photons.  
579 The reconstruction of these events depends upon the charge deposited within each  
580 PMT and the timing response of each individual PMT. Therefore, the most relevant  
581 calibration techniques to this thesis are outlined.

582 Before installation, 420 PMTs were calibrated to have identical charge responses  
583 and then distributed throughout the tank in a cross-shape pattern (As illustrated by  
584 Figure 2.2). These are used as a standardised measure for the rest of the PMTs installed  
585 at similar geometric positions within SK to be calibrated against. To perform this  
586 calibration, a xenon lamp is located at the center of the SK tank which flashes uniform  
587 light at 1Hz. This allows for geometrical effects, water quality variation, and timing  
588 effects to be measured in-situ throughout normal data-taking periods.

589 When specifically performing calibration of the detector (in out-of-data taking  
590 mode), the water in the tank was circulated to avoid top/bottom asymmetric water  
591 quality. Any non-uniformity within the tank significantly affects the PMT hit proba-

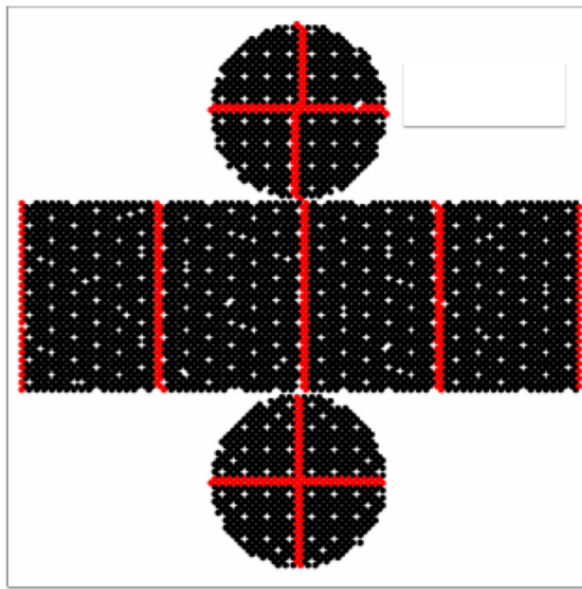


**Figure 2.2:** The location of “standard PMTs” (red) inside the SK detector. Taken from [85].

592     bility through scattering or absorption. This becomes a dominant effect for the very  
 593     low-intensity light sources discussed later which are designed such that only one  
 594     photon is incident upon a given PMT.

595       The “gain” of a PMT is defined as the ratio of the total charge of the signal produced  
 596     compared to the charge of photoelectrons emitted by the photocathodes within the  
 597     PMT. To calibrate the signal of each PMT, the “relative” and “absolute” gain values are  
 598     measured. The relative gain is the variation of gain among each of the PMTs whereas  
 599     the absolute gain is the average gain of all PMTs.

600       The relative gain is calibrated as follows. A laser is used to generate two measure-  
 601     ments: a high-intensity flash that illuminates every PMT with a sufficient number of  
 602     photons, and a low-intensity flash in which only a small number of PMTs collect light.  
 603       The first measurement creates an average charge,  $Q_{obs}(i)$  on PMT  $i$ , whereas the second  
 604     measurement ensures that each hit PMT only generates a single photoelectron. For the  
 605     low-intensity measurement, the number of times each PMT records a charge larger  
 606     than 1/4 photoelectrons,  $N_{obs}(i)$ , is counted. The values measured can be expressed as

$$\begin{aligned} Q_{obs}(i) &\propto I_H \times f(i) \times \epsilon(i) \times G(i), \\ N_{obs}(i) &\propto I_L \times f(i) \times \epsilon(i), \end{aligned} \quad (2.1)$$

607 Where  $I_H$  and  $I_L$  is the intensity of the high and low flashes,  $f(i)$  is the acceptance  
 608 efficiency of the  $i^{\text{th}}$  PMT,  $\epsilon(i)$  is the product of the quantum and collection efficiency  
 609 of the  $i^{\text{th}}$  PMT and  $G(i)$  is the gain of the  $i^{\text{th}}$  PMT. The relative gain for each PMT can  
 610 determined by taking the ratio of these quantities.

611 The absolute gain calibration is performed by observing fixed energy  $\gamma$ -rays of  
 612  $E_\gamma \sim 9\text{MeV}$  emitted isotropically from neutron capture on a NiCf source situated at  
 613 the center of the detector. This generates a photon yield of about 0.004 photoelec-  
 614 trons/PMT/event, meaning that  $> 99\%$  of PMT signals are generated from single  
 615 photoelectrons. A charge distribution is generated by performing this calibration over  
 616 all PMTs, and the average value of this distribution is taken to be the absolute gain  
 617 value.

618 As mentioned in subsection 2.1.1, the average quantum and collection efficiency  
 619 for the SK detector is  $\sim 21\%$  and  $> 70\%$  respectively. However, these values do differ  
 620 between each PMT and need to be calibrated accordingly. Consequently, the NiCf  
 621 source is also used to calibrate the “quantum  $\times$  collection” efficiency (denoted “QE”)  
 622 value of each PMT. The NiCf low-intensity source is used as the PMT hit probability  
 623 is proportional to the QE ( $N_{obs}(i) \propto \epsilon(i)$  in Equation 2.1). A Monte Carlo prediction  
 624 which includes photon absorption, scattering, and reflection is made to estimate the  
 625 number of photons incident on each PMT and the ratio of the number of predicted  
 626 to observed hits is calculated. The difference is attributed to the QE efficiency of that  
 627 PMT. This technique is extended to calculate the relative QE efficiency by normalizing  
 628 the average of all PMTs which removes the dependence on the light intensity.

629 Due to differing cable lengths and readout electronics, the timing response between  
630 a photon hitting the PMT and the signal being captured by the data acquisition can be  
631 different between each PMT. Due to threshold triggers (Described in subsection 2.1.3),  
632 the time at which a pulse reaches a threshold is dependent upon the size of the pulse.  
633 This is known as the ‘time-walk’ effect and also needs to be accounted for in each PMT.  
634 To calibrate the timing response, a pulse of light with width 0.2ns is emitted into the  
635 detector through a diffuser. Two-dimensional distributions of time and pulse height  
636 (or charge) are made for each PMT and are used to calibrate the timing response. This  
637 is performed in-situ **whilst during** data taking with the light source pulsing at 0.03Hz.

638 The top/bottom water quality asymmetry is measured using the NiCf calibration  
639 data and cross-referencing these results to the “standard PMTs”. The water attenuation  
640 length is continuously measured by the rate of vertically-downgoing cosmic-ray  
641 muons which enter via the top of the tank.

### 642 2.1.3 Data Acquisition and Triggering

643 Dark noise is the phenomenon where a PMT registers a pulse that is consistent with a  
644 single photoelectron emitted from photon detection despite the PMT being in complete  
645 darkness. This is predominately caused by two processes. Firstly there is intrinsic  
646 dark noise which is where photoelectrons gain enough thermal energy to be emitted  
647 from the photocathode, and secondly, the radioactive decay of contaminants inside the  
648 structure of the PMT. Typical dark noise rate for PMTs used within SK are  $O(3)$ kHz  
649 [86] **which equates to about 12 dark noise hits per 220ns**. This is lower than the  
650 expected number of photons generated for a ‘high energy event’ (As described in  
651 subsection 2.1.4) but instability in this value can cause biases in reconstruction.

652     The analysis presented in this thesis only uses the SK-IV period of the SK exper-  
 653     iment so this subsection focuses on the relevant points of the data acquisition and  
 654     triggering systems to that SK period. The earlier data acquisition and triggering  
 655     systems are documented in [97, 98].

656     Before the SK-IV period started, the existing front-end electronics were replaced

657     with “QTC-Based Electrons with Ethernet, QBEE” systems [99]. When the QBEE  
 658     observes a signal above a 1/4 photoelectron threshold, the charge-to-time (QTC)

659     converter generates a rectangular pulse. The start of the rectangular pulse indicates

660     the time at which the analog photoelectron signal was received and the width of the

661     pulse indicates the total charge integrated throughout the signal. This is then digitized

662     by time-to-digital converters and sent to the “front-end” PCs. The digitized signal

663     from every QBEE is then chronologically ordered and sent to the “merger” PCs. It is

664     the merger PCs that apply the software trigger. Any triggered events are passed to the

665     “organizer” PC. This sorts the data stream of multiple merger PCs into chronologically

666     ordered events which are then saved to disk. The schematic of data flow from PMTs to

667     disk is illustrated in Figure 2.3.

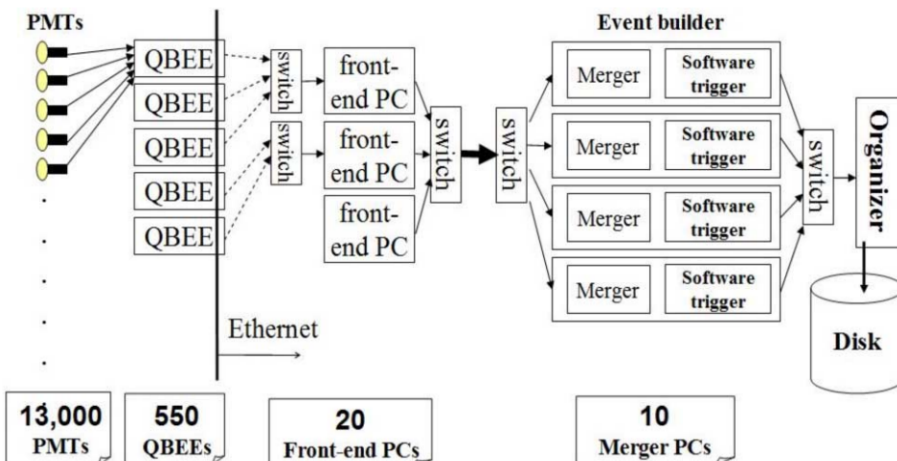


**Figure 2.3:** Schematic view of the data flow through the data acquisition and online system.  
 Taken from [100].

668 The software trigger (described in [101]) operates by determining the number of  
 669 PMT hits within a 200ns sliding window,  $N_{200\mu s}$ . **This window** coincides with the  
 670 maximum time that a Cherenkov photon would take to traverse the length of the  
 671 SK tank [98]. For lower energy events that generate fewer photons, this technique is  
 672 useful for eliminating background processes like dark noise and radioactive decay  
 673 which would be expected to separate in time. When the value of  $N_{200\mu s}$  exceeds some  
 674 threshold, a software trigger is issued. There are several trigger thresholds used within  
 675 the SK-IV period which are detailed in Table 2.2. If one of these thresholds is met, the  
 676 PMT hits within an extended time window are also read out and saved to disk. In  
 677 the special case of an event that exceeds the SHE trigger but does not exceed the OD  
 678 trigger, the AFT trigger looks for delayed coincidences of 2.2MeV gamma rays emitted  
 679 from neutron capture in a  $535\mu s$  window after the SHE trigger. A similar but more  
 680 complex “Wideband Intelligent Trigger (WIT)” has been deployed and is described  
 681 in [102].

Trigger	Acronym	Condition	Extended time window ( $\mu s$ )
Super Low Energy	SLE	>34/31 hits	1.3
Low Energy	LE	>47 hits	40
High Energy	HE	>50 hits	40
Super High Energy	SHE	>70/58 hits	40
Outer Detector	OD	>22 hits in OD	N/A

**Table 2.2:** The trigger thresholds and extended time windows saved around an event which were utilised throughout the SK-IV period. The exact thresholds can change and the values listed here represent the thresholds at the start and end of the SK-IV period.

## 682 2.1.4 Cherenkov Radiation

683 Cherenkov light is emitted from any highly energetic charged particle traveling  
 684 with relativistic velocity,  $\beta$ , greater than the local speed of light in a medium [103].  
 685 Cherenkov light is formed at the surface of a cone with characteristic pitch angle,

$$\cos(\theta) = \frac{1}{\beta n}. \quad (2.2)$$

686 where  $n$  is the refractive index of the medium. Consequently, the Cherenkov  
 687 momentum threshold,  $P_{thres}$ , is dependent upon the mass,  $m$ , of the charged particle  
 688 moving through the **media medium**,

$$P_{thres} = \frac{m}{\sqrt{n^2 - 1}} \quad (2.3)$$

689 For water, where  $n = 1.33$ , the Cherenkov threshold momentum and energy for  
 690 various particles are given in Table 2.3. In contrast,  $\gamma$ -rays are detected indirectly via  
 691 the combination of photons generated by Compton scattering and pair production.  
 692 The threshold for detection in the SK detector is typically higher than the threshold  
 693 for photon production. This is due to the fact that the attenuation of photons in the  
 694 water means that typically  $\sim 75\%$  of Cherenkov photons reach the ID PMTs. Then the  
 695 collection and quantum efficiencies described in subsection 2.1.1 result in the number  
 696 of detected photons being lower than the number of photons which reach the PMTs.

Particle	Threshold Momentum (MeV)	Threshold Energy (MeV)
Electron	0.5828	0.7751
Muon	120.5	160.3
Pion	159.2	211.7
Proton	1070.0	1423.1

**Table 2.3:** The threshold momentum and energy for a particle to generate Cherenkov light in ultrapure water, as calculated in Equation 2.2 in ultrapure water which has refractive index  $n = 1.33$ .

The Frank-Tamm equation [104] describes the relationship between the number of Cherenkov photons generated per unit length,  $dN/dx$ , the wavelength of the photons generated,  $\lambda$ , and the relativistic velocity of the charged particle,

$$\frac{d^2N}{dxd\lambda} = 2\pi\alpha \left(1 - \frac{1}{n^2\beta^2}\right) \frac{1}{\lambda^2}. \quad (2.4)$$

where  $\alpha$  is the fine structure constant. For a 100MeV momentum electron, approximately 330 photons will be produced per centimeter in the  $300\text{nm} \leq \lambda \leq 700\text{nm}$  region which the ID PMTs are most sensitive to [86].

## 2.2 The Tokai to Kamioka Experiment

The Tokai to Kamioka (T2K) experiment is a long-baseline neutrino oscillation experiment located in Japan. Proposed in the early 2000s [105, 106] to replace K2K [107], T2K was designed to observe electron neutrino appearance whilst precisely measuring the oscillation parameters associated with muon neutrino disappearance [108]. The experiment consists of a neutrino beam generated at the Japan Proton Accelerator Research Complex (J-PARC), a suite of near detectors situated 280m from the beam target, and the Super Kamiokande far detector positioned at a 295km baseline. The cross-section view of the T2K experiment is drawn in Figure 2.4.

The T2K collaboration makes world-leading measurements of the  $\sin^2(\theta_{23})$ ,  $\Delta m_{23}^2$ , and  $\delta_{CP}$  oscillation parameters. Improvements in the precision and accuracy of parameter estimates are still being made by including new data samples and developing the models which describe the neutrino interactions and detector responses [109]. Electron

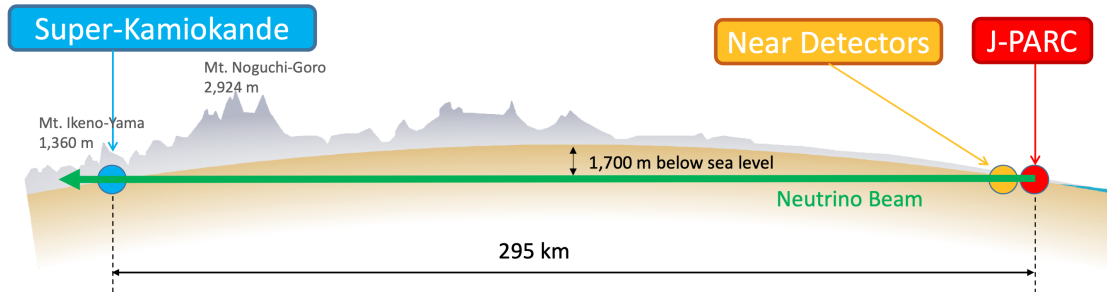


**Figure 2.4:** The cross-section view of the Tokai to Kamioka experiment illustrating the beam generation facility at J-PARC, the near detector situated at a baseline of 280m and the Super Kamiokande far detector situated 295km from the beam target.

<sup>716</sup> neutrino appearance was first observed at T2K in 2014 [110] ~~which accompanied a~~  
<sup>717</sup> ~~7.3 $\sigma$  significance of a non-zero  $\sin^2(\theta_{13})$  measurement with 7.3 $\sigma$  significance.~~

<sup>718</sup> The near detectors provide constraints on the beam flux and cross-section model  
<sup>719</sup> parameters used within the **fit oscillation analysis** by observing the unoscillated  
<sup>720</sup> neutrino beam. There are a host of detectors situated in the near detector hall (As  
<sup>721</sup> illustrated in Figure 2.5): ND280 (subsection 2.2.2), INGRID (subsection 2.2.3), NINJA  
<sup>722</sup> [111], WAGASCI [112], and Baby-MIND [113]. The latter three are not currently used  
<sup>723</sup> within the oscillation analysis presented within this thesis.

<sup>724</sup> Whilst this thesis presents the ND280 in terms of its purpose for the oscillation  
<sup>725</sup> analysis, the detector can also make many cross-section measurements at neutrino  
<sup>726</sup> energies of  $O(1)$ GeV for the different targets within the detector [114, 115]. These  
<sup>727</sup> measurements are of equal importance as they can lead the way in determining the  
<sup>728</sup> model parameters used in the interaction models for the future high-precision era of  
<sup>729</sup> neutrino physics.

### <sup>730</sup> 2.2.1 The Neutrino Beam

<sup>731</sup> The neutrino beam used within the T2K experiment is described in [59, 116] and  
<sup>732</sup> summarised below. The accelerating facility at J-PARC is composed of two sections; the

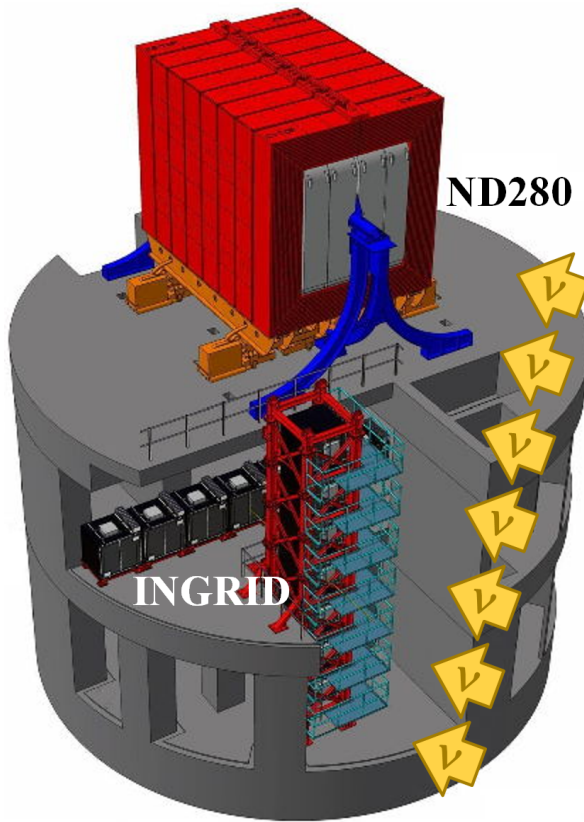
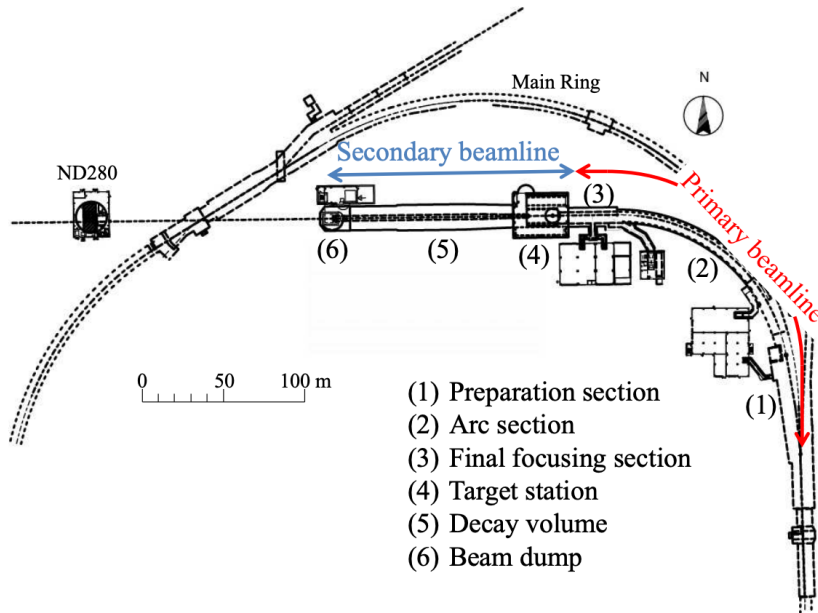


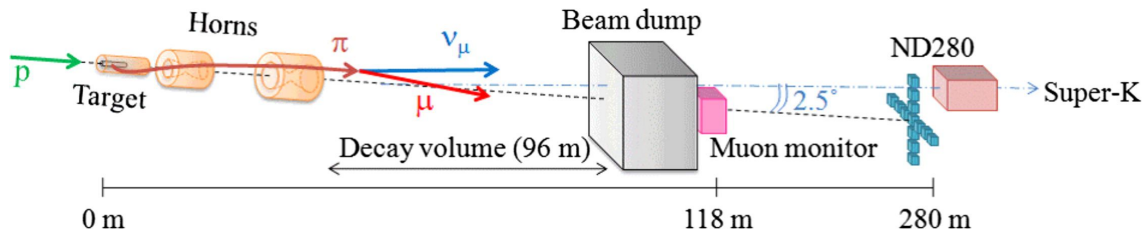
**Figure 2.5:** The near detector suite for the T2K experiment showing the ND280 and INGRID detectors. The distance between the detectors and the beam target is 280m.

733 primary and secondary beamlines. Figure 2.6 illustrates a schematic of the beamline,  
 734 focusing mostly on the components of the secondary beamline. The primary beamline  
 735 has three accelerators that progressively accelerate protons; a linear accelerator, a rapid-  
 736 cycling synchrotron, and the main-ring (MR) synchrotron. Once fully accelerated by  
 737 the MR, the protons have a kinetic energy of 30GeV. Eight bunches of these protons,  
 738 separated by 500ns, are extracted per “spill” from the MR and directed towards a  
 739 graphite target (a rod of length 91.4cm and diameter 2.6cm). Spills are extracted at  
 740 0.5Hz with  $\sim 3 \times 10^{14}$  protons contained per spill.

741 The secondary beamline consists of three main components: the target station, the  
 742 decay volume, and the beam dump. The target station is comprised of the target, beam  
 743 monitors, and three magnetic focusing horns. The proton beam interacts with the  
 744 graphite target to form a secondary beam of mostly pions and kaons. The secondary



(a) Primary and secondary beamline



(b) Secondary beamline

**Figure 2.6:** Top panel: Bird's eye view of the most relevant part of primary and secondary beamline used within the T2K experiment. The primary beamline is the main-ring proton synchrotron, kicker magnet, and graphite target. The secondary beamline consists of the three focusing horns, decay volume, and beam dump. Figure taken from [116]. Bottom panel: The side-view of the secondary beamline including the focusing horns, beam dump and neutrino detectors. Figure taken from [117].

745 beam travels through a 96m long decay volume, generating neutrinos through the  
 746 following decays [59],

$$\begin{aligned}
\pi^+ &\rightarrow \mu^+ + \nu_\mu & \pi^- &\rightarrow \mu^- + \bar{\nu}_\mu \\
K^+ &\rightarrow \mu^+ + \nu_\mu & K^- &\rightarrow \mu^- + \bar{\nu}_\mu \\
&\rightarrow \pi^0 + e^+ + \nu_e & &\rightarrow \pi^0 + e^- + \bar{\nu}_e \\
747 \quad &\rightarrow \pi^0 + \mu^+ + \nu_\mu & &\rightarrow \pi^0 + \mu^- + \bar{\nu}_\mu \\
K_L^0 &\rightarrow \pi^- + e^+ + \nu_e & K_L^0 &\rightarrow \pi^+ + e^- + \bar{\nu}_e \\
&\rightarrow \pi^- + \mu^+ + \nu_\mu & &\rightarrow \pi^+ + \mu^- + \bar{\nu}_\mu \\
\mu^+ &\rightarrow e^+ + \bar{\nu}_\mu + \nu_e & \mu^- &\rightarrow e^- + \nu_\mu + \bar{\nu}_e
\end{aligned}$$

748     The electrically charged component of the secondary beam is focused towards the  
 749    far detector by the three magnetic horns. These horns direct charged particles of a  
 750    particular polarity towards SK whilst defocusing the oppositely charged particles.  
 751    This allows a mostly neutrino or mostly antineutrino beam to be used within the  
 752    experiment, denoted as “forward horn current (FHC)” or “reverse horn current (RHC)”  
 753    respectively.

754     Figure 2.7 illustrates the different contributions to the FHC and RHC neutrino flux.  
 755    The low energy flux is dominated by the decay of pions whereas kaon decay becomes  
 756    the dominant source of neutrinos for  $E_\nu > 3\text{GeV}$ . The “wrong-sign” component,  
 757    which is the  $\bar{\nu}_\mu$  background in a  $\nu_\mu$  beam, and the intrinsic irreducible  $\nu_e$  background,  
 758    are predominantly due to muon decay for  $E_\nu < 2\text{GeV}$ . As the antineutrino **production**  
 759    cross-section is smaller than the neutrino cross-section, the wrong-sign component is  
 760    more dominant in the RHC beam as compared to that in the FHC beam.

761     The beam dump, situated at the end of the decay volume, stops all charged particles  
 762    other than highly energetic muons ( $p_\mu > 5\text{GeV}$ ). The MuMon detector monitors the  
 763    penetrating muons to determine the beam direction and intensity which is used to  
 764    constrain some of the beam flux systematics within the analysis [117, 119].

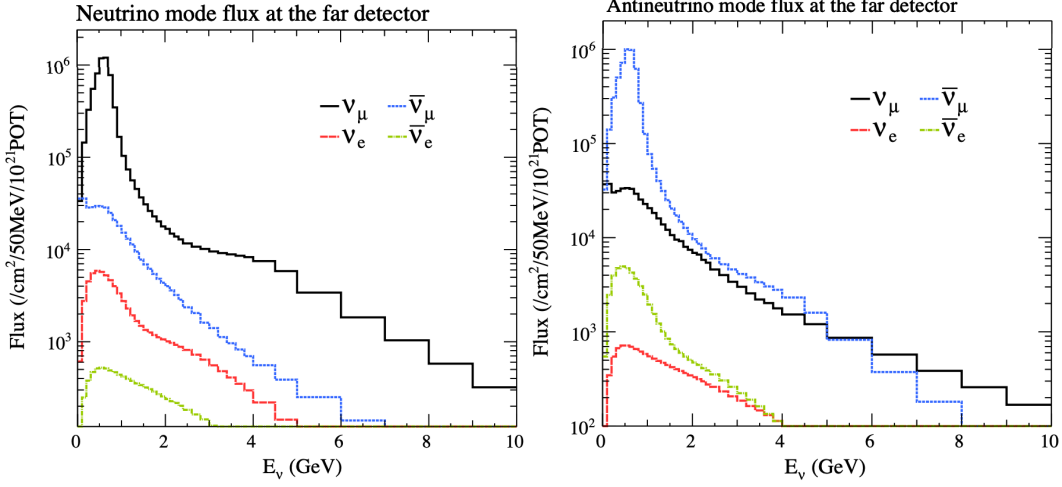


**Figure 2.7:** The Monte Carlo prediction of the energy spectrum for each flavour of neutrino ( $\nu_e$ ,  $\bar{\nu}_e$ ,  $\nu_\mu$  and  $\bar{\nu}_\mu$ ) in the neutrino dominated beam FHC mode (Left) and antineutrino dominated beam RHC mode (Right) expected at SK. Taken from [118].

The T2K experiment uses an off-axis beam to narrow the neutrino energy distribution. This was the first implementation of this technique in a long-baseline neutrino oscillation experiment after its original proposal [120]. Pion decay,  $\pi \rightarrow \mu + \nu_\mu$ , is a two-body decay. Consequently, the neutrino energy,  $E_\nu$ , can be determined based on the pion energy,  $E_\pi$ , and the angle at which the neutrino is emitted,  $\theta$ ,

$$E_\nu = \frac{m_\pi^2 - m_\mu^2}{2(E_\pi - p_\pi \cos(\theta))}, \quad (2.5)$$

where  $m_\pi$  and  $m_\mu$  are the mass of the pion and muon respectively. For a fixed energy pion, the neutrino energy distribution is dependent upon the angle at which the neutrinos are observed from the initial pion beam direction. For the 295km baseline at T2K,  $E_\nu = 0.6\text{GeV}$  maximises the electron neutrino appearance probability,  $P(\nu_\mu \rightarrow \nu_e)$ , whilst minimising the muon disappearance probability,  $P(\nu_\mu \rightarrow \nu_\mu)$ . Figure 2.8 illustrates the neutrino energy distribution for a range of off-axis angles, as well as the oscillation probabilities most relevant to T2K.

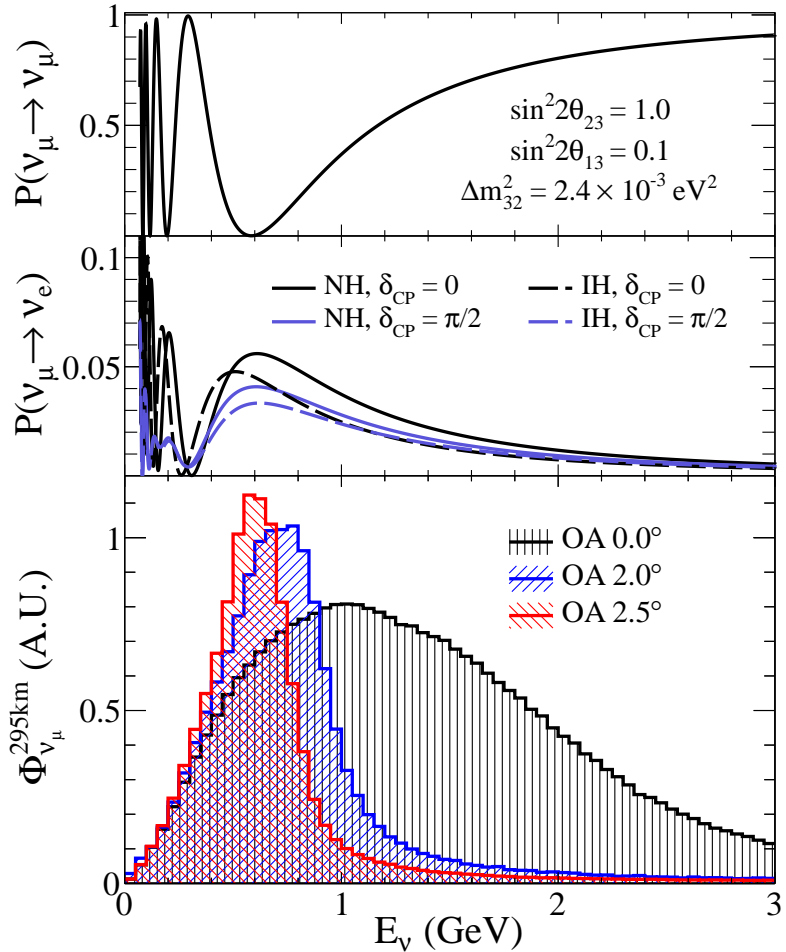


**Figure 2.8:** Top panel: T2K muon neutrino disappearance probability as a function of neutrino energy. Middle panel: T2K electron neutrino appearance probability as a function of neutrino energy. Bottom panel: The neutrino flux distribution for three different off-axis angles (Arbitrary units) as a function of neutrino energy.

## 777 2.2.2 The Near Detector at 280m

778 Whilst all the near detectors are situated in the same “pit” located at 280m from the  
 779 beamline, the “ND280” detector is the off-axis detector which is situated at the same  
 780 off-axis angle as the Super-Kamiokande far detector. It has two primary functions;  
 781 firstly it measures the neutrino flux and secondly it counts the event rates of different  
 782 types of neutrino interactions. Both of these constrain the flux and cross-section  
 783 systematics invoked within the model for a more accurate prediction of the expected  
 784 event rate at the far detector.

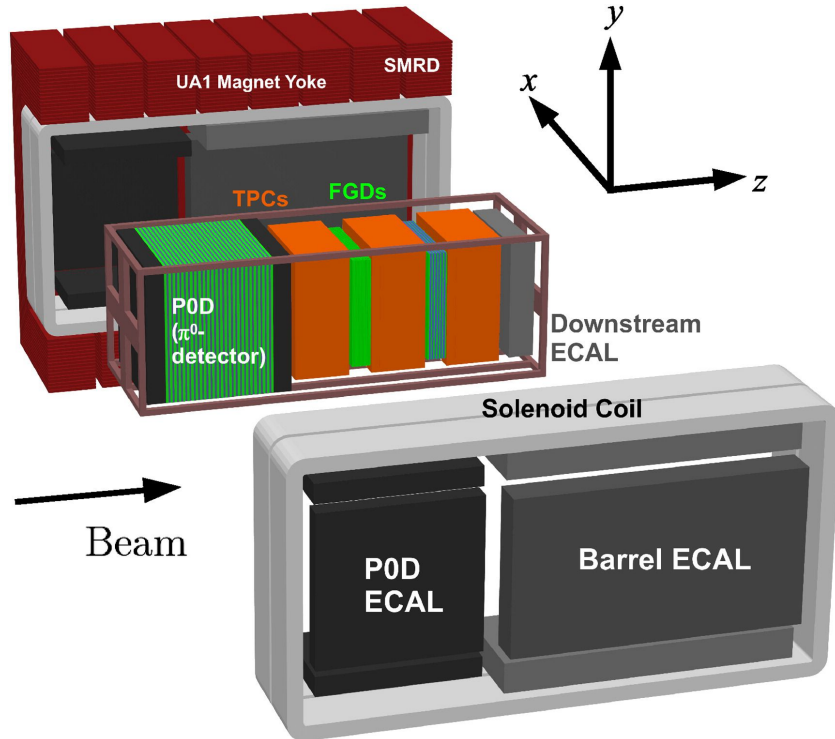


**Figure 2.9:** The components of the ND280 detector. The neutrino beam travels from left to right. Taken from [116].

As illustrated in Figure 2.9, the ND280 detector consists of several sub-detectors.

The most important part of the detector for this analysis is the tracker region. This is comprised of two time projection chambers (TPCs) sandwiched between three fine grain detectors (FGDs). The FGDs contain both hydrocarbon plastics and water targets for neutrino interactions and provide track reconstruction near the interaction vertex. The emitted charged particles can then propagate into the TPCs which provide particle identification and momentum reconstruction. The FGDs and TPCs are further described in subsubsection 2.2.2.1 and subsubsection 2.2.2.2 respectively. The electromagnetic calorimeter (ECAL) encapsulates the tracker region alongside the  $\pi^0$  detector (P0D). The ECAL measures the deposited energy from photons emitted from interactions within the FGD. The P0D constrains the cross-section of neutral current interactions which generate neutral pions, which is one of the largest backgrounds in the electron neutrino appearance oscillation channel. The P0D and ECAL detectors are detailed in subsubsection 2.2.2.3 and subsubsection 2.2.2.4 respectively. The entire

799 detector is located within a large **yolk yoke** magnet which produces a 0.2T magnetic  
800 field. This design of the magnet also includes a scintillating detector called the side  
801 muon range detector (SMRD) which is used to track high-angle muons as well as  
802 acting as a cosmic veto. The SMRD is described in subsubsection 2.2.2.5.

803 **2.2.2.1 Fine Grained Detectors**

804 The T2K tracker region is comprised of two fine grained detectors (FGD) and three  
805 Time Projection Chambers (TPC). A detailed description of the FGD design, construc-  
806 tion, and assembly is found in [121] and summarised below. The FGDs are the primary  
807 target for neutrino interactions with a mass of 1.1 tonnes per FGD. Alongside this,  
808 the FGDs are designed to be able to track short-range particles which do not exit the  
809 FGD. Typically, short-range particles are low momentum and are observed as tracks  
810 that deposit a large amount of energy per unit length. This means the FGD needs  
811 good granularity to resolve these particles. The FGDs have the best timing resolution  
812 ( $\sim 3\text{ns}$ ) of any of the sub-detectors of the ND280 detector. As such, the FGDs are used  
813 for time of flight measurements to **determine distinguish** forward going positively  
814 charged particles from backward going negatively charged particles. Finally, any  
815 tracks which pass through multiple sub-detectors are required to be track matched to  
816 the FGD.

817 Both FGDs are made from square scintillator planes of side length 186cm and  
818 width 2.02cm. Each plane consists of two layers of 192 scintillator bars in an X **or** Y  
819 orientation. A wavelength shifting fiber is threaded through the center of each bar and  
820 is read out by a multi-pixel photon counter (MPPC). FGD1 is the most upstream of  
821 the two FGDs and contains 15 planes of carbon plastic scintillator which is a common  
822 target in external neutrino scattering data. As the far detector is a pure water target, 7  
823 of the 15 scintillator planes in FGD2 have been replaced with a hybrid water-scintillator

824 target. Due to the complexity of the nucleus, nuclear effects can not be extrapolated  
 825 between different nuclei. Therefore having the ability to take data on one target which  
 826 is the same as external data and another target which is the same as the far detector  
 827 target is beneficial for reliable model parameter estimates.

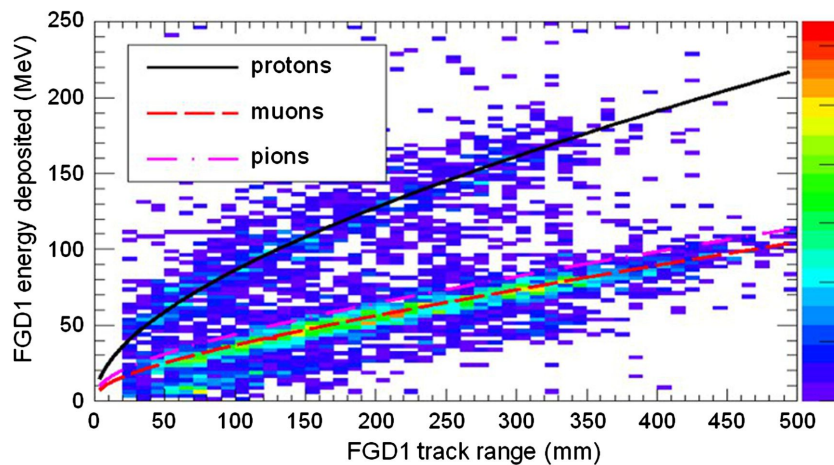


**Figure 2.10:** Comparison of data to Monte Carlo prediction of integrated deposited energy as a function of track length for particles that stopped in FGD1. Taken from [121].

828 The integrated deposited energy is used for particle identification. The FGD  
 829 can distinguish protons from other charged particles by comparing the integrated  
 830 deposited energy from data to Monte Carlo prediction as seen in Figure 2.10.

### 831 2.2.2.2 Time Projection Chambers

832 The majority of particle identification and momentum measurements within ND280  
 833 are provided by three Time Projection Chambers (TPCs) [122]. The TPCs are located  
 834 on either side of the FGDs. They are located inside of the magnetic field meaning the  
 835 momentum of a charged particle can be determined from the bending of the track.

836 Each TPC module consists of two gas-tight boxes, as shown in Figure 2.11, which  
 837 are made of non-magnetic material. The outer box is filled with CO<sub>2</sub> which acts as  
 838 an electrical insulator between the inner box and the ground. The inner box forms

839 the field cage which produces a uniform electric drift field of  $\sim 275\text{V/cm}$  and **is filled**  
 840 **with** an argon gas mixture. Charged particles moving through this gas mixture ionize  
 841 the gas **mixture**. **The and the** ionised charge is drifted towards micromegas detectors  
 842 which measure the ionization charge. The time and position information in the readout  
 843 allows a three-dimensional image of the neutrino interaction.

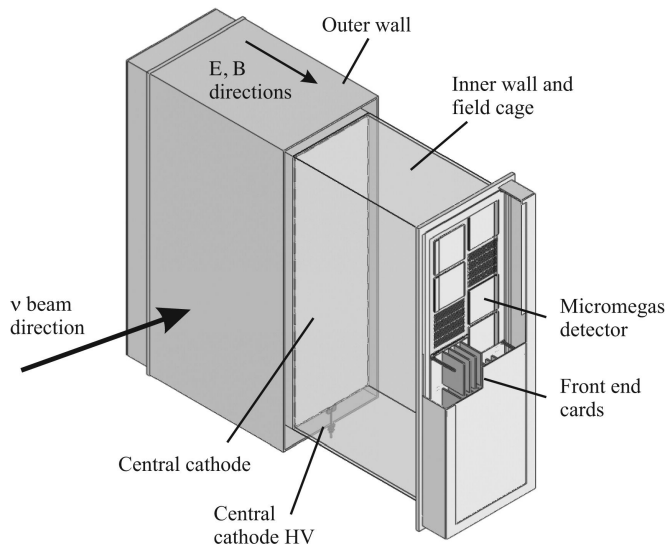
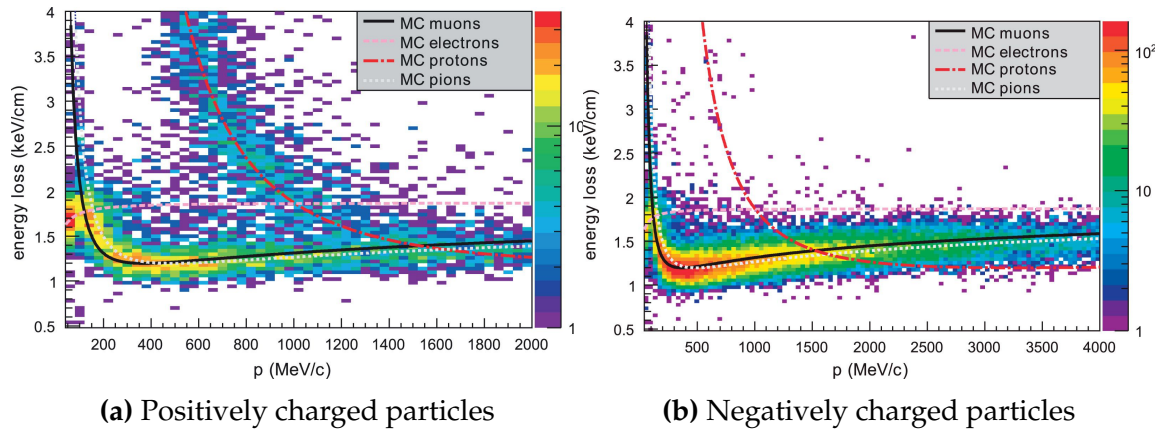


Figure 2.11: Schematic design of a Time Projection Chamber detector. Taken from [122].

844 The particle identification of tracks that pass through the TPCs is performed using  
 845  $dE/dx$  measurements. Figure 2.12 illustrates the data to Monte Carlo distributions  
 846 of the energy lost by a charged particle passing through the TPC as a function of the  
 847 reconstructed particle momentum. The resolution is  $7.8 \pm 0.2\%$  meaning that electrons  
 848 and muons can be distinguished. This allows reliable measurements of the intrinsic  $\nu_e$   
 849 component of the beam.

### 850 2.2.2.3 $\pi^0$ Detector

851 If one of the  $\gamma$ -rays from a  $\pi^0 \rightarrow 2\gamma$  decay is missed at the far detector, the reconstruc-  
 852 tion will determine that event to be **electron-like a charge current  $\nu_e$ -like event**. This  
 853 is one of the main backgrounds hindering the electron neutrino appearance searches.



**Figure 2.12:** The distribution of energy loss as a function of reconstructed momentum for charged particles passing through the TPC, comparing data to Monte Carlo prediction. Taken from [122].

854     Therefore, the  $\pi^0$  detector (P0D) measures the cross-section of the neutral current  
 855     induced neutral pion production on a water target **to constrain this background.**

856     The P0D is a cube of approximately 2.5m length **The P0D consists consisting**  
 857     of layers of scintillating bars, brass and lead sheets, and water bags as illustrated in  
 858     Figure 2.13. Two electromagnetic calorimeters are positioned at the most upstream  
 859     and most downstream position in the sub-detector and the water target is situated in  
 860     between them. The scintillator layers are built from two triangular bars orientated  
 861     in opposite directions to form a rectangular layer. Each triangular scintillator bar is  
 862     threaded with optical fiber which is read out by MPPCs. The high-Z brass and lead  
 863     regions produce electron showers from the photons emitted in  $\pi^0$  decay.

864     The sub-detector can generate measurements of NC1 $\pi^0$  cross-sections on a water  
 865     target by measuring the event rate both with and without the water target, with the  
 866     cross-section on a water target being determined as the difference. The total active  
 867     mass is 16.1 tonnes when filled with water and 13.3 tonnes when empty.

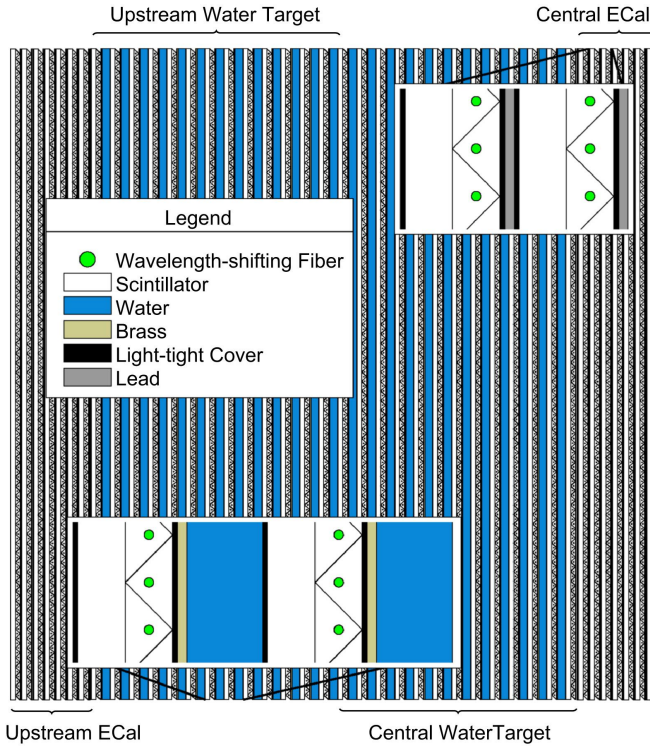


**Figure 2.13:** A schematic of the P0D side-view. Taken from [123].

#### 868 2.2.2.4 Electromagnetic Calorimeter

869 The electromagnetic calorimeter [124] (ECal) encapsulates the P0D and tracking sub-  
 870 detectors. Its primary purpose is to aid  $\pi^0$  reconstruction from any interaction in  
 871 the tracker. To do this, it measures the energy and direction of photon showers from  
 872  $\pi^0 \rightarrow 2\gamma$  decay. It can also distinguish pion and muon tracks depending on the shape  
 873 of the photon shower deposited.

874 The ECal is comprised of three sections; the P0D ECal which surrounds the P0D,  
 875 the barrel ECal which encompasses the tracking region, and the downstream ECal  
 876 which is situated downstream of the tracker region. The barrel and downstream  
 877 ECals are tracking calorimeters that focus on electromagnetic showers from high-angle  
 878 particles emitted from the tracking sub-detectors. Particularly in the TPC, high-angle  
 879 tracks (those which travel perpendicularly to the beam-axis) can travel along a single  
 880 scintillator bar resulting in very few hits. The width of the barrel and downstream

881 ECal corresponds to  $\sim 11$  electron radiation lengths to ensure  ~~$\sim 50\%$  of the energy~~  
882 ~~of the  $\pi^0$  is contained a significant amount of the  $\pi^0$  energy is contained~~. As the  
883 P0D has its own calorimetry which reconstructs showers, the P0D ECal determines  
884 the energy which escapes the P0D.

885 Each ECal is constructed of multiple layers of scintillating bars sandwiched between  
886 lead sheets. The scintillating bars are threaded with optical fiber and read out by  
887 MPPCs. Each sequential layer of the scintillator is orientated perpendicular to the  
888 previous which allows a ~~two-dimensional readout, which when temporal, information is included results in three-dimension event displays three dimensional event displays~~. The target mass of the P0D ECal, barrel ECal, and downstream ECal are 1.50,  
889 4.80 and 6.62 tonnes respectively.

892 **2.2.2.5 Side Muon Range Detector**

893 As illustrated in Figure 2.9, the ECal, FGDs, P0D, and TPCs are enclosed within the  
894 UA1 magnet. Originally designed for the NOMAD [125] experiment and reconditioned  
895 for use in the T2K experiment [126], the UA1 magnet provides a uniform horizontal  
896 magnetic field of  ~~$0.2 \pm 2 \times 10^{-4}$ T~~  $0.2$ T with an uncertainty of  $2 \times 10^{-4}$ T.

897 Built into the UA1 magnet, the side muon range detector (SMRD) [127] monitors  
898 high-energy muons which leave the tracking region and permeate through the ECal.  
899 It additionally acts as a cosmic muon veto and trigger.

900 **2.2.3 The Interactive Neutrino GRID**

901 The Interactive Neutrino GRID (INGRID) detector is situated within the same “pit” as  
902 the other near detectors. It is aligned with the beam in the “on-axis” position and mea-  
903 sures the beam direction, spread, and intensity. The detector was originally designed

904 with 16 identical modules [116] (two modules have since been decommissioned) and a  
905 “proton” module. The design of the detector is cross-shaped with length and height  
906  $10\text{m} \times 10\text{m}$  as illustrated in Figure 2.14.

907 Each module is composed of iron sheets interlaced with eleven tracking scintillator  
908 planes for a total target mass of 7.1 tonnes per module. The scintillator design is an X-Y  
909 pattern of 24 bars in both orientations, where each bar contains wave-length shifting  
910 fibers which are connected to multi-pixel photon counters (MPPCs). **The MPPCs con-**  
**vert detected photons into electrical signals via photodiodes. This is then read out**  
**by Trip-T front-end electronics and passed to the readout merging modules along**  
**with timing information from the clock module.** Each module is encapsulated inside  
914 veto planes to aid the rejection of charged particles entering the module.

915 The proton module is different from the other modules in that it consists of entirely  
916 scintillator planes with no iron target. The scintillator bars are also smaller than those  
917 used in the other modules to increase the granularity of the detector and improve  
918 tracking capabilities. The module sits in the center of the beamline and is designed to  
919 give precise measurements of quasi-elastic charged current interactions to evaluate  
920 the performance of the Monte Carlo simulation of the beamline.

921 The INGRID detector can measure the beam direction to an uncertainty of 0.4mrad  
922 and the beam center within a resolution of 10cm [116]. The beam direction in both the  
923 vertical and horizontal directions is discussed in [128] and it is found to be in good  
924 agreement with the MUMON monitor described in subsection 2.2.1.

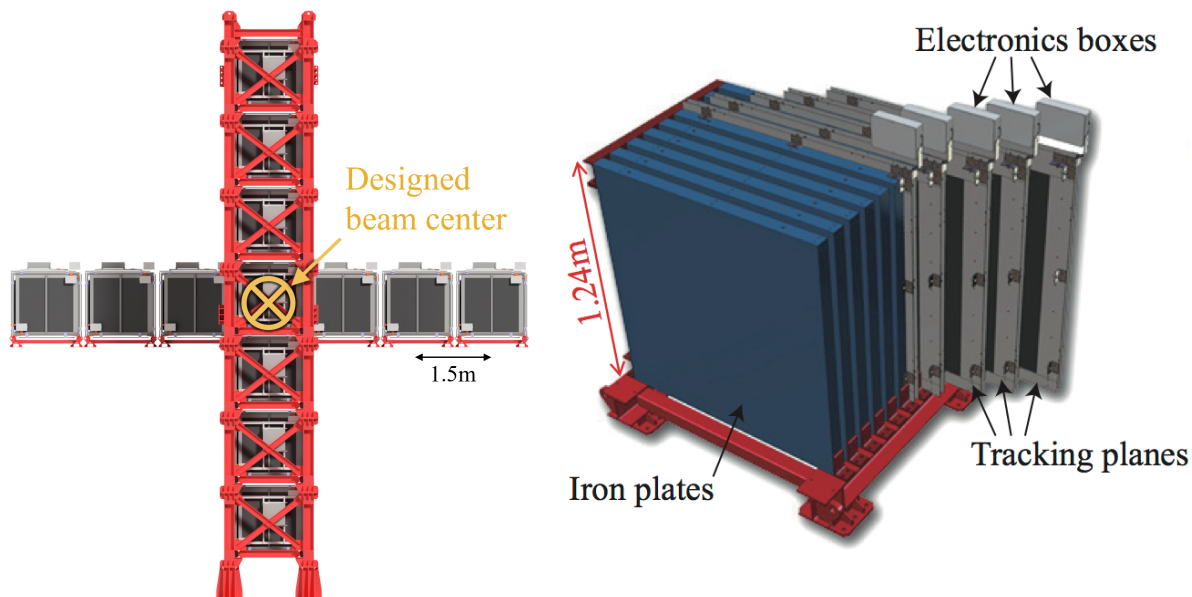


**Figure 2.14:** Left panel: The Interactive Neutrino GRID on-axis Detector. 14 modules are arranged in a cross-shape configuration, with the center modules being directly aligned with the on-axis beam. Right panel: The layout of a single module of the INGRID detector. Both figures are recreated from [116].

925

# Chapter 3

926

## Bayesian Statistics and Markov Chain 927 Monte Carlo Techniques

928 ~~The analysis throughout this thesis is based upon~~ This thesis presents a Bayesian  
929 oscillation analysis. To extract the oscillation parameters, a Markov Chain Monte  
930 Carlo (MCMC) method is used. This chapter explains the theory of how parameter  
931 estimates can be determined using this technique and condenses the material found in  
932 the literature [129–132].

933 The oscillation parameter determination presented within this thesis is built upon  
934 a ~~a simultaneous fit to the near detector, far detector beam, and atmospheric neutrino data~~  
935 ~~a simultaneous fit to neutrino beam data in the near detector, beam data~~  
936 ~~at SK and atmospheric data at SK~~. In total, there are four oscillation parameters of  
937 interest ( $\sin^2(\theta_{23})$ ,  $\sin^2(\theta_{13})$ ,  $\Delta m_{23}^2$ , and  $\delta_{CP}$ ), two oscillation parameters to which  
938 this study will not be sensitive ( $\sin^2(\theta_{12})$ ,  $\Delta m_{12}^2$ ) and many nuisance parameters  
939 that control the systematic uncertainty models invoked within this study. ~~The systematic~~  
940 ~~uncertainties can be grouped into categories depending on how they are~~  
941 ~~defined: 574 bin-normalisations due to the near detector response, 45 bin-normali-~~  
942 ~~sations to describe the far detector response to neutrino beam events, 27 parameters~~  
943 ~~to describe the detector response to atmospheric neutrino events, 100 to model the~~  
944 ~~bin-normalisation due to beam flux uncertainties, 18 which model the atmospheric~~  
945 ~~flux uncertainties, and 87 to describe the correlated cross-section model. An alter-~~  
946 ~~native parameterisation, where the far detector response is correlated between the~~

947 ~~beam and atmospheric samples, replaces the bin normalisation parameters with~~  
 948 ~~224 shift and smear systematics. Section Link to Systematics Chapter describes the~~  
 949 ~~systematic model in more depth.~~

950 The MCMC technique generates a multi-dimensional probability distribution across  
 951 all of the model parameters used in the fit. To determine the parameter estimate of a  
 952 single parameter, this multi-dimensional object is integrated over all other parameters.  
 953 This process is called Marginalisation and is further described in subsection 3.3.1.  
 954 Monte Carlo techniques approximate the probability distribution of each parameter  
 955 within the limit of generating infinite samples. As ever, generating a large number of  
 956 samples is time and resource-dependent. Therefore, an MCMC technique is utilised  
 957 within this analysis to reduce the required number of steps to sufficiently sample the  
 958 parameter space. This technique is described in further detail in subsection 3.2.1.

### 959 3.1 Bayesian Statistics

960 ~~According to Bayesian Inference, observables and parameters of a statistical model~~  
 961 ~~are treated on an equal footing. To estimate model parameters  $\vec{\theta}$  from some data~~  
 962  ~~$D$ , one needs to define the joint probability distribution  $P(D|\vec{\theta})$  which Bayesian~~  
 963 ~~inference treats observable data,  $D$ , and model parameters,  $\vec{\theta}$ , on equal footing such~~  
 964 ~~that a probability model of both data and parameters is required. This is the joint~~  
 965 ~~probability distribution  $P(D, \vec{\theta})$  and~~ can be described ~~as by~~ the prior distribution for  
 966 model parameters  $P(\vec{\theta})$  and the likelihood of the data given the model parameters  
 967  $P(D|\vec{\theta})$ ,

$$P(D, \vec{\theta}) = P(D|\vec{\theta})P(\vec{\theta}). \quad (3.1)$$

The prior distribution,  $P(\vec{\theta})$ , describes all previous knowledge about the parameters within the model. For example, if the risk of developing health problems is known to increase with age, the prior distribution would describe the increase. For the purpose of this analysis, the prior distribution is typically the best-fit values taken from external data measurements with a Gaussian uncertainty. The prior distribution can also contain correlations between model parameters. In an analysis using Monte Carlo techniques, the likelihood of measuring some data assuming some set of model parameters is calculated by comparing the Monte Carlo prediction generated at that particular set of model parameters to the data.

It is parameter estimation that is important for this analysis and as such, we apply Bayes' theorem [133] to calculate the probability for each parameter to have a certain value given the observed data,  $P(\vec{\theta}|D)$ , which is known as the posterior distribution (often termed the posterior). This can be expressed as

$$P(\vec{\theta}|D) = \frac{P(D|\vec{\theta})P(\vec{\theta})}{\int P(D|\vec{\theta})P(\vec{\theta})d\vec{\theta}}. \quad (3.2)$$

The denominator in Equation 3.2 is the integral of the joint probability distribution over all values of all parameters used within the fit. For brevity, we say that the posterior distribution is

$$P(\vec{\theta}|D) \propto P(D|\vec{\theta})P(\vec{\theta}). \quad (3.3)$$

In subsection 3.3.1, we see that for the cases used within this analysis, it is reasonable to know the posterior to some normalisation constant.

## 986 3.2 Monte Carlo Simulation

987 Monte Carlo techniques are used to numerically solve a complex problem that does  
988 not necessarily have an analytical solution. These techniques rely on building a large  
989 ensemble of samples from an unknown distribution and then using the ensemble to  
990 approximate the properties of the distribution.

991 An example that uses Monte Carlo techniques is to calculate the area underneath  
992 a curve. For example, take the problem of calculating the area under a straight line  
993 with gradient  $M = 0.4$  and intercept  $C = 1.0$ . Analytically, one can calculate the area  
994 under the line is equal to 30 units for  $0 \leq x \leq 10$ . Using Monte Carlo techniques,  
995 one can calculate the area under this line by throwing many random values for the  $x$   
996 and  $y$  components of each sample and then calculating whether that point falls below  
997 the line. The area can then be calculated by the ratio of points below the line to the  
998 total number of samples thrown multiplied by the total area in which samples were  
999 scattered. The study is shown in Figure 3.1 highlights this technique and finds the area  
1000 under the curve to be 29.9 compared to an analytical solution of 30.0. The deviation  
1001 of the numerical to analytical solution can be attributed to the number of samples  
1002 used in the study. The accuracy of the approximation in which the properties of the  
1003 Monte Carlo samples replicate those of the desired distribution is dependent on the  
1004 number of samples used. Replicating this study with a differing number of Monte  
1005 Carlo samples used in each study (As shown in Figure 3.2) highlights how the Monte  
1006 Carlo techniques are only accurate within the limit of a high number of samples.

1007 Whilst the above example has an analytical solution, these techniques are just as  
1008 applicable to complex solutions. Clearly, any numerical solution is only as useful as its  
1009 efficiency. As discussed, the accuracy of the Monte Carlo technique is dependent upon  
1010 the number of samples generated to approximate the properties of the distribution.

Furthermore, if the positions at which the samples are evaluated are not ‘cleverly’ picked, the efficiency of the Monte Carlo technique significantly drops. Given the example in Figure 3.1, if the region in which the samples are scattered significantly extends passed the region of interest, many calculations will be calculated but do not add to the ability of the Monte Carlo technique to achieve the correct result. For instance, any sample evaluated at a  $y \geq 5$  could be removed without affecting the final result. This does bring in an aspect of the ‘chicken and egg’ problem in that to achieve efficient sampling, one needs to know the distribution beforehand.

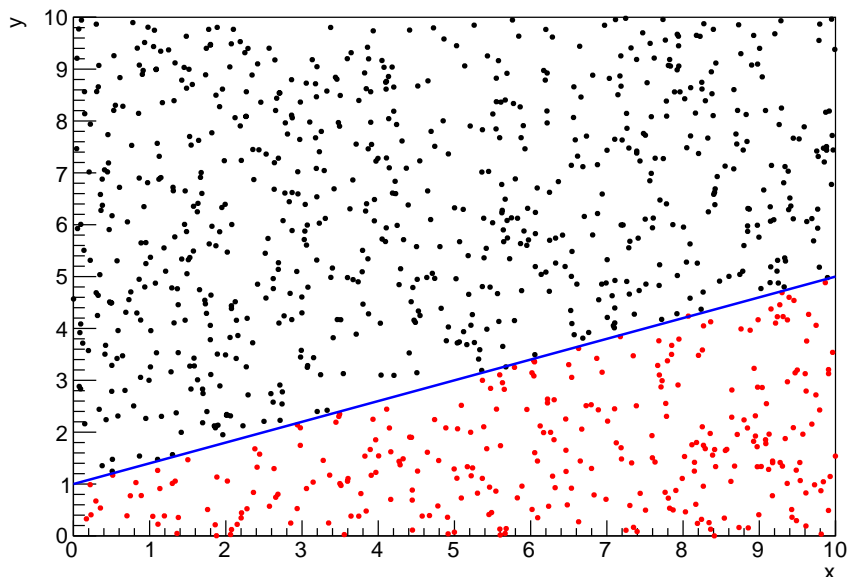


**Figure 3.1:** Example of using Monte Carlo techniques to find the area under the blue line. The gradient and intercept of the line are 0.4 and 1.0 respectively. The area found to be under the curve using one thousand samples is 29.9 units.

### 3.2.1 Markov Chain Monte Carlo

This analysis utilises a multi-dimensional probability distribution, with some dimensions being significantly more constrained than others. This could be from prior knowledge of parameter distributions from external data or un-physical regions in

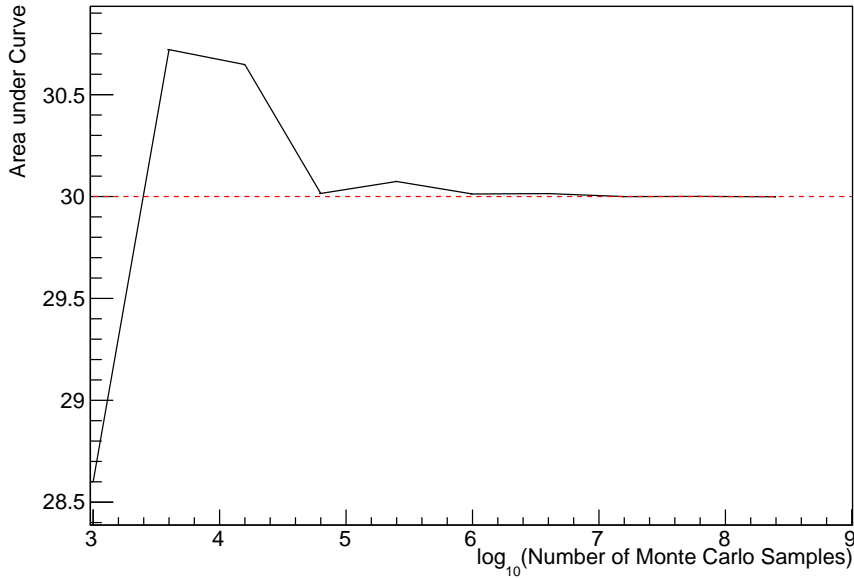


**Figure 3.2:** The area under a line of gradient 0.4 and intercept 1.0 for the range  $0 \leq x \leq 10$  as calculated using Monte Carlo techniques as a function of the number of samples used in each repetition. The analytical solution to the area is 30 units as given by the red line.

which parameters can not exist. Consequently, the Monte Carlo techniques used need to be as efficient as possible. For this analysis, the Markov Chain Monte Carlo (MCMC) technique is chosen. An MCMC technique is a Monte Carlo technique that uses a Markov chain to select which points at which to sample the parameter distribution. This technique performs a semi-random stochastic walk through the allowable parameter space. This builds a posterior distribution which has the property that the density of sampled points is proportional to the probability density of that parameter. This does mean that the samples produced by this technique are not statistically independent but they will cover the space of the distribution.

A Markov chain functions by selecting the position of step  $\vec{x}_{i+1}$  based on the position of  $\vec{x}_i$ . The space in which the Markov chain selects samples is dependent upon the total number of parameters utilised within the fit, where a discrete point in this space is described by the N-dimensional space  $\vec{x}$ . In a perfectly operating Markov chain, the position of the next step depends solely on the previous step and not on the

1037 further history of the chain ( $\vec{x}_0, \vec{x}_1$ , etc.). However, in solving the multi-dimensionality  
 1038 of the fit used within this analysis, each step becomes correlated with several of  
 1039 the steps preceding itself. This behaviour is further explained in subsection 3.2.3.  
 1040 Providing the MCMC chain is well optimised, it will begin to converge towards a  
 1041 unique stationary distribution. The period between the chain's initial starting point  
 1042 and the convergence to the unique stationary distribution is colloquially known as the  
 1043 burn-in period. This is discussed further in subsection 3.2.3. Once the chain reaches  
 1044 the stationary distribution, all points sampled after that point will look like samples  
 1045 from that distribution.

1046 Further details of the theories underpinning MCMC techniques are discussed  
 1047 in [130] but can be summarised by the requirement that the chain satisfies the three  
 1048 'regularity conditions':

- 1049     • Irreducibility: From every position in the parameter space  $\vec{x}$ , there must exist a  
 1050       non-zero probability for every other position in the parameter space to be reached.
- 1051     • Recurrence: Once the chain arrives at the stationary distribution, every step fol-  
 1052       lowing from that position must be samples from the same stationary distribution.
- 1053     • Aperiodicity: The chain must not repeat the same sequence of steps at any point  
 1054       throughout the sampling period.

1055 The output of the chain after burn-in (ie. the sampled points after the chain  
 1056 has reached the stationary distribution) can be used to approximate the posterior  
 1057 distribution and model parameters  $\vec{\theta}$ . To achieve the requirement that the unique  
 1058 stationary distribution found by the chain be the posterior distribution, one can use  
 1059 the Metropolis-Hastings algorithm. This guides the stochastic process depending on  
 1060 the likelihood of the current proposed step compared to that of the previous step.  
 1061 Implementation and other details of this technique are discussed in subsection 3.2.2.

---

### 1062 3.2.2 Metropolis-Hastings Algorithm

1063 As a requirement for MCMCs, the Markov chain implemented in this technique must  
 1064 have a unique stationary distribution that is equivalent to the posterior distribution.  
 1065 To ensure this requirement and that the regularity conditions are met, this analysis  
 1066 utilises the Metropolis-Hastings (MH) algorithm [134, 135]. For the  $i^{th}$  step in the chain,  
 1067 the MH algorithm determines the position in the parameter space to which the chain  
 1068 moves to based on the current step,  $\vec{x}_i$ , and the proposed step,  $\vec{y}_{i+1}$ . The proposed step  
 1069 is randomly selected from some proposal function  $f(\vec{x}_{i+1}|\vec{x}_i)$ , which depends solely  
 1070 on the current step (ie. not the further history of the chain). The next step in the chain  
 1071  $\vec{x}_{i+1}$  can be either the current step or the proposed step determined by whether the  
 1072 proposed step is accepted or rejected. To decide if the proposed step is selected, the  
 1073 acceptance probability,  $\alpha(\vec{x}_i, \vec{y}_i)$ , is calculated as

$$\alpha(\vec{x}_i, \vec{y}_{i+1}) = \min\left(1, \frac{P(\vec{y}_{i+1}|D)f(\vec{x}_i|\vec{y}_{i+1})}{P(\vec{x}_i|D)f(\vec{y}_{i+1}|\vec{x}_i)}\right). \quad (3.4)$$

1074 Where  $P(\vec{y}_{i+1}|D)$  is the posterior distribution as introduced in section 3.1. To  
 1075 simplify this calculation, the proposal function is required to be symmetric such that  
 1076  $f(\vec{x}_i|\vec{y}_{i+1}) = f(\vec{y}_{i+1}|\vec{x}_i)$ . In practice, a multi-variate Gaussian distribution is used to  
 1077 throw parameter proposals from. This reduces Equation 3.4 to

$$\alpha(\vec{x}_i, \vec{y}_{i+1}) = \min\left(1, \frac{P(\vec{y}_{i+1}|D)}{P(\vec{x}_i|D)}\right). \quad (3.5)$$

After calculating this quantity, a random number,  $\beta$ , is generated uniformly between 0 and 1. If  $\beta \leq \alpha(\vec{x}_i, \vec{y}_{i+1})$ , the proposed step is accepted. Otherwise, the chain sets the next step equal to the current step and this procedure is repeated. This can be interpreted as if the posterior probability of the proposed step is greater than that of the current step, ( $P(\vec{y}_{i+1}|D) \geq P(\vec{x}_i|D)$ ), the proposed step will always be accepted. If the opposite is true, ( $P(\vec{y}_{i+1}|D) \leq P(\vec{x}_i|D)$ ), the proposed step will be accepted with probability  $P(\vec{x}_i|D)/P(\vec{y}_{i+1}|D)$ . This ensures that the Markov chain does not get trapped in any local minima in the potentially non-Gaussian posterior distribution. The outcome of this technique is that the density of steps taken in a discrete region is directly proportional to the probability density in that region.

### **3.2.3 MCMC Optimisation**

As discussed in subsection 3.2.2, the proposal function invoked within the MH algorithm can take any form and the chain will still converge to the stationary distribution. ~~As discussed in Link to Analysis Strategy Section, this analysis performs the Monte Carlo reweighting on an event-by-event basis. This requires significant computational resources to perform a parameter fit At each set of proposed parameter values, a prediction of the same spectra has to be generated which requires significant computational resources.~~ Therefore, the number of steps taken before the unique stationary distribution is found should be minimised as only steps after convergence add information to the **fit oscillation analysis**. Furthermore, the chain should entirely cover the allowable parameter space to ensure that all values have been considered. Tuning the distance that the proposal function jumps between steps on a parameter-by-parameter basis can both minimise the length of the burn-in period and ensure that the correlation between step  $\vec{x}_i$  and  $\vec{x}_j$  is sufficiently small.

1102        The effect of changing the width of the proposal function is highlighted in Figure 3.3.  
1103        Three scenarios, each with the same underlying stationary distribution (A Gaussian of  
1104        width 1.0 and mean 0.), are presented. The only difference between the three scenarios  
1105        is the width of the proposal function, colloquially known as the ‘step size  $\sigma$ ’. Each  
1106        scenario starts at an initial parameter value of 10.0 which would be considered an  
1107        extreme variation. For the case where  $\sigma = 0.1$ , it is clear to see that the chain takes  
1108        a long time to reach the expected region of the parameter. This indicates that this  
1109        chain would have a large burn-in period and does not converge to the stationary  
1110        distribution until step  $\sim 500$ . Furthermore, whilst the chain does move towards the  
1111        expected region, each step is significantly correlated with the previous. Considering  
1112        the case where  $\sigma = 5.0$ , the chain approaches the expected parameter region almost  
1113        instantly meaning that the burn-in period is not significant. However, there are clearly  
1114        large regions of steps where the chain does not move. This is likely due to the chain  
1115        proposing steps in the tails of the distribution which have a low probability of being  
1116        accepted. Consequently, this chain would take a significant number of steps to fully  
1117        span the allowable parameter region. For the final scenario, where  $\sigma = 0.5$ , you can see  
1118        a relatively small burn-in period of approximately 100 steps. Once the chain reaches  
1119        the stationary distribution, it moves throughout the expected region of parameter  
1120        values many times, sufficiently sampling the full parameter region. This example is a  
1121        single parameter varying across a continuous distribution and does not fully reflect  
1122        the difficulties in the many-hundred multi-variate parameter distribution used within  
1123        this analysis. However, it does give a conceptual idea of the importance of selecting  
1124        the proposal function and associated step size.

1125        As discussed, step size tuning directly correlates to the average step acceptance  
1126        rate. If the step size is too small, many steps will be accepted but the chain moves  
1127        slowly. If the opposite is true, many steps will be rejected as the chain proposes steps  
1128        in the tails of the distribution. Discussion in [136] suggests that the ‘ideal’ acceptance

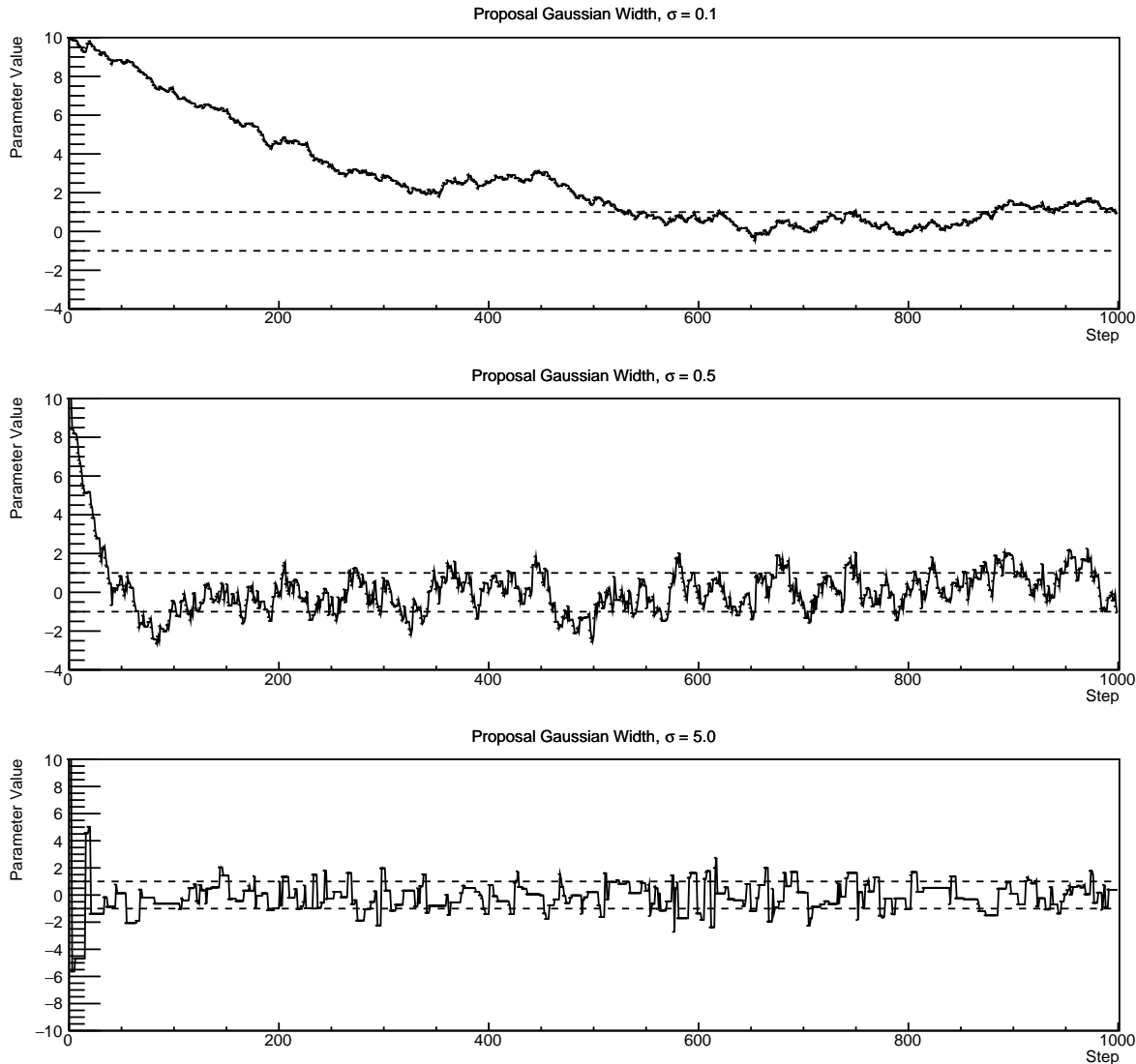


**Figure 3.3:** Three MCMC chains, each with a stationary distribution equal to a Gaussian centered at 0 and width 1 (As indicated by the black dotted lines). All of the chains use a Gaussian proposal function but have different widths (or ‘step size  $\sigma$ ’). The top panel has  $\sigma = 0.1$ , middle panel has  $\sigma = 0.5$  and the bottom panel has  $\sigma = 5.0$ .

<sup>1129</sup> rate of a high dimension MCMC chain should be approximately  $\sim 25\%$ . An “ideal”

<sup>1130</sup> step size [136] of

$$\sigma = \frac{2.4}{N_p}, \quad (3.6)$$

1131 where  $N_p$  is the number of parameters included in the MCMC fit. However, the  
 1132 complex correlations between systematics mean that some parameters have to be hand  
 1133 tuned and many efforts have been taken to select a set of parameter-by-parameter step  
 1134 sizes to approximately reach the ideal acceptance rate.

1135 Figure 3.3 highlights the likelihood as calculated by the fit in [DB: Link to AsimovA](#)  
 1136 [Sensitivity Section](#) as a function of the number of steps in each chain. In practice,  
 1137 many independent MCMC chains are run simultaneously to parallelise the task of  
 1138 performing the fit. This figure overlays the distribution found in each chain. As seen,  
 1139 the likelihood decreases from its initial value and converges towards a stationary  
 1140 distribution after  $\sim 1 \times 10^5$  steps. ~~Each fit (whether it be different asimov fits or data~~  
~~fit) will have a different set of preferred parameter values which results in a differ-~~  
~~ent stationary distribution. For each fit presented in this thesis, a burn-in period of~~  
~~1  $\times 10^5$  steps was found to be sufficient.~~

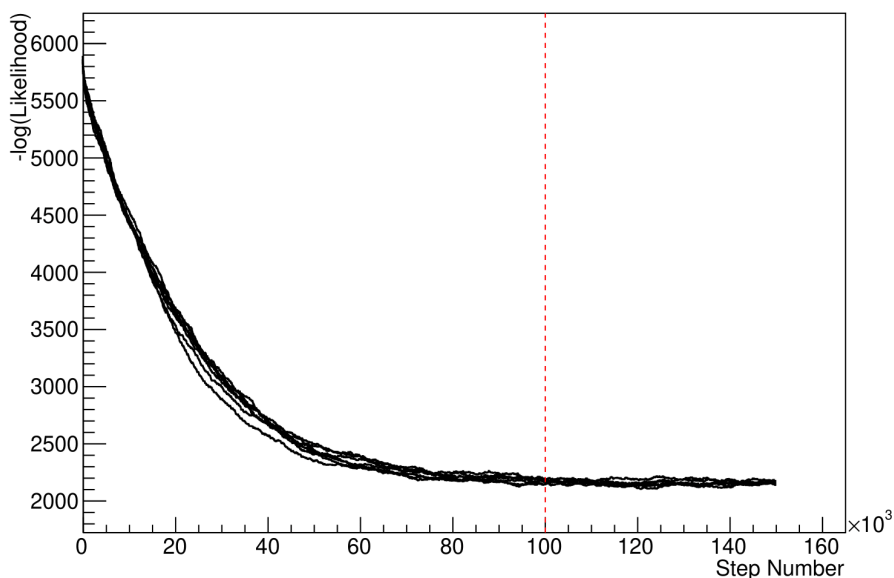


**Figure 3.4:** The log-likelihood from the fit detailed in [DB: Link to AsimovA](#) [Sensitivity Section](#) as a function of the number of steps accumulated in each fit. Many independent MCMC chains were run in parallel and overlaid on this plot. The red line indicates the  $1 \times 10^5$  step burn-in period after which the log-likelihood becomes stable.

1144     Multiple configurations of this analysis have been performed throughout this  
1145     thesis where different samples or systematics have been used. For all of these  
1146     configurations, it was found that a burnin period of  $1 \times 10^5$  was sufficient in all  
1147     cases.

### 1148 3.3 Understanding the MCMC Results

1149     Whilst [Link](#) and [Link](#) describe how to interpret Bayesian statistics and explains the  
1150     MCMC techniques used within this analysis, there is no mention of how to inter-  
1151     pret the output of the chain. The previous sections have described how to generate  
1152     the posterior probability distribution using Bayesian MCMC techniques. How-  
1153     ever, this analysis focuses on oscillation parameter determination. The posterior  
1154     distribution output from the chain is a high dimension object, with as many dimen-  
1155     sions as there are parameters included in the [fit oscillation analysis](#). However, this  
1156     multi-dimensional object is difficult to conceptualize so parameter estimations are  
1157     often presented in one or two-dimensional projections of this probability distribution.  
1158     To do this, we invoke the marginalisation technique highlighted in subsection 3.3.1.

#### 1159 3.3.1 Marginalisation

1160     The output of the MCMC chain is a highly dimensional probability distribution  
1161     which is very difficult to interpret. From the standpoint of an oscillation analysis  
1162     experiment, the one or two-dimensional ‘projections’ of the oscillation parameters of  
1163     interest are most relevant. Despite this, the best fit values and uncertainties on the  
1164     oscillation parameters of interest should correctly encapsulate the correlations to the  
1165     other systematic uncertainties (colloquially called ‘nuisance’ parameters). For this joint  
1166     beam and atmospheric analysis, the oscillation parameters of interest are  $\sin^2(\theta_{23})$ ,

1167  $\sin^2(\theta_{13})$ ,  $\Delta m_{23}^2$ , and  $\delta_{CP}$ . All other parameters (Including the oscillation parameter  
1168 this fit is insensitive to) are deemed nuisance parameters. To generate these projections,  
1169 we rely upon integrating the posterior distribution over all nuisance parameters. This  
1170 is called marginalisation. A simple example of this technique is to imagine the scenario  
1171 where two coins are flipped. To determine the probability that the first coin returned  
1172 a ‘head’, the exact result of the second coin flip is disregarded and simply integrated  
1173 over. For the parameters of interest,  $\vec{\theta}_i$ , we can calculate the marginalised posterior by  
1174 integrating over the nuisance parameters,  $\vec{\theta}_n$ . In this case, Equation 3.2 becomes

$$P(\vec{\theta}_i|D) = \frac{\int P(D|\vec{\theta}_i, \vec{\theta}_n)P(\vec{\theta}_i, \vec{\theta}_n)d\vec{\theta}_n}{\int P(D|\vec{\theta})P(\vec{\theta})d\vec{\theta}} \quad (3.7)$$

1175 Where  $P(\vec{\theta}_i, \vec{\theta}_n)$  encodes the prior knowledge about the uncertainty and correlations  
1176 between the parameters of interest and the nuisance parameters. In practice, this  
1177 is simply taking the one or two-dimensional projection of the multi-dimensional  
1178 probability distribution.

1179 Whilst in principle an easy solution to a complex problem, correlations between the  
1180 interesting and nuisance parameters can bias the marginalised results. A similar effect  
1181 is found when the parameters being marginalised over have non-Gaussian probability  
1182 distributions. For example, Figure 3.5 highlights the marginalisation bias in the  
1183 probability distribution found for a parameter when requiring a correlated parameter  
1184 to have a positive parameter value. Due to the complex nature of this oscillation  
1185 parameter fit presented in this thesis, there are certainly correlations occurring between  
1186 the oscillation parameters of interest and the other nuisance parameters included in  
1187 the fit.

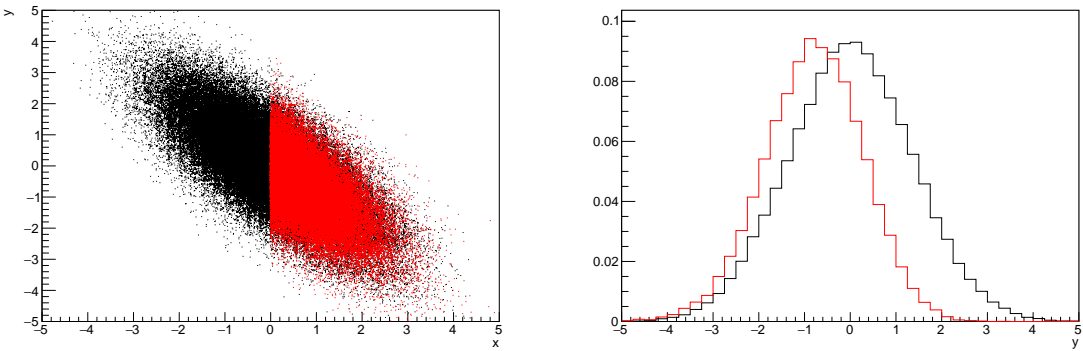


**Figure 3.5:** Left: The two dimensional probability distribution for two correlated parameters  $x$  and  $y$ . The red distribution shows the two dimensional probability distribution when  $0 \leq x \leq 5$ . Right: The marginalised probability distribution for the  $y$  parameter found when requiring the  $x$  to be bound between  $-5 \leq x \leq 5$  for the black and red distribution, respectively.

### 1188 3.3.2 Parameter Estimation and Credible Intervals

1189 The purpose of this analysis is to determine the best fit values for the oscillation  
 1190 parameters that the beam and atmospheric samples are sensitive to:  $\sin^2(\theta_{23})$ ,  $\sin^2(\theta_{13})$   
 1191 ,  $\Delta m_{23}^2$ , and  $\delta_{CP}$ . Typically, the results presented take the form of one or two-dimension  
 1192 marginalised probability distributions for the appearance ( $\sin^2(\theta_{13})$  and  $\delta_{CP}$ ) and  
 1193 disappearance ( $\sin^2(\theta_{23})$  and  $\Delta m_{23}^2$ ) parameters. The posterior probability density  
 1194 taken from the output MCMC chain is binned in these parameters. The parameter  
 1195 best-fit point is then taken to be the value that has the highest posterior probability.  
 1196 This is performed in both one and two-dimensional projections.

1197 However, the single best-fit point in a given parameter is not of much use on its  
 1198 own. We would also like to determine the uncertainty, or credible interval, on that  
 1199 best-fit point. The definition of the  $1\sigma$  credible interval is that we have 68% belief that  
 1200 the parameter is within those bounds. For a more generalised definition, the credible  
 1201 interval is the region,  $R$ , of the posterior distribution that contains a specific fraction of  
 1202 the total probability, such that

$$\int_R P(\theta|D)d\theta = \alpha \quad (3.8)$$

1203 Where  $\theta$  is the parameter on which we calculate the credible interval. This technique  
1204 then calculates the  $\alpha \times 100\%$  credible interval.

1205 In practice, this analysis uses the highest posterior density (HPD) credible intervals  
1206 which are calculated through the following method. First, the probability distribution  
1207 is area-normalised such that it has an integrated area equal to 1.0. The bins of proba-  
1208 bility are then summed from the highest to lowest until the sum exceeds the  $1\sigma$  level  
1209 (0.68 in this example). This process is repeated for a range of credible intervals, notably  
1210 the  $1\sigma$ ,  $2\sigma$  and  $3\sigma$  along with other levels where the critical values for each level can  
1211 be found in [137]. This process can be repeated for the two-dimensional probability  
1212 distributions by creating two-dimensional contours of credible intervals rather than a  
1213 one-dimensional result.

### 1214 3.3.3 Bayesian Model Comparisons

1215 Due to the matter resonance, this analysis has some sensitivity to the mass hierarchy  
1216 of neutrino states (whether  $\Delta m_{23}^2$  is positive or negative) and the octant of  $\sin^2(\theta_{23})$   
1217 . The Bayesian approach utilised within this analysis gives an intuitive method of  
1218 model comparison by determining which hypothesis is most favourable. Taking the  
1219 ratio of Equation 3.3 for the two hypotheses of normal hierarchy,  $NH$ , and inverted  
1220 hierarchy,  $IH$ , gives

$$\frac{P(\vec{\theta}_{NH}|D)}{P(\vec{\theta}_{IH}|D)} = \frac{P(D|\vec{\theta}_{NH})}{P(D|\vec{\theta}_{IH})} \times \frac{P(\vec{\theta}_{NH})}{P(\vec{\theta}_{IH})}. \quad (3.9)$$

1221 The middle term defines the Bayes factor which is a data-driven interpretation of  
 1222 how strong the data prefers one hierarchy to the other. For this analysis, equal priors  
 1223 on both mass hierarchy hypotheses are chosen ( $P(\vec{\theta}_{NH}) = P(\vec{\theta}_{IH}) = 0.5$ ). In practice,  
 1224 the MCMC chain proposes a value of  $|\Delta m_{23}^2|$  and then applies a 50% probability  
 1225 that the value is sign flipped. Consequently, the Bayes factor can be calculated from  
 1226 the ratio of the probability density in either hypothesis. This equates to counting the  
 1227 number of steps taken in the normal and inverted hierarchies and taking the ratio. The  
 1228 same approach can be taken to compare the upper octant (UO) compared to the lower  
 1229 octant (LO) hypothesis of  $\sin^2(\theta_{23})$ .

1230 Whilst the value of the Bayes factor should always be shown, the Jeffreys scale [138]  
 1231 (highlighted in Table 3.1) gives an indication of the strength of preference for one model  
 1232 compared to the other. Other interpretations of the strength of preference of a model  
 1233 exist, e.g. the Kass and Raferty Scale [139].

$\log_{10}(B_{AB})$	$B_{AB}$	Strength of Preference
< 0.0	< 1	No preference for hypothesis A (Supports hypothesis B)
0.0 – 0.5	1.0 – 3.16	Preference for hypothesis A is weak
0.5 – 1.0	3.16 – 10.0	Preference for hypothesis A is substantial
1.0 – 1.5	10.0 – 31.6	Preference for hypothesis A is strong
1.5 – 2.0	31.6 – 100.0	Preference for hypothesis A is very strong
> 2.0	> 100.0	Decisive preference for hypothesis A

**Table 3.1:** Jeffreys scale for strength of preference for two models  $A$  and  $B$  as a function of the calculated Bayes factor ( $B_{AB} = B(A/B)$ ) between the two models [138]. The original scale is given in terms of  $\log_{10}(B(A/B))$  but converted to linear scale for easy comparison throughout this thesis.

### 1234 3.3.4 Comparison of MCMC Output to Expectation

1235 ~~Whilst not important for the extraction of oscillation parameters, understanding~~  
1236 ~~how the data constrains the model parameters is important to the understanding~~  
1237 ~~of this analysis. To ensure the fit is performing well, a best-fit spectra is produced~~  
1238 ~~using the posterior probability distribution and compared with the data, allowing~~  
1239 ~~easy by-eye comparisons to be made.~~ A simple method of doing this is to perform a  
1240 comparison in the fitting parameters (For instance, the reconstructed neutrino energy  
1241 and lepton direction for T2K far detector beam samples) of the spectra generated by  
1242 the MCMC chain to ‘data’. This ‘data’ could be true data or some variation of Monte  
1243 Carlo prediction. This allows easy comparison of the MCMC probability distribution  
1244 to the data. To perform this,  $N$  steps from the post burn-in MCMC chain are randomly  
1245 selected (Where for all plots of this style in this thesis,  $N = 3000$ ). From these, the  
1246 Monte Carlo prediction at each step is generated by reweighting the model parameters  
1247 to the values specified at that step. Due to the probability density being directly  
1248 correlated with the density of steps in a certain region, parameter values close to the  
1249 best fit value are most likely to be selected.

1250 In practice, for each bin of the fitting parameters has a probability distribution  
1251 of event rates, with one entry per sampled MCMC step. This distribution is binned  
1252 where the bin with the highest probability is selected as the mean and an error on  
1253 the width of this probability distribution is calculated using the approach highlighted  
1254 in subsection 3.3.2. Consequently, the best fit distribution in the fit parameter is not  
1255 necessarily that which would be attained by reweighting the Monte Carlo prediction  
1256 to the most probable parameter values.

1257 A similar study can be performed to illustrate the freedom of the model parameter  
1258 space prior to the fit. This can be done by throwing parameter values from the prior

<sub>1259</sub> uncertainty of each parameter. This becomes troublesome for parameters with no  
<sub>1260</sub> prior uncertainty as the range is technically infinite. Where applicable solutions to  
<sub>1261</sub> remove these have been addressed.

<sub>1262</sub> **Chapter 4**

<sub>1263</sub> **Simulation, Reconstruction and Event Se-**  
<sub>1264</sub> **lections**

<sub>1265</sub> **4.1 Simulation**

<sub>1266</sub> In order to generate a Monte Carlo prediction of the expected event rate at the far  
<sub>1267</sub> detector for both sets of samples, all the processes in the beamline, atmospheric flux,  
<sub>1268</sub> neutrino interaction, and detector need to be modeled. The beamline simulation  
<sub>1269</sub> consists of three distinct parts; initial hadron interaction modeling, target station  
<sub>1270</sub> geometry and particle tracking and hadronic re-interactions. These are modeled by  
<sub>1271</sub> FLUKA [140], JNUBEAM [141, 142], and GCALOR [143], respectively. FLUKA is  
<sub>1272</sub> not very adaptable but matches external cross-section measurements in the region of  
<sub>1273</sub> interest better than GCALOR ( $O(10)$ GeV). Thus a small simulation is built to model  
<sub>1274</sub> the interactions in the target and the output is then passed to JNUBEAM and GCALOR  
<sub>1275</sub> for propagation. The hadronic interactions are tuned to data from the NA61/SHINE  
<sub>1276</sub> [144–146] and HARP [147] experiments. The tuning is done by reweighting the FLUKA  
<sub>1277</sub> and GCALOR predictions to match the external data multiplicity and cross-section  
<sub>1278</sub> measurements, based on final state particle kinematics [148]. The predicted flux for  
<sub>1279</sub> neutrino and antineutrino beam modes is illustrated in Figure 2.7.

<sub>1280</sub> The atmospheric neutrino flux predictions are simulated by the HKKM model  
<sub>1281</sub> [43, 45], where the primary cosmic ray flux is tuned to AMS [149] and BESS [150]

external data assuming the US-standard atmosphere '76 [151] density profile and includes geomagnetic field effects. Secondary interactions of pions and muons are handled by DPMJET-III [152] for energies above 32GeV and JAM [45, 153] for energies below that value. These hadronic interactions are tuned to external data [154, 155] using the same methodology as the tuning of the beamline simulation. The energy and cosine zenith predictions of  $\nu_e, \bar{\nu}_e, \nu_\mu, \bar{\nu}_\mu$  flux are given in Figure 1.3 and Figure 1.5, respectively. The flux is approximately symmetrical and peaked around  $\cos(\theta_Z) = 0.0$ . This is because horizontally-going pions and kaons can travel further than their vertically-going counterparts resulting in a larger probability of decay to neutrinos. The symmetry is broken in low-energy neutrinos due to geomagnetic effects, which modify the track of the primary cosmic rays.

The neutrino interactions in all three detectors are simulated with NEUT [156, 157]. This simulates quasi-elastic (QE), meson exchange (MEC), single meson production (PROD), coherent pion production (COH), and deep inelastic scattering (DIS) interactions. These interaction categories can be further broken down by whether they were propagated via a  $W^\pm$  boson in Charged Current (CC) interactions or via a  $Z^0$  boson in Neutral Current (NC) interactions. CC interactions have a charged lepton in the final state, which can be flavour-tagged in reconstruction to determine the flavour of the neutrino. In contrast, NC interactions have a neutrino in the final state so no flavour information can be determined from the observables in the detector. This is the reason why NC events are assumed to not oscillate within the analysis. Both CC and NC interactions are modeled for all the above interaction categories, other than MEC interactions which are only modeled for CC events. The SK detector is only sensitive to charged particles, so all charged current interactions are simulated whilst only neutral current processes that produce charged mesons (NCDIS, NCCOH, and NCPROD) are modeled. NC MEC interactions can only produce charged particles through secondary re-interactions which is a low cross-section process.

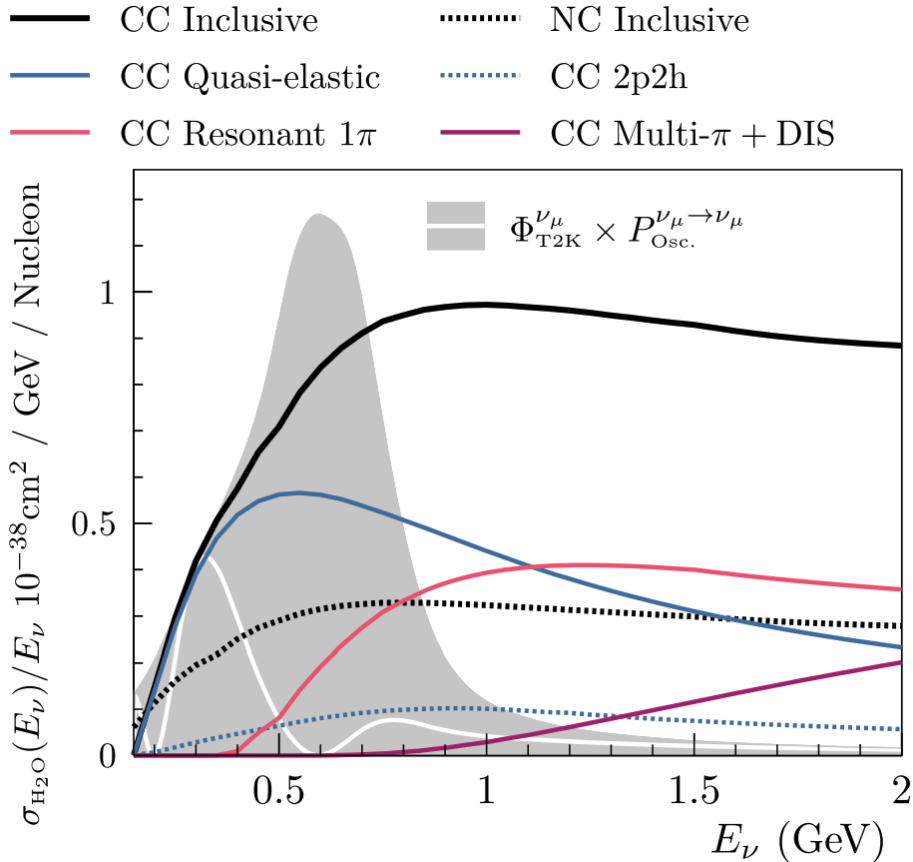


**Figure 4.1:** The NEUT prediction of the  $\nu_\mu$ -H<sub>2</sub>O cross-section overlaid on the T2K  $\nu_\mu$  flux. The charged current (black, solid) and neutral current (black, dashed) inclusive, charged current quasi-elastic (blue, solid), charged current 2p2h (blue, dashed), charged current single pion production (pink), and charged current multi- $\pi$  and DIS (Purple) cross-sections are illustrated. Taken from [156].

As illustrated in Figure 4.1, QE interactions dominate the low-energy cross-section of neutrino interactions. The NEUT implementation adopts the Llewellyn Smith [158] model for neutrino-nucleus interactions, where the nuclear ground state of any bound nucleons (neutrino-oxygen interactions) is approximated by a spectral-function [159] model that simulates the effects of Fermi momentum and Pauli blocking. The cross-section of QE interactions are controlled by vector and axial-vector form factors parameterised by the BBBA05 [160] model and a dipole form factor with  $M_A^{QE} = 1.21\text{GeV}$  fit to external data [161], respectively. QE interactions only account for single-nucleon interactions whereas multi-nucleon interactions (or MEC) can contribute significantly to the overall cross-section. NEUT implements the Valencia [162] model

1319 to simulate MEC events, where two nucleons and two holes in the nuclear target are  
1320 produced (Often called 2p2h interactions due to this effect).

1321 For neutrinos of energy  $O(1)\text{GeV}$ , PROD interactions become dominant. These  
1322 predominantly produce charged and neutral pions although  $\gamma$ , kaon, and  $\eta$  production  
1323 is also considered. To simulate these interactions, the Berger-Sehgal [163] model is  
1324 implemented within NEUT. It simulates the excitation of a nucleon from a neutrino  
1325 interaction, production of an intermediate baryon, and the consequential decay to a  
1326 single meson or  $\gamma$ . Pions can also be produced through COH interactions, which occur  
1327 when the incoming neutrino interacts with the entire oxygen nuclei target leaving a  
1328 single pion outside of the nucleus. NEUT utilises the Berger-Sehgal [164] model to  
1329 simulate these interactions.

1330 DIS and multi- $\pi$  producing interactions become the most dominant for energies  
1331  $> O(5)\text{GeV}$ . PYTHIA [165] is used to simulate any interaction with invariant mass,  
1332  $W > 2\text{GeV}/c^2$ , which produces at least one meson. For any interaction which produces  
1333 at least two mesons but has  $W < 2\text{GeV}/c^2$ , the Bronner model is invoked [166].  
1334 Both of these models use Parton distribution functions based on the Bodek-Yang  
1335 model [167–169].

1336 Any pion which is produced within the nucleus can re-interact through final state  
1337 interactions before it exits, as illustrated by the scattering, absorption, production, and  
1338 exchange interactions in Figure 4.2. These re-interactions alter the observable particles  
1339 within the detector. For instance, if the charged pion from a CC PROD interaction  
1340 is absorbed, the observables would mimic a CC QE interaction. To simulate these  
1341 effects, NEUT uses a semi-classical intranuclear cascade model [156]. This cascade  
1342 functions by stepping the pion through the nucleus in fixed-length steps equivalent  
1343 to  $dx = R_N/100$ , where  $R_N$  is the radius of the nucleus. At each step, the Monte  
1344 Carlo allows the pion to interact through scattering, charged exchange, absorption, or

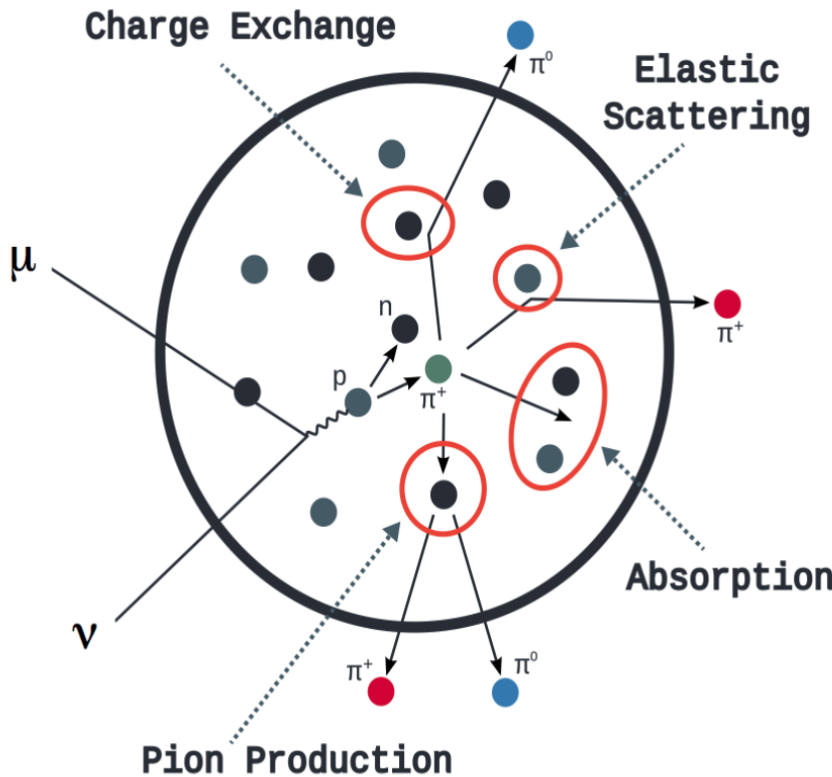


**Figure 4.2:** Illustration of the various processes which a pion can undergo before exiting the nucleus. Taken from [170].

1345 production with an interaction-dependent probability calculated from a fit to external  
 1346 data [171]. This cascade continues until the pion is absorbed or exits the nucleus.

1347 Once the outgoing particle kinematics have been determined from NEUT, they  
 1348 are passed into the detector simulation. The near detectors ND280 and INGRID are  
 1349 simulated using a GEANT4 package [116, 172] to simulate the detector geometry and  
 1350 particle tracking. The response of the detectors is simulated using the elecSim pack-  
 1351 age. The far detector simulation is based upon the original Kamiokande experiment  
 1352 software which uses the GEANT3-based SKDETSIM [116, 173] package. This controls  
 1353 the interactions of particles in the water as well as Cherenkov light production. The  
 1354 water quality and PMT calibration measurements detailed in subsection 2.1.2 are also  
 1355 used within this simulation to make accurate predictions of the detector response.

**<sup>1356</sup> 4.2 Event Reconstruction at SK**

<sup>1357</sup> Any above Cherenkov threshold event which occurs in SK will be recorded by the  
<sup>1358</sup> PMT array, where each PMT records the time and accumulated charge is measured.  
<sup>1359</sup> This is shown in the event displays illustrated in Figure 4.3. To be useful for physics  
<sup>1360</sup> analyses, this series of PMT hit information needs to be reconstructed to determine the  
<sup>1361</sup> particle’s identity and kinematics. This is because the charge and timing distribution  
<sup>1362</sup> of photons generated by a particular particle in an event is dependent upon its initial  
<sup>1363</sup> vertex position, time, direction, and momentum of the particle.

<sup>1364</sup> For the purposes of this analysis, the `fitQun` reconstruction algorithm is utilised.  
<sup>1365</sup> Its core function is to compare a prediction of the accumulated charge and timing  
<sup>1366</sup> distribution from each PMT, generated for a particular particle hypothesis, to that  
<sup>1367</sup> observed in the neutrino event. It determines the best particle hypothesis by min-  
<sup>1368</sup> imising a likelihood function which includes information from PMTs which were hit  
<sup>1369</sup> and those that were not hit. This improves upon the `APFit` reconstruction algorithm  
<sup>1370</sup> which has been used for many previous SK analyses. `APFit` only includes information  
<sup>1371</sup> from PMTs within the 43 deg Cherenkov cone and then sequentially fits the kinematic  
<sup>1372</sup> parameters and particle configuration. Conversely, `fitQun` performs a simultaneous  
<sup>1373</sup> fit, improving both the accuracy of the fit parameters and the rejection of neutral  
<sup>1374</sup> current  $\pi^0$  events [174, 175]. The `fitQun` algorithm is based on the key concepts  
<sup>1375</sup> on the MiniBooNE reconstruction algorithm [176] and is described in [177] which is  
<sup>1376</sup> summarised below.

<sup>1377</sup> An event in SK can consist of multiple “sub-events”. For example, a muon neutrino  
<sup>1378</sup> interaction will generate a muon which will subsequently decay into an electron.  
<sup>1379</sup> Both the muon and electron can generate Cherenkov photons but both subevents  
<sup>1380</sup> need to be reconstructed separately. Therefore, to avoid assigning photons generated

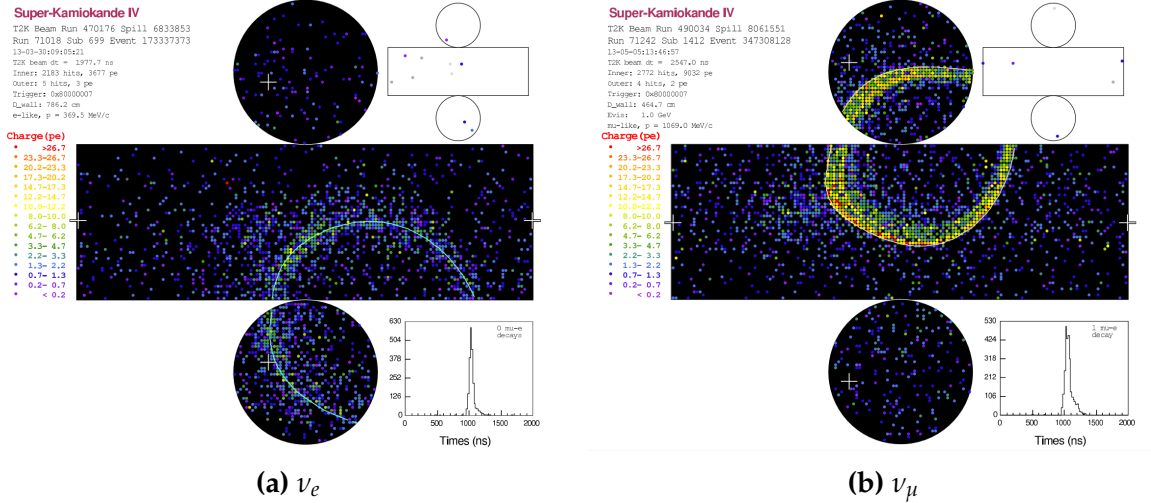


**Figure 4.3:** Event displays from Super Kamiokande illustrating the “crisp” ring from a muon and the typically “fuzzy” electron ring. Each pixel represents a PMT and the color scheme denotes the accumulated charge deposited on that PMT. Figures taken from [178].

1381 by the decay-electron to the muon, each event is divided into time clusters, termed  
 1382 “subevents”, where subevent is defined to contain at most one hit for each PMT. To  
 1383 find the subevents, a vertex goodness metric is calculated for some vertex position  $\vec{x}$   
 1384 and time  $t$ ,

$$G(\vec{x}, t) = \sum_i^{\text{hit PMTs}} \exp \left( -\frac{1}{2} \left( \frac{T_{Res}^i(\vec{x}, t)}{\sigma} \right)^2 \right) \quad (4.1)$$

1385 where

$$T_{Res}^i(\vec{x}, t) = t_i - t - |R_{PMT}^i - \vec{x}| / c_n \quad (4.2)$$

1386 is the residual hit time,  $R_{PMT}^i$  is the position of the  $i^{th}$  PMT,  $c_n$  is the speed of light in  
 1387 water and  $\sigma = 4\text{ns}$  which is comparable to the time resolution of the PMT. When the fit

values of time and vertex are close to the true values,  $T_{Res}^i(\vec{x}, t)$  tends to zero resulting in subevents appearing as spikes in the goodness metric. The fit vertex and time are grid-scanned, and the values which maximise the goodness metric are selected as the “pre-fit vertex”. Whilst this predicts a vertex for use in the clustering algorithm, the final vertex is fit using the higher-precision maximum likelihood method described below.

Once the pre-fit vertex has been determined, the goodness metric is scanned as a function of  $t$  to determine the number of delayed peaks. A peak-finding algorithm is then used on the goodness metric, requiring the goodness metric to exceed some threshold and drop below a reduced threshold before any delayed additional peaks are considered. The thresholds are set such that the rate of false peak finding is minimised while still attaining good data to Monte Carlo agreement. To improve performance, the pre-fit vertex for each delayed subevent is re-calculated after PMT hits from the primary subevent are masked. This improves the decay-electron tagging performance. Once all subevents have been determined, the time window around each subevent is then defined by the earliest and latest time which satisfies  $-180 < T_{Res}^i < 800\text{ns}$ . The subevents and associated time windows are then used as seeds for further reconstruction.

For a given subevent, `fiTQun` constructs a likelihood based on the accumulated charge  $q_i$  and time information  $t_i$  from the  $i^{th}$  PMT,

$$L(\Gamma, \vec{\theta}) = \prod_j^{\text{unhit}} P_j(\text{unhit}|\Gamma, \vec{\theta}) \prod_i^{\text{hit}} \{1 - P_i(\text{unhit}|\Gamma, \vec{\theta})\} f_q(q_i|\Gamma, \vec{\theta}) f_t(t_i|\Gamma, \vec{\theta}), \quad (4.3)$$

where  $\vec{\theta}$  defines the track parameters; vertex position, direction vector and momenta, and  $\Gamma$  represents the particle hypothesis.  $P_i(\text{unhit}|\Gamma, \vec{\theta})$  defines the probability

<sub>1410</sub> of the  $i^{th}$  tube to not register a hit given the track parameters and particle hypothesis.  
<sub>1411</sub> The charge likelihood,  $f_q(q_i|\Gamma, \vec{\theta})$ , and time likelihood,  $f_t(t_i|\Gamma, \vec{\theta})$ , represent the probability density function of observing charge  $q_i$  and time  $t_i$  on the  $i^{th}$  PMT given track parameters  $\vec{\theta}$  and particle hypothesis  $\Gamma$ .

<sub>1414</sub> As the generation and propagation of the optical photons are independent of the PMT and electronics response, it is natural to split the calculation into two. Firstly, calculating the expected number of photoelectrons (or predicted charge),  $\mu_i$ , at the <sub>1417</sub>  $i^{th}$  PMT, and then calculating the likelihood based on this value. This substitution allows the charge likelihood density  $f_q(q_i|\mu_i)$  and unhit probability  $P_i(\text{unhit}|\mu_i)$  to be expressed via quantities that are only dependent on the response of the PMT.

<sub>1420</sub> The predicted charge is calculated based on contributions from both the direct light and the scattered light. The direct light contribution is determined based on the integration of the Cherenkov photon profile along the track. PMT angular acceptance and water quality and calibration measurements discussed in subsection 2.1.2 are included to accurately model the detector's response. The scattered light is calculated in a similar way although it includes a scattering function that depends on the vertex of the particle and the position of the PMT. The charge likelihood is calculated by comparing the prediction to the observed charge in the PMT, where the prediction assumes photoelectron generation obeys a Poisson distribution.

<sub>1429</sub> The time likelihood is approximated to depend on the vertex  $\vec{x}$ , direction  $\vec{d}$ , and time  $t$  of the track parameters as well as the particle hypothesis. The expected time for PMT hits is calculated by assuming unscattered photons being emitted from the midpoint of the track,  $S_{mid}$ ,

$$t_i^{exp} = t + S_{mid}/c + |R_{PMT}^i - \vec{x} - S_{mid}\vec{d}|/c_n, \quad (4.4)$$

where  $c$  is the speed of light in a vacuum. The time likelihood is then expressed in terms of the residual difference between the PMT hit time and the expected hit time,  $t_i^{Res} = t_i - t_i^{exp}$ . As the first photon hit defines the PMT hit time, the time likelihood density profile is narrower for higher momenta particles which introduces a dependence on the predicted charge. The particle hypothesis and momentum also affect the Cherenkov photon distribution which modifies the shape of the time likelihood density since in reality not all photons are emitted at the midpoint of the track. As with the charge likelihood, the contributions from both the direct and scattered light to the time likelihood density are calculated separately, which are both calculated from particle gun studies.

The track parameters,  $\vec{\theta}$ , which maximise  $L(\Gamma|\vec{\theta})$  are defined the best fit parameters. In practice MINUIT [179] is used to minimise the value of  $-\ln L(\Gamma, \vec{\theta})$ . The particle hypothesis is determined by the comparison of  $L(\Gamma, \vec{\theta})$  across all viable hypotheses,  $\Gamma$ . The fit considers an electron-like, muon-like, and charged pion-like hypothesis. The particle's identity is determined by taking the ratio of the likelihood of each of the hypotheses. For instance, electrons and muons are distinguished by considering the value of  $\ln(L_e/L_\mu)$  as illustrated in Figure 4.4.

Alongside the three hypotheses which have a single final state particle generating optical photons, denoted “single-ring” particle hypotheses, the `fitQun` algorithm also considers a  $\pi^0$  hypothesis. To do this, it performs a fit looking for two standard electron-hypothesis tracks which point to the same vertex position and time. This assumes the electron tracks are generated from photon-conversion so the electron tracks actually appear offset from the proposed  $\pi^0$  vertex. For these fits, the conversion length, direction, and momenta of each photon are also considered as track parameters which are then fit in the same methodology as the standard single-ring hypotheses.

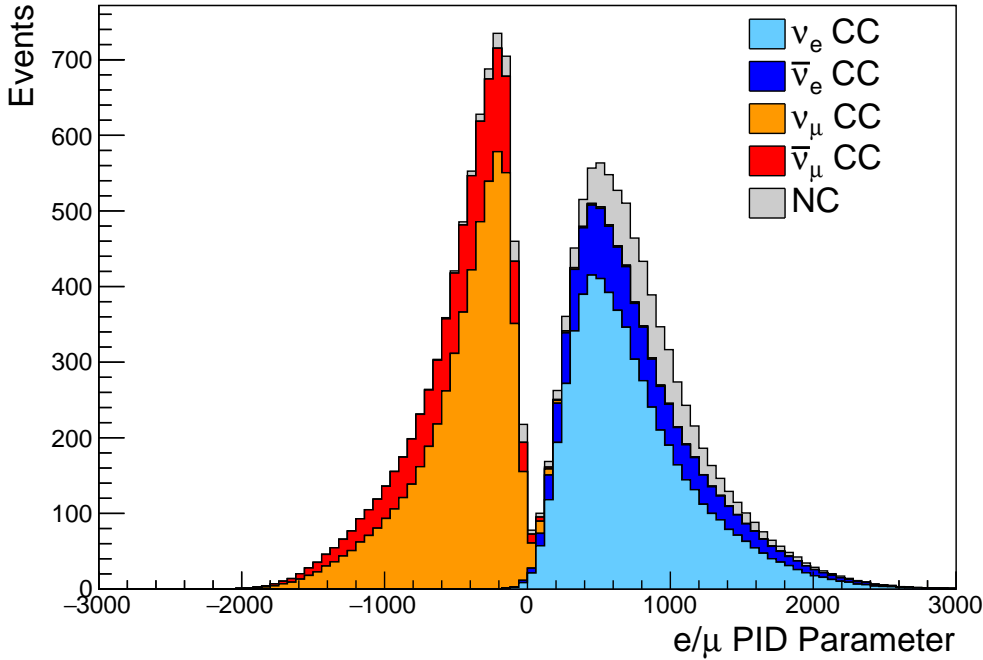


**Figure 4.4:** The electron/muon PID separation parameter for all sub-GeV single-ring events in SK-IV. The charged current (CC) component is broken down in four flavours of neutrino ( $\nu_\mu, \bar{\nu}_\mu, \nu_e$  and  $\bar{n}u_e$ ). Events with positive values of the parameter are determined to be electron-like.

The previous discussion pertains to a single final state particle that generates optical photons. However, the higher energy atmospheric neutrino events can generate final states with multiple particles which generate Cherenkov photons. These “multi-ring” hypotheses are also considered in the `fitQun` algorithm, but only for the first subevent in each ring to reduce computational cost. When calculating the charge likelihood density, the predicted charge associated with each ring is calculated separately and then merged to calculate the total accumulated charge on each PMT. Similarly, the time likelihood for the multi-ring hypothesis is calculated assuming each ring is independent. However, each track is then time-ordered based on the time of flight from the center of the track to the PMT, and the direct light from any ring incident on the PMT arrives before any scattered light. To reduce computational resources required for a fit, the multi-ring fits only consider electron-like and charged pion-like rings as the pion fit can be used as a proxy for a muon fit due to their similar mass.

1471     Typically, multi-ring fits have the largest likelihood because of the additional  
1472    degrees of freedom introduced. Multi-ring fits proceed by proposing another ring  
1473    to the previous fit and then fitting the parameters in the method described above.  
1474    The additional ring is only added if the ratio of likelihoods between the  $n$  and  $n + 1$   
1475    passes the criteria. The criteria values for single-ring and multi-ring separation have  
1476    been determined to be 9.35(11.83) based on Monte-Carlo studies, for hypotheses with  
1477    electron-like(muon-like) the first ring.

1478     As an example of how the reconstruction depends on the detector conditions, the  
1479    author of this thesis assessed the quality of event reconstruction for SK-V data. The  
1480    detector systematics invoked within the T2K-only oscillation analysis are determined  
1481    using data to Monte Carlo comparisons using the SK-IV data [180]. Due to tank-open  
1482    maintenance occurring between SK-IV and SK-V, the dark rate of each PMT was  
1483    observed to increase due to light exposure for a significant time during the repairs.  
1484    This can be seen in Figure 4.5. Run-10 of the T2K experiment was conducted in the SK-  
1485    V period, so the consistency of SK-IV and SK-V data needs to be studied to determine  
1486    whether the SK-IV defined systematics can be applied to the run-10 data. This study  
1487    was performed using the stopping muon data set for both the SK-IV and SK-V periods.  
1488    This data is used due to the high rate of interactions,  $O(200)$  events per hour, as well  
1489    as having similar energies to muons from CCQE  $\nu_\mu$  interactions. The rate of cosmic  
1490    muons does depend on the solar activity cycle [181]. This has been neglected in this  
1491    comparison study as it is the shape of the distributions which is important for the  
1492    purposes of being compared to the detector systematics. 2398.42 and 626.719 hours of  
1493    SK-IV and SK-V are used which equates to 686743 and 192504 events respectively.

1494     The predicted charge used in the `fitQun` charge likelihood calculation for each  
1495    PMT includes the photoelectron emission contribution from the dark rate of the PMT.  
1496    Therefore, the increase in the dark rate needs to be accounted for. In practice, the

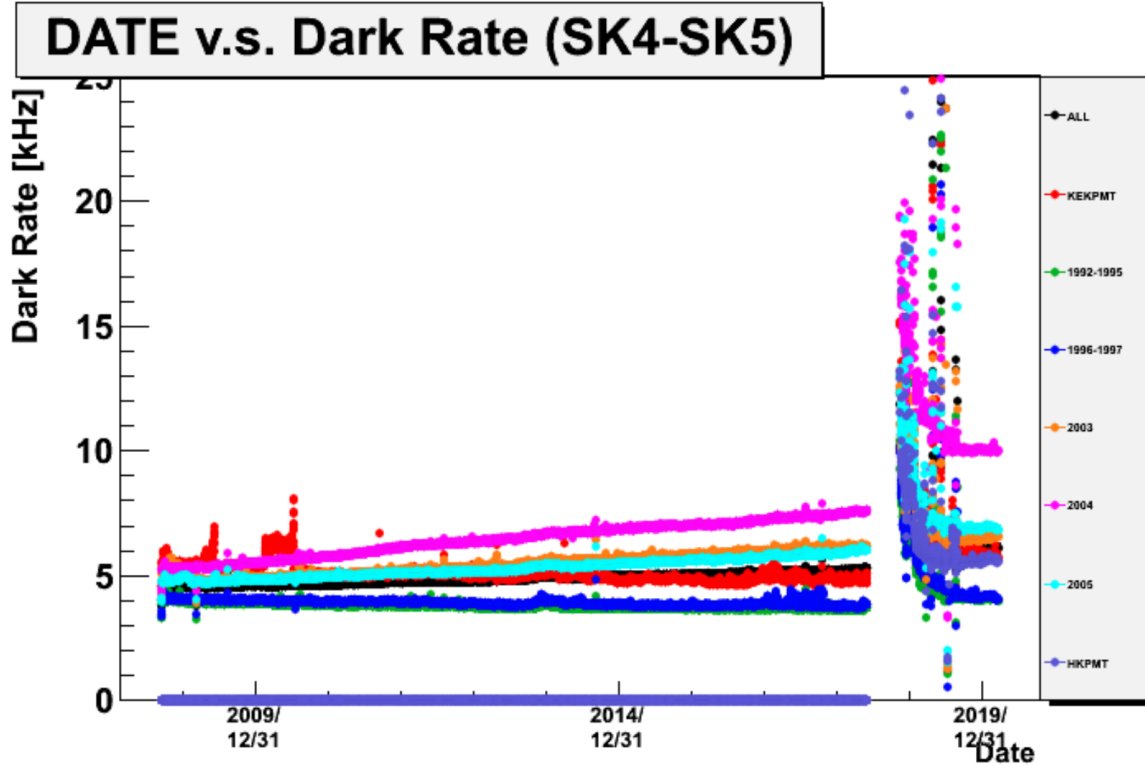


**Figure 4.5:** The variation of the measured dark rate as a function of date, broken down by PMT type. The SK-IV and SK-V periods span September 2008 to May 2018 and January 2019 to July 2020 respectively. The break in measurement between 2018 corresponds to the period of tank repair and refurbishment. Figure adapted from [180].

reconstruction algorithm takes the average dark rate for all PMTs for each SK period as an input and predicts the associated charge from this contribution. The dark rate was calculated by averaging the dark rate per run for each period separately, using the calibration measurements detailed in subsection 2.1.2. The average dark rate from SK-IV and SK-V were found to be  $4.57\text{kHz}$  and  $6.30\text{kHz}$ , respectively. The associated charge with the muon and decay electron subevents are illustrated in Figure 4.6. As expected, the increase in dark rate is not observed in the muon subevent which is of typically higher energy. However, it has a clear effect on the decay electron subevent which is lower energy.

The energy scale systematic for the SK-IV period was determined to be 2.1% [182]. It is defined to be equal to the difference between data and Monte Carlo prediction

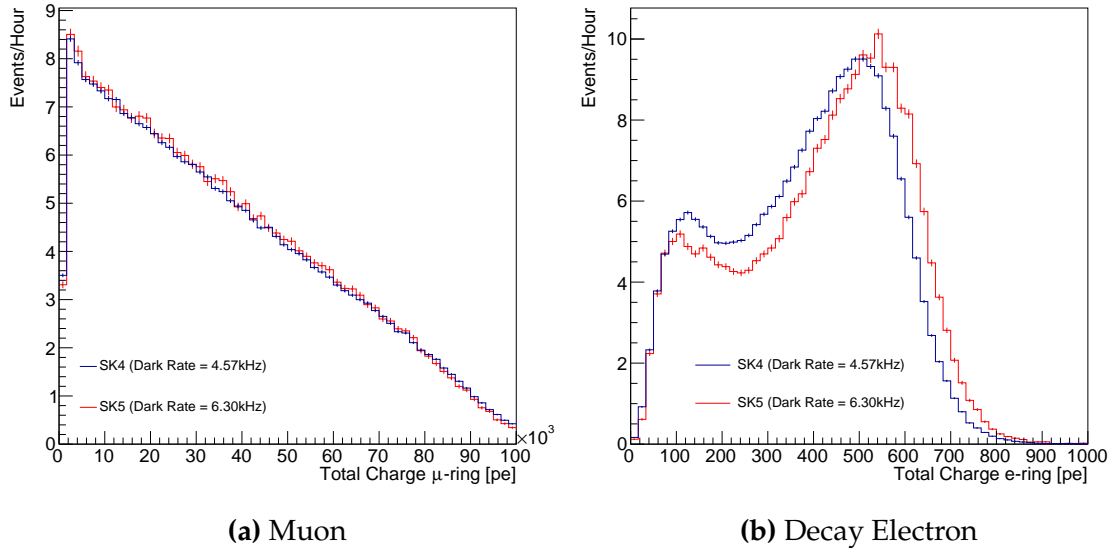


**Figure 4.6:** Comparison of the measured raw charge deposited per event from the stopping muon data samples between SK-IV (Blue) and SK-V (Red), split by the primary muon subevent and the associated decay electron subevent.

in the stopping muon data sample. To determine the consistency of the SK-IV and SK-V with respect to the energy scale systematic, the muon momentum distribution is compared between the two SK periods. The distribution of Cherenkov photons is dependent upon the momentum of the particle. This is then integrated along the track length of the particle to determine the PMT hit probability for each PMT. Consequently, the reconstructed momentum divided by track length is compared between SK-IV and SK-V as illustrated in Figure 4.7.

The consistency between these distributions has been computed in two ways.  
Firstly, a Gaussian is fit to each distribution separately. The mean of which is found to  
be  $(2.272 \pm 0.003)\text{MeV/cm}$  and  $(2.267 \pm 0.006)\text{MeV/cm}$  for SK-IV and SK-V respec-  
tively. The ratio of these is equal to  $1.002 \pm 0.003$ . The mean of the Gaussian's is  
consistent with the expected stopping power of a minimum ionising muon for a target  
material (water) with  $Z/A \sim 0.5$  [183]. The second consistency check is performed  
by introducing a nuisance parameter,  $\alpha$ , which modifies the SK-V distribution. The  
value of  $\alpha$  which minimises the  $\chi^2$  between the SK-IV and SK-V is determined by

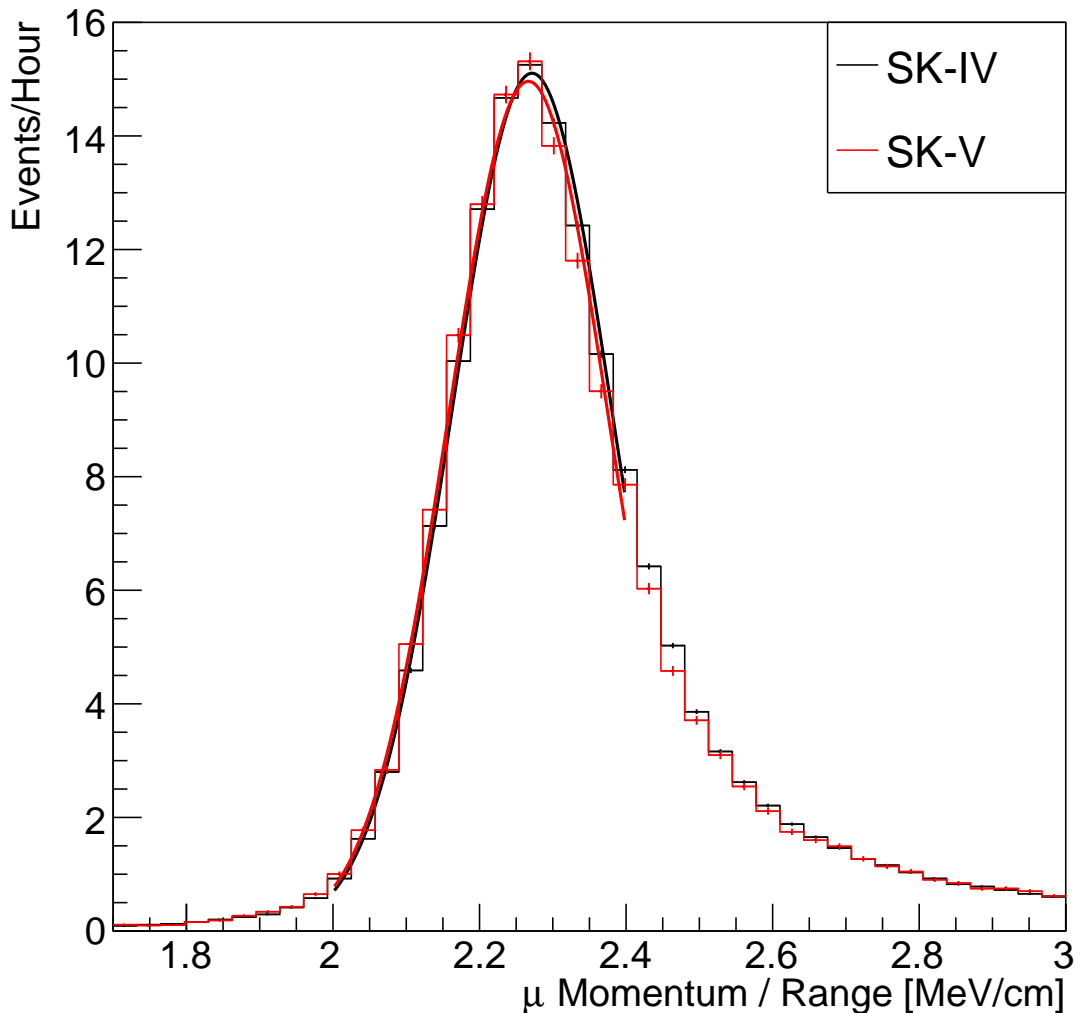


**Figure 4.7:** The distribution of the reconstructed momentum from the muon ring divided by the distance between the reconstructed muon and decay electron vertices as found in the stopping muon data sets of SK-IV (Black) and SK-IV (Red). Only events with one tagged decay electron and considered. A Gaussian fit is considered in the range [2.0, 2.4] MeV/cm and illustrated as the solid curve.

scanning across a range of values. This is repeated by applying  $\alpha$  as a multiplicative factor and an additive shift. The  $\chi^2$  distributions for different values of  $\alpha$  is illustrated in Figure 4.8. The values which minimise the  $\chi^2$  are found to be 0.0052 and 1.0024 for the additive and multiplicative implementations respectively. No evidence of shifts larger than the 2.1% uncertainty on the energy scale systematic has been found in the reconstructed momentum distribution of SK-IV and SK-V.

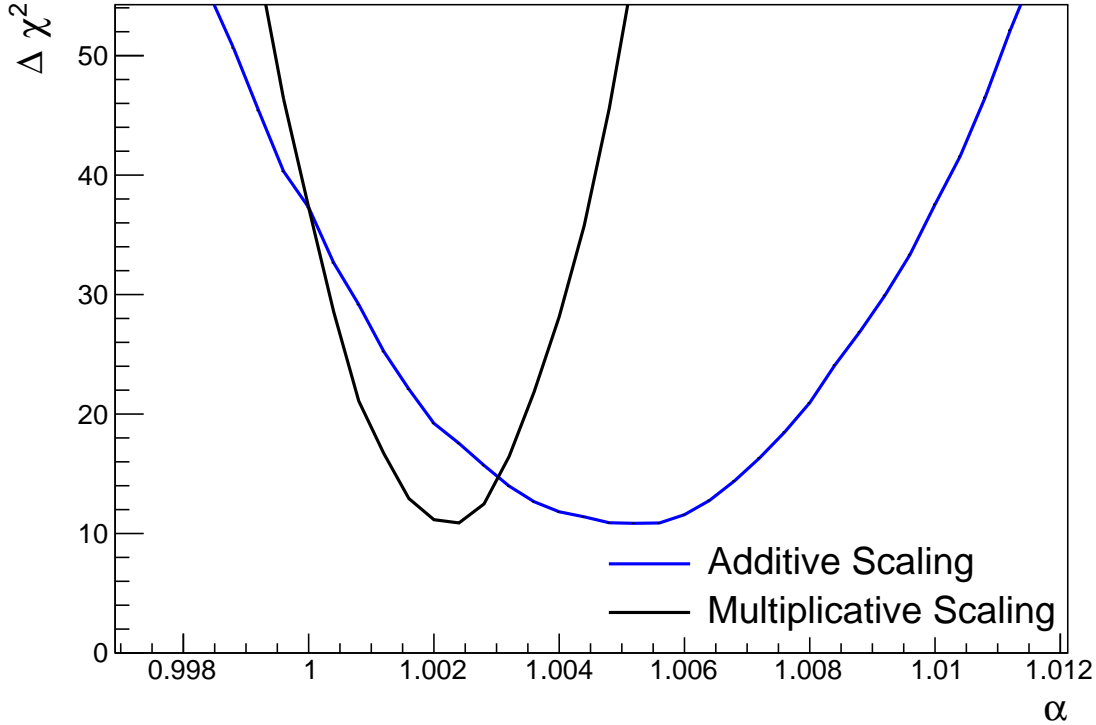


**Figure 4.8:** The  $\chi^2$  difference between the SK-IV and SK-V reconstructed muon momentum divided by range when the SK-V is modified by the scaling parameter  $\alpha$ . Both additive (Blue) and multiplicative (Black) scaling factors have been considered. In practice, the additive scaling factor actually uses the value of  $(\alpha - 1.0)$ .

### <sup>1529</sup> 4.3 Event Selection at SK

<sup>1530</sup> Atmospheric neutrino events observed in the SK detector are categorised into three  
<sup>1531</sup> different types of samples; fully contained (FC), partially contained (PC) and up-  
<sup>1532</sup> going muon (Up- $\mu$ ), using signatures in the inner and outer detector (ID and OD,  
<sup>1533</sup> respectively). To identify FC neutrino events, it is required that the neutrino interacts  
<sup>1534</sup> inside the fiducial volume of the ID such that no significant OD activity is observed.  
<sup>1535</sup> For this analysis, an event is defined to be in the fiducial volume providing the  
<sup>1536</sup> event vertex is at least 0.5m away from the ID walls. PC events have the same ID  
<sup>1537</sup> requirements but can have a larger signal present inside the OD. Typically these events  
<sup>1538</sup> are higher energy muon interactions that penetrate the ID walls. The Up- $\mu$  sample

1539 contains events where muons are created in the OD water or rock below the tank  
1540 and then propagate upwards through the detector. The reason downward-going  
1541 muons generated from neutrino interactions above the tank are neglected is due to  
1542 the difficulty in separating their signature from the cosmic muon shower background.  
1543 The sample categories are visually depicted in Figure 4.9.

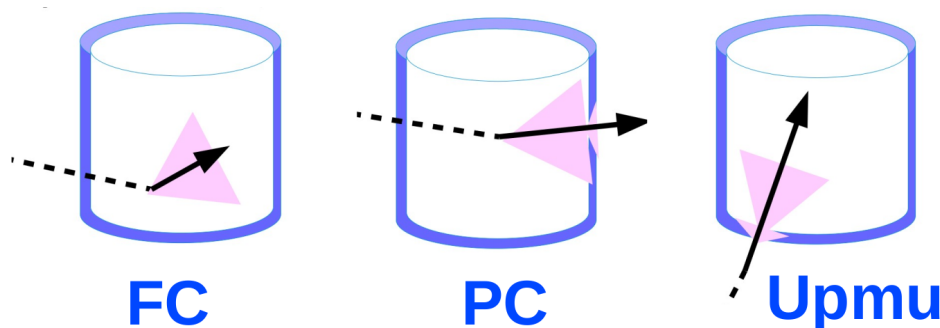


**Figure 4.9:** A depiction of the topology patterns for fully-contained (FC), partially-contained (PC) and up-going muon ( $\text{Up-}\mu$ ) samples included in this analysis.

1544 Based on the event characteristics as defined by the `fitQun` event reconstruction  
1545 software, the FC events are further divided up by

- 1546 • **Visible Energy:** equal to the sum of the reconstructed kinetic energy above the  
1547 Cerenkov threshold for all rings present in the event. The purpose is to separate  
1548 events into sub-GeV and multi-GeV categories.
- 1549 • **Number of observed Cerenkov rings.** The purpose is to separate single-ring and  
1550 multi-ring events, where single-ring events predominantly consist of quasi-elastic  
1551 interactions and multi-ring events are resonant pion production or deep inelastic  
1552 scattering events.
- 1553 • **Particle identification parameter of the most energetic ring:** A value deter-  
1554 mined from the maximum likelihood value based on `fitQun`'s electron, muon, or  
1555 pion hypothesis. The purpose is to separate electron-like and muon-like events.

- **Number of sub-events:** Based on optimised time cuts, this quantity determines the number of observed decay electrons associated with an event. The main purpose is to separate quasi-elastic events (which have one decay electron emitted from the muon decay) and resonant pion production events (which have two decay electrons emitted from the muon and pion).

The PC and Up- $\mu$  categories are broken down into “through-going” and “stopping” samples depending on whether the muon left the detector. This is because the stopping events deposited the entire energy of the interaction into the detector, resulting in better reconstruction. Through-going Up- $\mu$  samples are further broken down by whether any hadronic showering was observed in the event which would be mostly likely due to DIS interactions. The expected neutrino energy for the different categories is given in Figure 4.10. FC sub-GeV and multi-GeV events peak around 0.7GeV and 3GeV respectively, with slightly different peak energies for  $\nu_x \rightarrow \nu_e$  and  $\nu_x \rightarrow \nu_\mu$ . PC and Up- $\mu$  are almost entirely comprised of  $\nu_x \rightarrow \nu_\mu$  events and peak around 7GeV and 100GeV respectively.

In data-taking operation, the SK detector observes many background events alongside the beam and atmospheric neutrino signal events of physics interest. Cosmic ray muons and flasher events, which is the spontaneous discharge of a given PMTm contribute the largest amount of background events in the energy range relevant to oscillation analyses. Lower energy analyses like DSNB searches are also subject to radioactive backgrounds [184]. Therefore the data recorded is reduced with the aim of removing these background events. The reduction process is detailed in [47, 88] and briefly summarised below.

The first two steps in the FC reconstruction remove most cosmic ray muons by requiring a significant amount of ID activity compared to that measured in the OD. This is done by counting the total number of photoelectrons recorded in the ID as

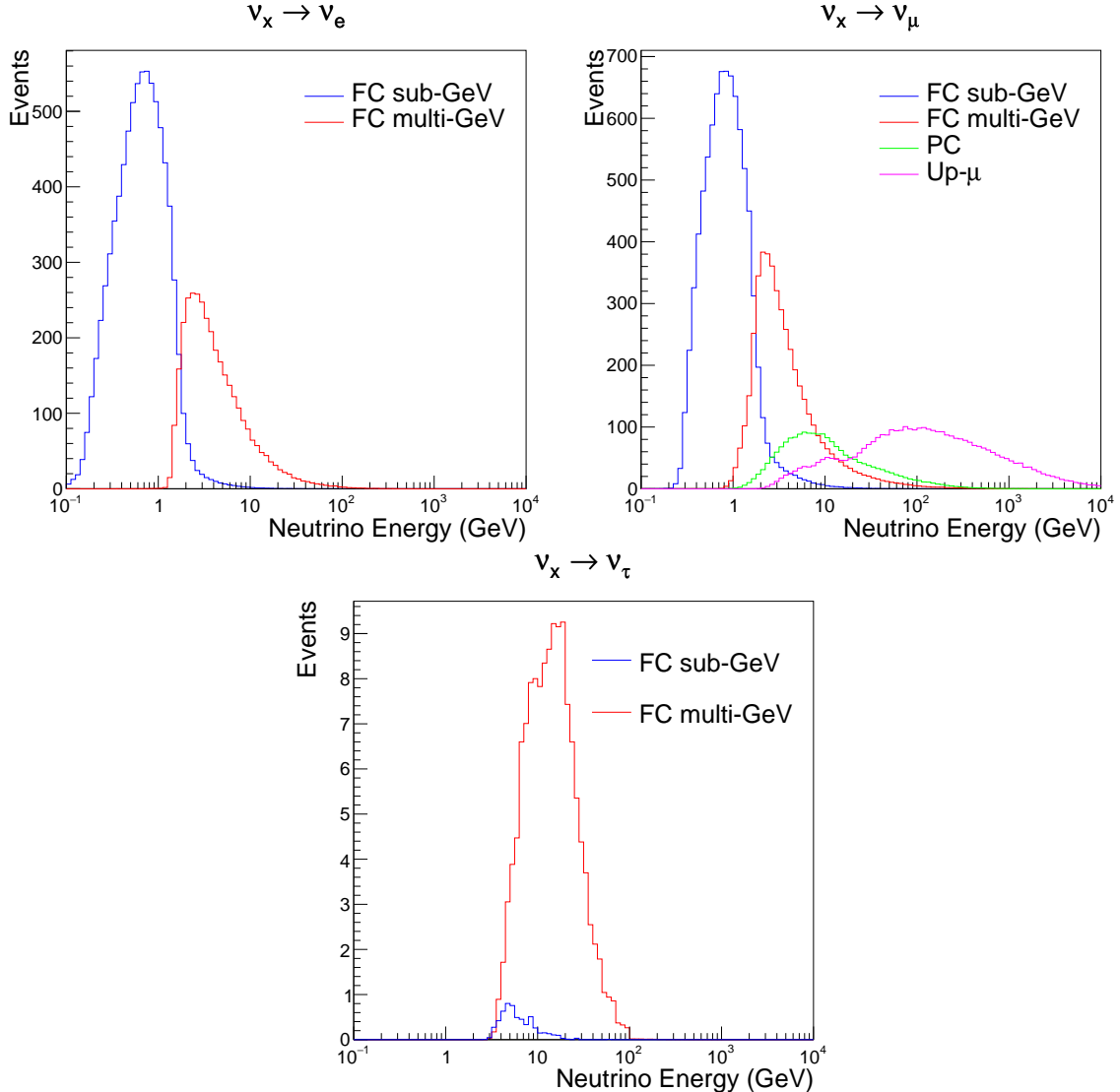


**Figure 4.10:** The predicted neutrino flux of the fully contained (FC) sub-GeV and multi-GeV, partially contained (PC) and upward-going muon (Up- $\mu$ ) events. The prediction is broken down by the  $\nu_x \rightarrow \nu_e$  prediction (top left),  $\nu_x \rightarrow \nu_\mu$  prediction (top right) and  $\nu_x \rightarrow \nu_\tau$  prediction (bottom). All systematic dials are set to their nominal values and the Asimov A oscillation parameters are assumed.

well as the number of hits in the OD. A third reduction step is then applied to select cosmic-ray muons that pass the initial reduction. These are typically high momentum muons or events which leave only a small number of hits in the OD. A purpose-built cosmic muon fitter is used to determine the entrance (or exit) position of the muon from the OD and a cut is applied to OD activity contained within 8m of this position. Flasher events are removed in the fourth reduction step which is based on the close

proximity of PMT hits surrounding the PMT producing the flash. Events that pass the reduction stage to this point are reconstructed using the more accurate APFit algorithm and the fifth step of the reduction uses the information from this more accurate fitter to repeat the third and fourth reduction steps using tighter cuts. This particularly targets invisible muons which are below the Cherenkov threshold resulting in no OD activity but whose decay electrons generate light inside the ID. The final cuts require the event vertex to be within the fiducial volume (0.5m from the wall although the nominal distance is 2.0m), visible energy  $E_{vis} > 30\text{MeV}$  and fewer than 16 hits within the higher energy OD cluster. The culmination of the fully contained reduction results in 8.09 events/day in the nominal fiducial volume [185]. The uncertainty in the reconstruction is calculated by comparing Monte Carlo prediction to data. The largest discrepancy is found to be 1.3% in the fourth reduction step.

The PC and Up- $\mu$  events are also processed through their own reduction processes detailed in [47]. Both of these samples are reconstructed with the APFit algorithm rather than `fiTQun`. This is because the efficiency of reconstructing events that leave the detector has not been sufficiently studied for reliable systematic uncertainties. 0.66 and 1.44 events/day are found after the final step of reduction for the PC and Up- $\mu$  samples respectively.

<sub>1606</sub> **Chapter 5**

<sub>1607</sub> **Oscillation Probability Calculation**

<sub>1608</sub> The calculation of the oscillation probability is crucial to the reliability of the sensitivity  
<sub>1609</sub> measurements of the analysis presented within this thesis. Firstly, it is important to  
<sub>1610</sub> understand how and where the sensitivity to the oscillation parameters comes from  
<sub>1611</sub> for both atmospheric and beam samples. An overview of how these sets of samples  
<sub>1612</sub> observe changes in  $\delta_{CP}$ ,  $\Delta m_{23}^2$ , and  $\sin^2(\theta_{23})$  as well as how the atmospheric samples  
<sub>1613</sub> have an increased sensitivity to mass hierarchy determination is given in section 5.1.  
<sub>1614</sub> It also explains the additional complexities involved when including atmospheric  
<sub>1615</sub> neutrinos as compared to a beam-only analysis.

<sub>1616</sub> Without additional techniques, atmospheric sub-GeV upward-going neutrinos can  
<sub>1617</sub> artificially inflate the sensitivity to  $\delta_{CP}$  due to the quickly varying oscillation probabil-  
<sub>1618</sub> ity in this region. Therefore, a “sub-sampling” approach has been developed to reduce  
<sub>1619</sub> these biases ensuring accurate and reliable sensitivity measurements. This technique  
<sub>1620</sub> ensures that small-scale unresolvable features of the oscillation probability have been  
<sub>1621</sub> averaged over whilst the large-scale resolvable features in the oscillation probability  
<sub>1622</sub> have been kept. The documentation of this technique is found in section 5.2 alongside  
<sub>1623</sub> the validation of the choices which have been made. The CUDAProb3 implementation  
<sub>1624</sub> choice made within the fitting framework, as detailed in section 5.3, ensures that the  
<sub>1625</sub> analysis can be done in a timely manner.

<sub>1626</sub> Whilst the beam neutrinos are assumed to propagate through a constant density  
<sub>1627</sub> slab of material, the density variations through the Earth result in more complex  
<sub>1628</sub> oscillation patterns Furthermore, the uncertainty in the electron density can modify

1629 the oscillation probability for the denser core layers of the Earth. section 5.4 details  
1630 the model of the Earth used within this analysis. This includes the official SK-only  
1631 methodology as well as relatively straightforward improvements that can be made to  
1632 more closely approximate the PREM model. Another quirk of atmospheric neutrinos  
1633 oscillation studies is that the height of production in the atmosphere is not known  
1634 on an event-by-event analysis. An analytical averaging technique that approximates  
1635 the uncertainty of the oscillation probability has been followed, with the author of  
1636 this thesis being responsible for the implementation and validation. This technique is  
1637 illustrated in section 5.5 alongside the variation in oscillation probability which would  
1638 be an expected effect in the down-going and horizontal-going neutrinos.

## 1639 5.1 Overview

1640 The analysis presented within this thesis focuses on the determination of oscillation  
1641 parameters from atmospheric and beam neutrinos. Whilst subject to the same oscil-  
1642 lation probability, the way in which the two sets of samples have sensitivity to the  
1643 different oscillation parameters differs quite significantly.

1644 Atmospheric neutrinos have a varying baseline, or “path length”, such that the  
1645 distance each neutrino travels before interacting is dependent upon the zenith angle.  
1646 Therefore the oscillation probability can be represented as a two-dimensional “oscillo-  
1647 gram” as shown in Figure 5.1. For this calculation, four layers of fixed density were  
1648 used to model the Earth with values taken from an approximation of the PREM model.  
1649 These can be seen in the distinct discontinuities in the oscillogram as a function of the  
1650 zenith angle.

1651 Another complexity of atmospheric neutrino oscillation probability calculation is  
1652 the uncertainty in the height at which a neutrino was produced, termed the “produc-

tion height". Primary cosmic rays, which contribute most of the neutrino flux, can interact anywhere between the Earth's surface and  $\sim 50$ km above that. The baseline,  $L$ , for a neutrino generated with zenith angle,  $\theta$ , and production height,  $h$ , can be calculated as

$$L = \sqrt{(R_E + h)^2 - R_E^2 (1 - \cos^2(\theta))} - R_E \cos(\theta), \quad (5.1)$$

where  $R_E = 6,371$ km is the Earth's radius.

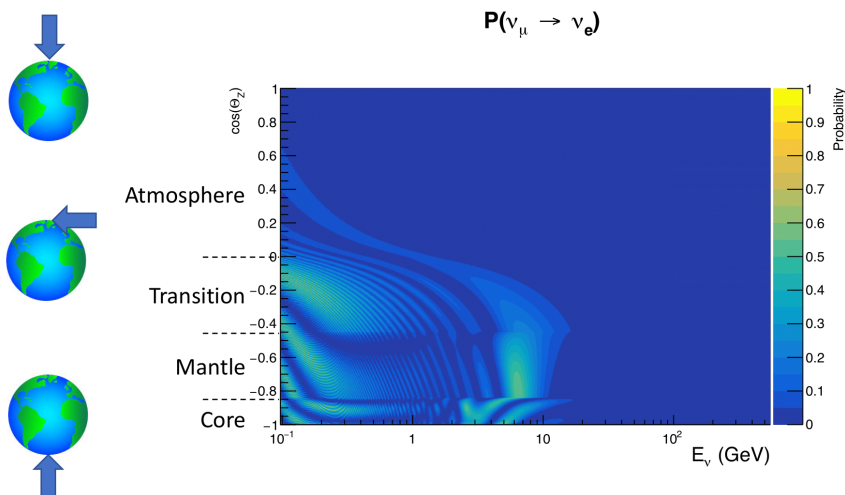


**Figure 5.1:** An "Oscillogram" that depicts the  $P(\nu_\mu \rightarrow \nu_e)$  oscillation probability as a function of neutrino energy and cosine of the zenith angle. The zenith angle is defined such that  $\cos(\theta_Z) = 1.0$  represents neutrinos that travel from directly above the detector. The four-layer constant density PREM model approximation is used and Asimov A oscillation parameters are assumed.

Atmospheric neutrinos do have some sensitivity to  $\delta_{CP}$  through a normalisation term. Figure 5.2 illustrates the difference in oscillation probability between CP-conserving and CP-violating  $\delta_{CP}$  values. The result is a complicated oscillation pattern in the appearance probability for sub-GeV upgoing neutrinos. The detector does not have sufficient resolution to resolve these individual patterns so the sensi-

tivity to  $\delta_{CP}$  for atmospheric neutrinos comes via the overall normalisation of the  
 sub-GeV upgoing events. The presence of matter means that the effect  $\delta_{CP}$  has on  
 the oscillation probability is not equal between neutrinos and antineutrinos which  
 would be expected when propagating through a vacuum. This is further extenuated  
 by the fact that SK can not distinguish neutrinos and antineutrinos well and that the  
 cross-section neutrino interaction is larger than that for antineutrinos. Finally, sample  
 selections (discussed in [DB: Link to selection chapter](#)) targeting different neutrino  
 interaction modes (charge current quasi-elastic and single pion production) result in  
 an imbalance in the percentage of neutrinos to anti-neutrinos in these samples due  
 to pion capture. Negatively charged pions from antineutrino interactions are more  
 likely to be captured by a nucleus compared to a positively charged pion emitted from  
 a neutrino interaction. This all culminates in atmospheric neutrinos having a very  
 complex sensitivity to  $\delta_{CP}$ .

Atmospheric neutrinos are subject to matter effects as they travel through the dense  
 matter in the Earth. The vacuum and matter oscillation probabilities for  $P(\nu_e \rightarrow \nu_e)$   
 and  $P(\bar{\nu}_e \rightarrow \bar{\nu}_e)$  are presented in Figure 5.3. The oscillation probability for both neutrinos  
 and antineutrinos are affected in the presence of matter but the resonance (Effects  
 around  $E_\nu \sim 5\text{GeV}$ ) only occurs for neutrinos in normal mass hierarchy and antineu-  
 trinos for inverse mass ordering. The exact position and amplitude of the resonance  
 depend on  $\sin^2(\theta_{23})$  meaning that the atmospheric neutrinos have sensitivity to the  
 octant of  $\theta_{23}$ .

As the T2K beam flux is centered at the first oscillation maximum, the sensitivity  
 to  $\delta_{CP}$  is predominantly observed as a change in the event-rate of e-like samples in  
 $\nu/\bar{\nu}$  modes. Figure 5.4 illustrates the  $P(\nu_\mu \rightarrow \nu_e)$  oscillation probability for a range  
 of  $\delta_{CP}$  values. A circular modulation of the oscillation peak (in both magnitude and  
 position) is observed when varying throughout the allowable values of  $\delta_{CP}$ . The CP-

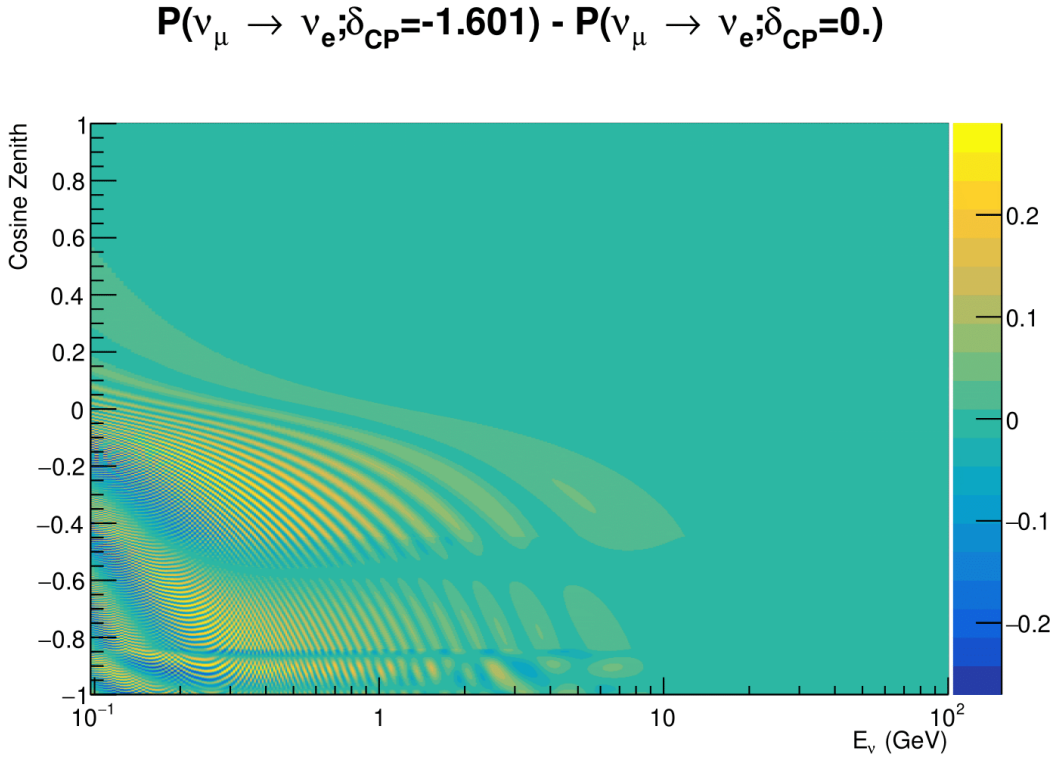


**Figure 5.2:** The effect of  $\delta_{CP}$  for atmospheric neutrinos given in terms of the neutrino energy and zenith angle. The oscillogram compares the  $P(\nu_\mu \rightarrow \nu_e)$  oscillation probability for a CP conserving ( $\delta_{CP} = 0.0$ ) and CP violating ( $\delta_{CP} = -1.601$ ) value of  $\delta_{CP}$ . The other oscillation parameters assume the “Asimov A” oscillation parameter set given in Table 5.1.

1689 conserving values of  $\delta_{CP} = 0, \pi$  have a lower(higher) oscillation maximum than the  
 1690 CP-violating values of  $\delta_{CP} = -\pi/2 (\delta_{CP} = \pi/2)$  leading to a  $\sin(\delta_{CP})$  type sensitivity.  
 1691 A sub-dominant shift in the energy of the oscillation peak is also present to aid in  
 1692 separating the two CP-conserving values of  $\delta_{CP}$ .

1693 T2K’s sensitivity to the atmospheric oscillation parameters is more of a shape-  
 1694 based variation of the muon-like samples, as illustrated in Figure 5.4. The value of  
 1695  $\Delta m_{32}^2$  laterally shifts the position of the oscillation dip (around  $E_\nu \sim 0.6$ GeV) in the  
 1696  $P(\nu_\mu \rightarrow \nu_\mu)$  oscillation probability. A variation of  $\sin^2(\theta_{23})$  is predominantly observed  
 1697 as a vertical shift of the oscillation dip with second-order horizontal shifts being due  
 1698 to matter effects. The beam neutrinos have limited sensitivity to matter effects due

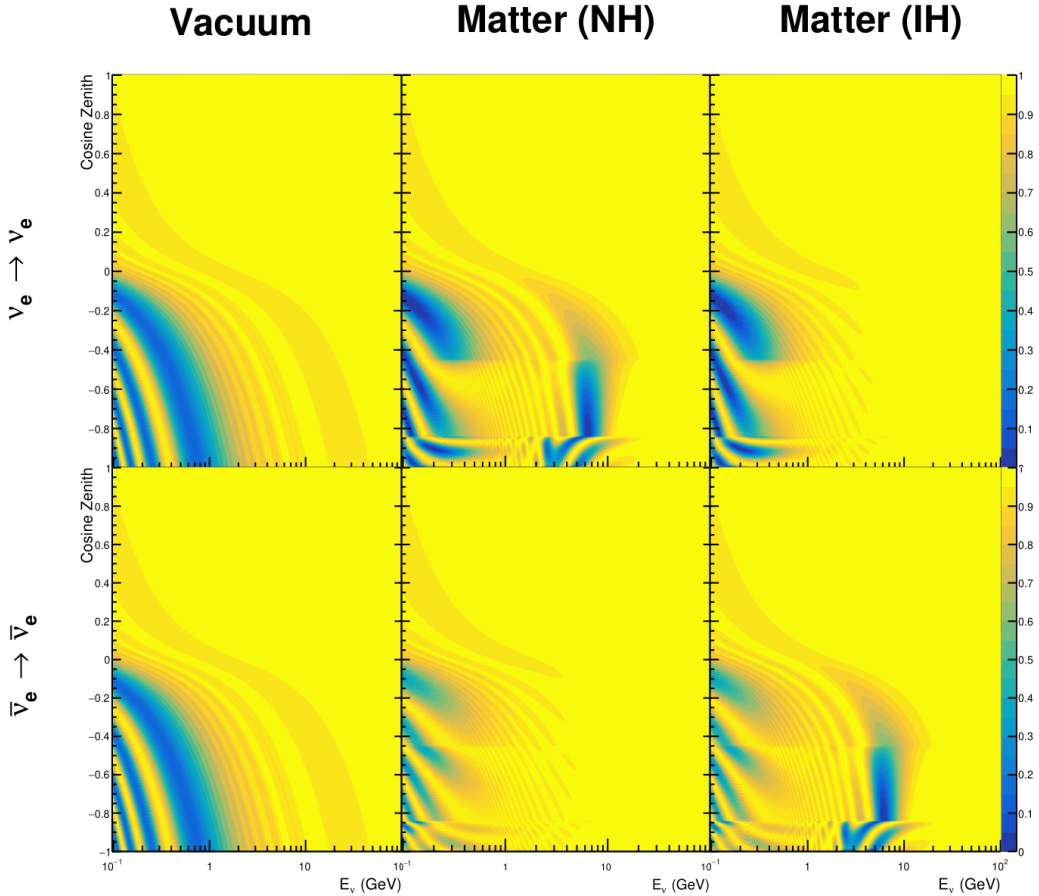


**Figure 5.3:** An illustration of the matter-induced effects on the oscillation probability, given as a function of neutrino energy and zenith angle. The top row of panels gives the  $P(\nu_e \rightarrow \nu_e)$  oscillation probability and the bottom row illustrates the  $P(\bar{\nu}_e \rightarrow \bar{\nu}_e)$  oscillation probability. The left column highlights the oscillation probability in a vacuum, whereas the middle and right column represents the oscillation probabilities when the four layer fixed density PREM model is assumed. All oscillation probabilities assume the “Asimov A” set given in Table 5.1, but importantly, the right column sets an inverted mass hierarchy. The “matter resonance” effects at  $E_\nu \sim 5\text{GeV}$  can be seen in the  $P(\nu_e \rightarrow \nu_e)$  for normal mass hierarchy and  $P(\bar{\nu}_e \rightarrow \bar{\nu}_e)$  for inverted hierarchy.

1699 to the shorter baseline as well as the Earth’s mantle is relatively low-density material  
 1700 (as compared to the Earth’s core). For some values of  $\delta_{CP}$ , the degeneracy in the  
 1701 number of e-like events allows the mass hierarchy to be resolved. This leads to a  $\delta_{CP}$   
 1702 -dependent mass hierarchy sensitivity which can be seen in Figure 5.5.

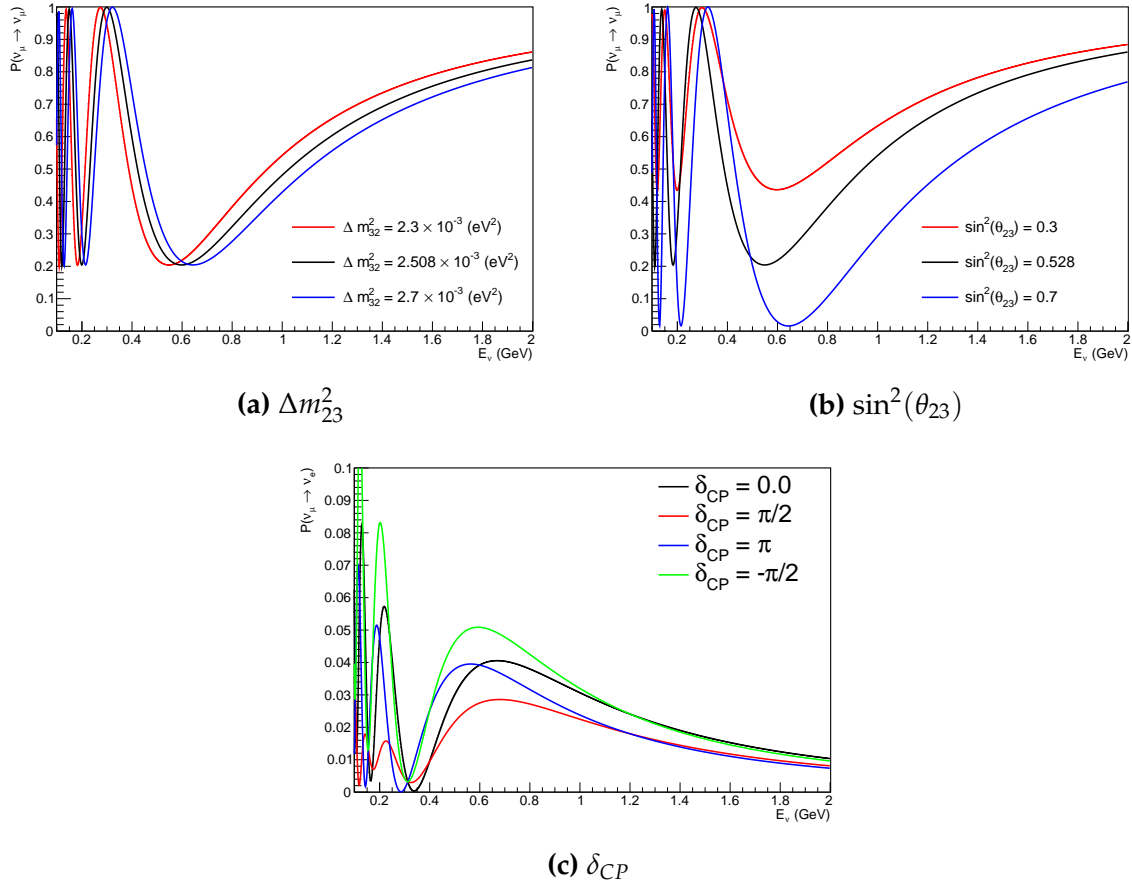


**Figure 5.4:** The oscillation probability for beam neutrino events given as a function of neutrino energy. All oscillation parameters assume the “Asimov A” set given in Table 5.1 unless otherwise stated. Each panel represents a change in one of the oscillation parameters whilst keeping the remaining parameters fixed.

Whilst all oscillation channels should be included for completeness, the computational resources required to run a fit are limited and any reasonable approximations which reduce the number of oscillation probability calculations that need to be made should be applied. The  $\nu_e \rightarrow \nu_{e,\mu,\tau}$  (and antineutrino equivalent) oscillations can be ignored for beam neutrinos as the  $\nu_e/\bar{\nu}_e$  fluxes being approximately two orders of magnitude smaller than the corresponding  $\nu_\mu/\bar{\nu}_\mu$  flux. Furthermore, as the peak neutrino energy of the beam is well below the threshold for  $\tau$  production ( $E_\nu \sim 3\text{GeV}$  [186]) only a small proportion of the neutrinos produced in the beam have the required energy. For the few neutrinos that have sufficient energy, the oscillation probability is very small due to the short baseline. Whilst these approximations can be made for the

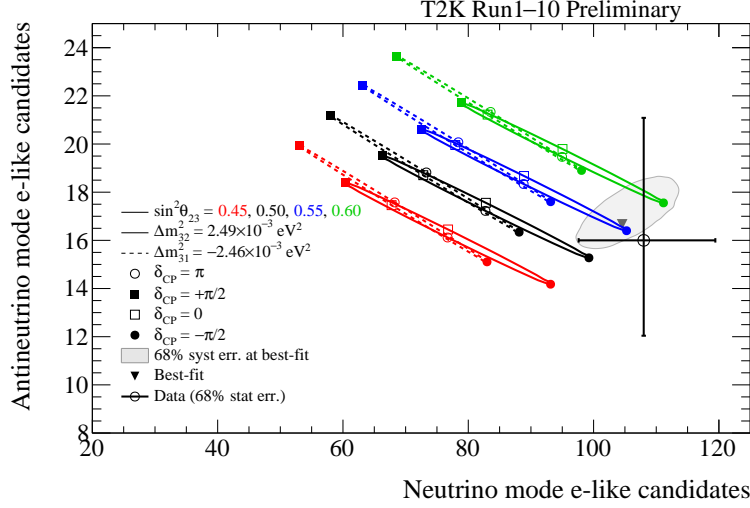


**Figure 5.5:** The number of electron-like events in the FHC and RHC operating mode of the beam, as a function of the oscillation probabilities. Both normal hierarchy (Solid) and inverse hierarchy (Dashed) values of  $\Delta m_{23}^2$  are given.

<sub>1713</sub> beam neutrinos, the atmospheric flux of  $\nu_e$  is of the same order of magnitude as the  $\nu_\mu$   
<sub>1714</sub> flux and the energy distribution of atmospheric neutrinos extends well above the tau  
<sub>1715</sub> production threshold.

<sub>1716</sub> Throughout this thesis, several spectra predictions, Asimov fits, and contour com-  
<sub>1717</sub> parisons are presented which require oscillation parameters to be assumed. Table 5.1  
<sub>1718</sub> defines two sets of oscillation parameters, with “Asimov A” set being close to the pre-  
<sub>1719</sub> ferred values from a previous T2K-only fit [187] and “Asimov B” being CP-conserving  
<sub>1720</sub> and further from maximal  $\theta_{23}$  mixing.

Parameter	Asimov A	Asimov B
$\Delta m_{12}^2$	$7.53 \times 10^{-5} \text{ eV}^2$	
$\Delta m_{32}^2$	$2.509 \times 10^{-3} \text{ eV}^2$	
$\sin^2(\theta_{12})$	0.304	
$\sin^2(\theta_{13})$	0.0219	
$\sin^2(\theta_{23})$	0.528	0.45
$\delta_{CP}$	-1.601	0.0

**Table 5.1:** Reference values of the neutrino oscillation parameters for two different oscillation parameter sets.

## 1721 5.2 Treatment of Fast Oscillations

1722 As shown in Figure 5.6, atmospheric neutrino oscillations have a significantly more  
1723 complex structure for upgoing neutrinos with energy below 1GeV. This is because the  
1724  $L/E$  dependence of the oscillation probability in this region induces rapid variations  
1725 for small changes in  $L$  or  $E$ . As discussed in section 5.1, this is also the region in which  
1726 atmospheric neutrinos have sensitivity to  $\delta_{CP}$ . In practice, the direction between  
1727 the detector and a neutrino's production vertex is inferred from the direction of any  
1728 secondary particles created in the detector target. For low-energy neutrinos, this  
1729 inference can be rather poor and introduces a distinct difference to beam neutrinos  
1730 where the direction to production vertex is very well known.

1731 As a consequence of the poor detector resolution, an average oscillation probability  
1732 is observed in this region. This creates a computational problem as a significantly  
1733 large amount of MC statistics would be required to accurately predict the number  
1734 of events in each bin if MC averaging was the only technique used. This section  
1735 describes the ‘sub-sampling’ approach developed for this analysis and compares it to  
1736 the methodology used within the SK-only analysis.

1737 The official SK-only analysis uses the osc3++ oscillation parameter fitter [188]. To  
1738 perform the fast oscillation averaging, it uses a ‘nearest-neighbour’ technique. For a  
1739 given neutrino MC event, the nearest neighbours in reconstructed lepton momentum  
1740 and zenith angle are found and a distribution of neutrino energies is built. This  
1741 distribution is then used to compute an average oscillation probability for the given  
1742 neutrino MC event.

1743 For the  $i^{th}$  event, the oscillation weight is calculated as

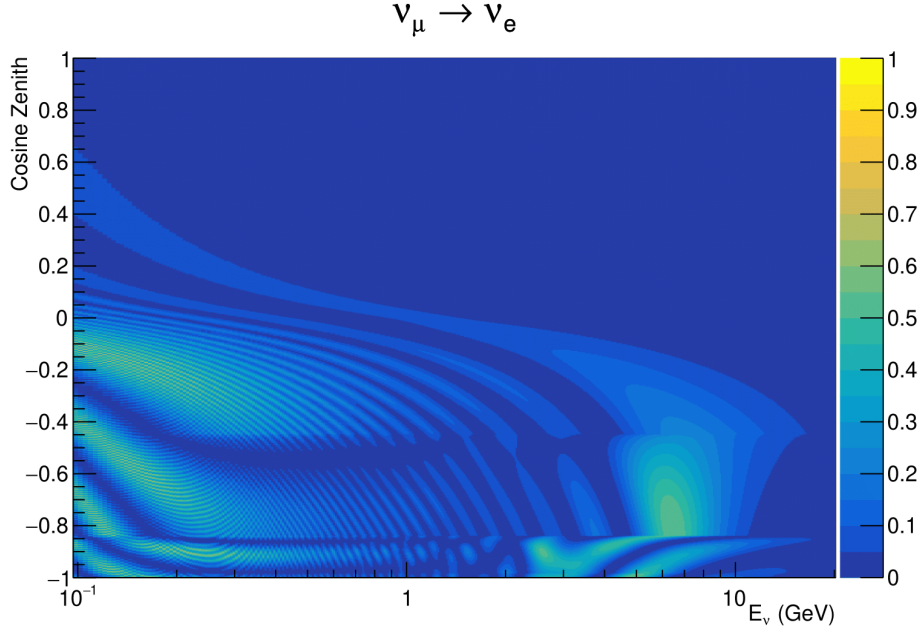


**Figure 5.6:** The oscillation probability  $P(\nu_\mu \rightarrow \nu_e)$ , given as a function of neutrino energy and zenith angle, which highlights an example of the “fast” oscillations in the sub-GeV upgoing region.

$$W_i = \frac{1}{5}P(E_i, \bar{L}_i) + \frac{1}{5} \sum_{\beta=-1, -0.5, 0.5, 1} P(E_i + \beta\sigma_i, L_\beta), \quad (5.2)$$

where  $P(E, L)$  is the oscillation probability calculation for neutrino energy  $E$  and path length  $L$ ,  $\sigma_i$  is the RMS of the energy distribution for the given event, and the two path lengths,  $\bar{L}_i$  and  $L_\beta$  are discussed below. In practice, twenty of the nearest neighbours are used to generate the neutrino energy distribution. All of the oscillation probability calculations are performed with a fixed zenith angle (and therefore have same matter density profile).

The uncertainty in the production height is controlled by using an “average” production height.  $\bar{L}_i$  represents the average path length computed using twenty production heights taken from the Honda flux model’s prediction [45] for a fixed zenith angle, where the production heights are sampled in steps of 5% of their cumulative

<sub>1754</sub> distribution function.  $L_\beta$  values are similarly calculated but instead use different  
<sub>1755</sub> combinations of four production heights (sampled in the same way),

$$\begin{aligned} L_{-1.0} &= \frac{1}{4}L(45, 50, 55, 60), \\ L_{-0.5} &= \frac{1}{4}L(35, 40, 65, 70), \\ L_{+0.5} &= \frac{1}{4}L(25, 30, 75, 68), \\ L_{+1.0} &= \frac{1}{4}L(15, 20, 85, 89). \end{aligned} \tag{5.3}$$

<sub>1756</sub> This averaging works well because of the correlation between the true neutrino  
<sub>1757</sub> zenith angle and the inferred direction from secondary particles in the detector. For  
<sub>1758</sub> low-energy neutrinos, where the resolution of the true neutrino direction is poor,  $\sigma_i$   
<sub>1759</sub> will be large, resulting in significant averaging effects. Contrary to this, the inferred  
<sub>1760</sub> direction of high-energy neutrinos will be much closer to the true value, meaning that  
<sub>1761</sub>  $\sigma_i$  will be smaller.

<sub>1762</sub> In practice, this technique is performed before the fit in order to deal with the  
<sub>1763</sub> computational cost. Oscillation probabilities are pre-calculated on a 4D grid. This  
<sub>1764</sub> is possible as the Osc3++ framework uses binned oscillation parameters rather than  
<sub>1765</sub> continuous so the oscillation parameters used in the fit are known prior to run-time.  
<sub>1766</sub> The framework used in the analysis presented within this thesis uses continuous  
<sub>1767</sub> oscillation parameters. Due to the MCMC technique invoked within the fitter (see  
<sub>1768</sub> chapter 3), there is no way to know which oscillation parameter values will be selected  
<sub>1769</sub> in each step at run-time. Therefore, the oscillation parameter calculation would have  
<sub>1770</sub> to be performed at run-time which is very expensive for event-by-event reweighting.  
<sub>1771</sub> Having to compute five oscillation probabilities per event would require far too many

<sub>1772</sub> computational resources to be viable so the SK technique can not be used within this  
<sub>1773</sub> analysis. However, the concept of the averaging technique can be taken from it.

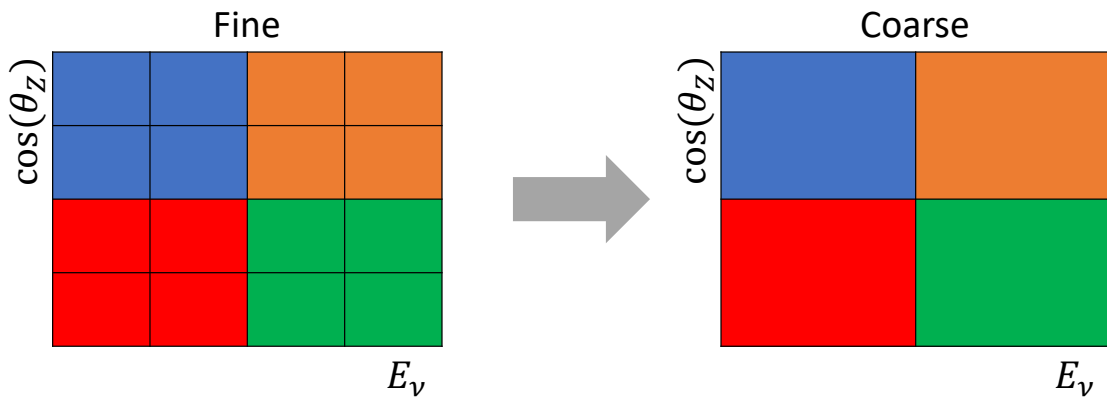


**Figure 5.7:** Illustration of the averaging procedure for  $N = 2$ . The oscillation probabilities calculated on the finer left binning are averaged to obtain the oscillation probabilities in the coarser right binning. These averaged oscillation probabilities with the coarser binning are then applied to each event during the fit.

<sub>1774</sub> This analysis uses a binned oscillogram in which oscillation probabilities for a given  
<sub>1775</sub> event are selected based on that event's attributes. To perform a similar averaging as  
<sub>1776</sub> the SK analysis, a sub-sampling approach has been devised. The technique can be  
<sub>1777</sub> explained by considering a "fine" and "coarse" oscillogram. The fine oscillograms  
<sub>1778</sub> are used to define the array of cosine zeniths and energies for the neutrino oscillation  
<sub>1779</sub> engine. The coarse oscillograms cover the same phase-space as the fine oscillograms  
<sub>1780</sub> but have fewer bins in that range. Then, for a given coarse oscillogram bin, the value  
<sub>1781</sub> of that bin will be taken as the average of all the oscillation probabilities of all the fine  
<sub>1782</sub> oscillogram bins which fall into that coarse oscillogram bin.

<sub>1783</sub> The binning which is used to calculate the oscillation probabilities, known as the  
<sub>1784</sub> 'fine' binning, has  $N \times N$  subdivisions per coarse bin. The value assigned to a coarse  
<sub>1785</sub> bin is the linear average (flat prior in  $E_\nu$  and  $\cos(\theta_Z)$ ) of all the oscillation probabilities  
<sub>1786</sub> calculated at the center of each fine bin contained within that coarse bin. Figure 5.7  
<sub>1787</sub> illustrates the  $N = 2$  example where the assigned value to a coarse bin is the linear

1788 average of the four fine bins which fall in that coarse bin. Whilst the coarse bin edges  
1789 are not linear on either axis, the sub-division of the fine bins is linear over the range  
1790 of a coarse bin. The alignment of the fine and coarse binning edges is checked at  
1791 run-time.

1792 The coarse binning is defined with  $67 \times 52$  bins in true neutrino energy  $\times$  cosine  
1793 zenith. In general, the binning is logarithmically spaced in neutrino energy but has  
1794 some hand-picked bin edges. Firstly, the bin density around the matter resonance is  
1795 smoothly increased around the matter resonance region. This is to avoid smearing  
1796 this region which can be well sampled by the Monte Carlo. Secondly, bin edges  
1797 are selected to hit  $0.4, 0.6, 1, 10, 30, 50, 100\text{GeV}$ . This is to ensure that the Coloumb  
1798 correction systematic and the atmospheric flux systematics definitions in neutrino  
1799 energy can be hit. The cosine zenith binning is approximately linearly spaced across  
1800 the allowable range but the values of layer transitions are hit precisely;  $-0.8376$   
1801 (core-mantle) and  $-0.4464$  (mantle/transition zone). Bins are spread further apart for  
1802 downgoing events as this is a region unaffected by the fast oscillation wavelengths  
1803 and reduces the total number of calculations required to perform the reweight (Not  
1804 the number required to perform the oscillation calculation).

1805 The choice of  $N$  is justified based on two studies. Firstly, the variation of event  
1806 rates of each sample is studied as a function of the number of subdivisions. For  
1807 a given set of oscillation parameters thrown from the PDG prior constraints, the  
1808 oscillation probabilities are calculated using a given value of  $N$ . Each sample is re-  
1809 weighted and the event rate is stored. The value of  $N$  is scanned from 1, which  
1810 corresponds to no averaging, to 24, which corresponds to the largest computationally  
1811 viable subdivision binning. The event rate of each sample at large  $N$  is expected to  
1812 converge to a stationary value due to the fine binning fully sampling the small-scale

1813 structure. Figure 5.8 illustrates this behaviour for the SubGeV\_elike\_0dcy sample for  
 1814 30 different throws of the oscillation parameters.

### SubGeV-elike-0dcy

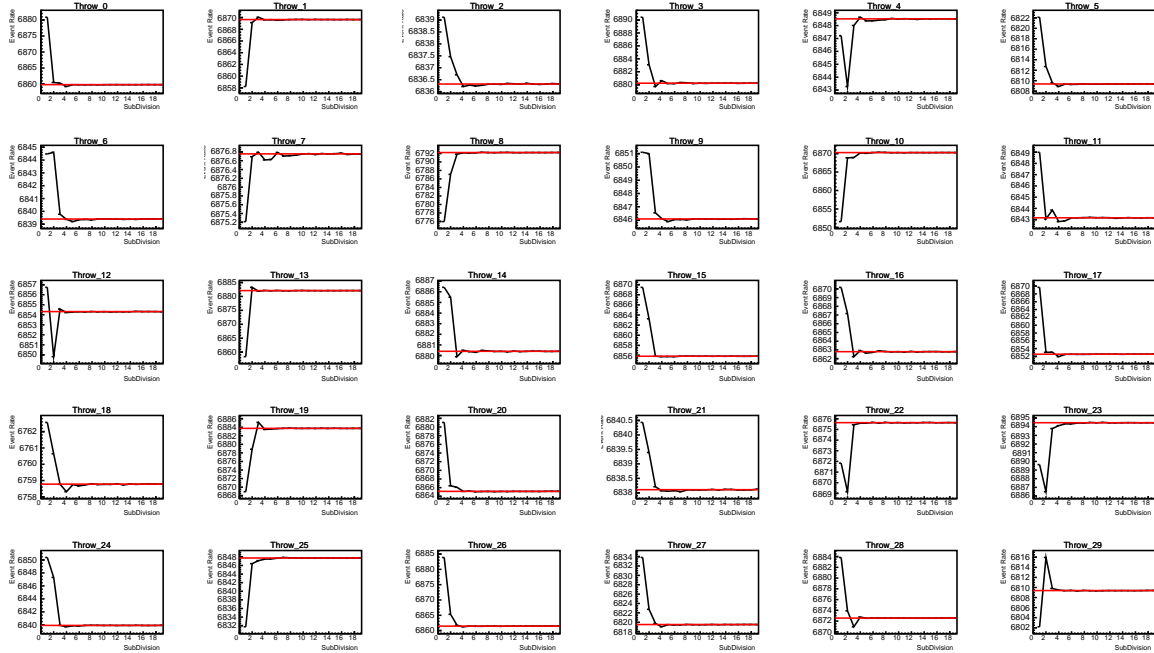


**Figure 5.8:** Event rate of the SubGeV\_elike\_0dcy sample as a function of the number of subdivisions per coarse bin. Each subplot represents the event rate of the sample at a different oscillation parameter set (thrown from the PDG priors). The red line in each subplot represents the mean of the event rate over the different values of sub-divisions for that particular oscillation parameter throw.

1815 Denoting the event rate for one sample for a given throw  $t$  at each  $N$  by  $\lambda_t^{(N)}$ , the  
 1816 average over all considered  $N$  values ( $\bar{\lambda}_t = \frac{1}{24} \sum_{N=1}^{24} \lambda_t^{(N)}$ ) is computed. The variance  
 1817 in the event rate at each  $N$  is then calculated from

$$\text{Var}[\lambda^{(N)}] = \frac{1}{N_{\text{throws}}} \sum_{t=1}^{N_{\text{throws}}} \left( \lambda_t^{(N)} - \bar{\lambda}_t \right)^2 - \left[ \frac{1}{N_{\text{throws}}} \sum_{t=1}^{N_{\text{throws}}} \left( \lambda_t^{(N)} - \bar{\lambda}_t \right) \right]^2. \quad (5.4)$$

1818 The aim of the study is to find the lowest value of  $N$  such that this variance is  
 1819 below 0.001. This is the typical threshold used by T2K fitters to validate systematic  
 1820 implementation so is just as applicable to the oscillation probability calculation. The  
 1821 results of this study for each atmospheric sample used within this thesis are illustrated  
 1822 in Figure 5.9 for 2000 throws of the oscillation parameters. As can be seen, the variance  
 1823 is below the threshold at  $N = 10$ , and is driven primarily by the SubGeV\_mulike\_1dcy  
 1824 and SubGeV\_elike\_0dcy selections.

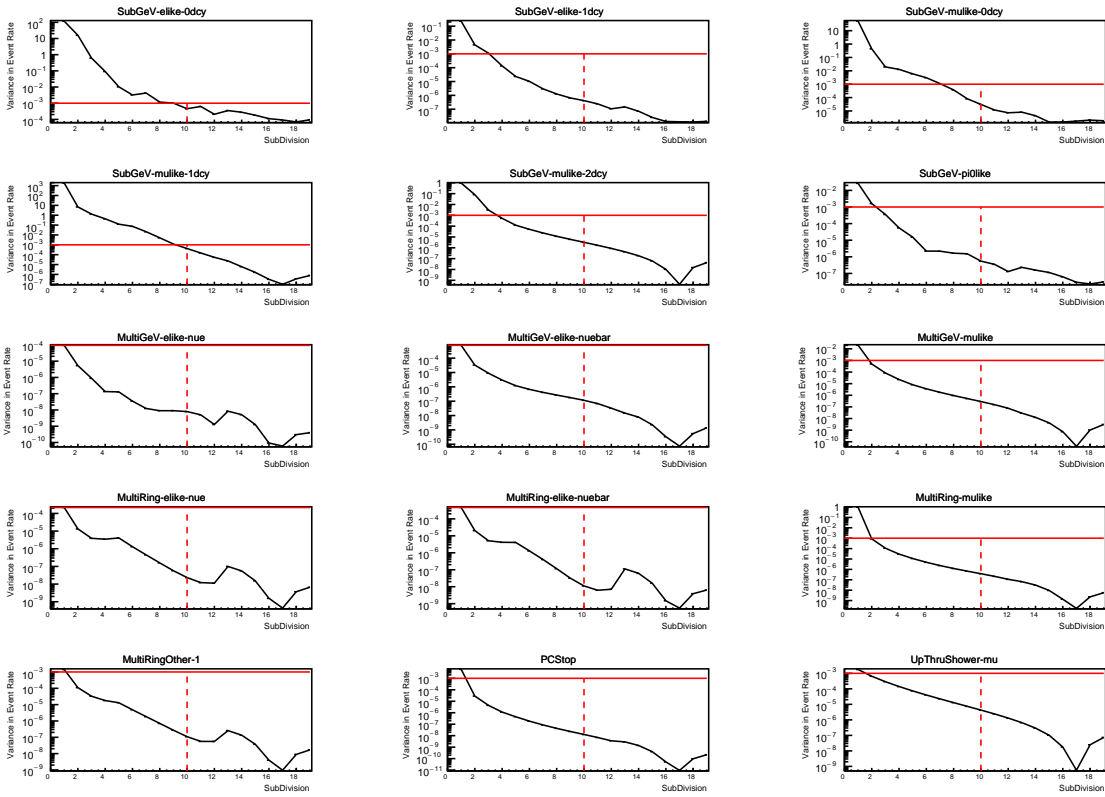


**Figure 5.9:** Variance of event rate for each atmospheric sample as a function of the number of sub-divisions per coarse bin. The solid red line indicates the 0.1% threshold and the dashed red line is a graphical indication of the variance at a sub-division  $N = 10$ .

1825 The second study to determine the value of  $N$  is as follows. The likelihood for  
 1826 each sample is computed against an Asimov data set created with oscillation pa-  
 1827 rameters from “Asimov A” in Table 5.1. Following Equation 5.4, the variance of the  
 1828 log-likelihood over all considered  $N$  is computed. The results are shown in Figure 5.10.

1829 This tests the impact of the averaging on each sample's binning by reconstructed  
 1830 momentum and/or zenith angle and also provides a scale for the calculation errors  
 1831 compared to their statistical uncertainties.

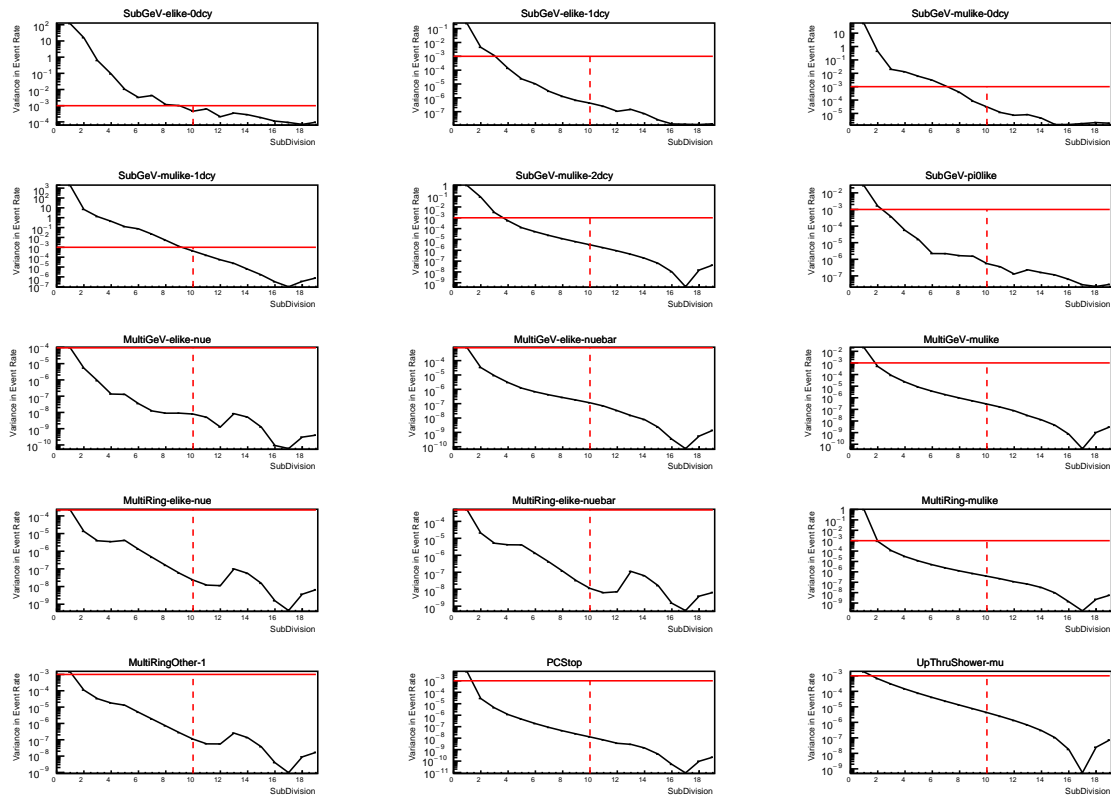


**Figure 5.10:** Variance of sample likelihood, when compared to 'Asimov data' set at Asimov A, for each atmospheric sample as a function of the number of sub-divisions per coarse bin. The solid red line indicates the 0.1% threshold and the dashed red line is a graphical indication of the variance at a sub-division  $N = 10$ .

1832 A choice of  $N$  sub-divisions per coarse bin has a variance in both event rate and  
 1833 log-likelihood residuals less than the required threshold of 0.001. The event rate test is  
 1834 the more stringent test. For the variance of log-likelihood residuals, the largest value is  
 1835 of order  $10^{-7}$ , corresponding to an error on the log-likelihood of about  $3 \times 10^{-4}$ , small  
 1836 enough to be negligible for the oscillation analysis.

<sup>1837</sup> In practice Figure 5.11 illustrates the effect of the smearing using  $N = 10$ . The fast  
<sup>1838</sup> oscillations in the sub-GeV upgoing region have been replaced with a normalisation  
<sup>1839</sup> effect whilst the large matter resonance structure remains.

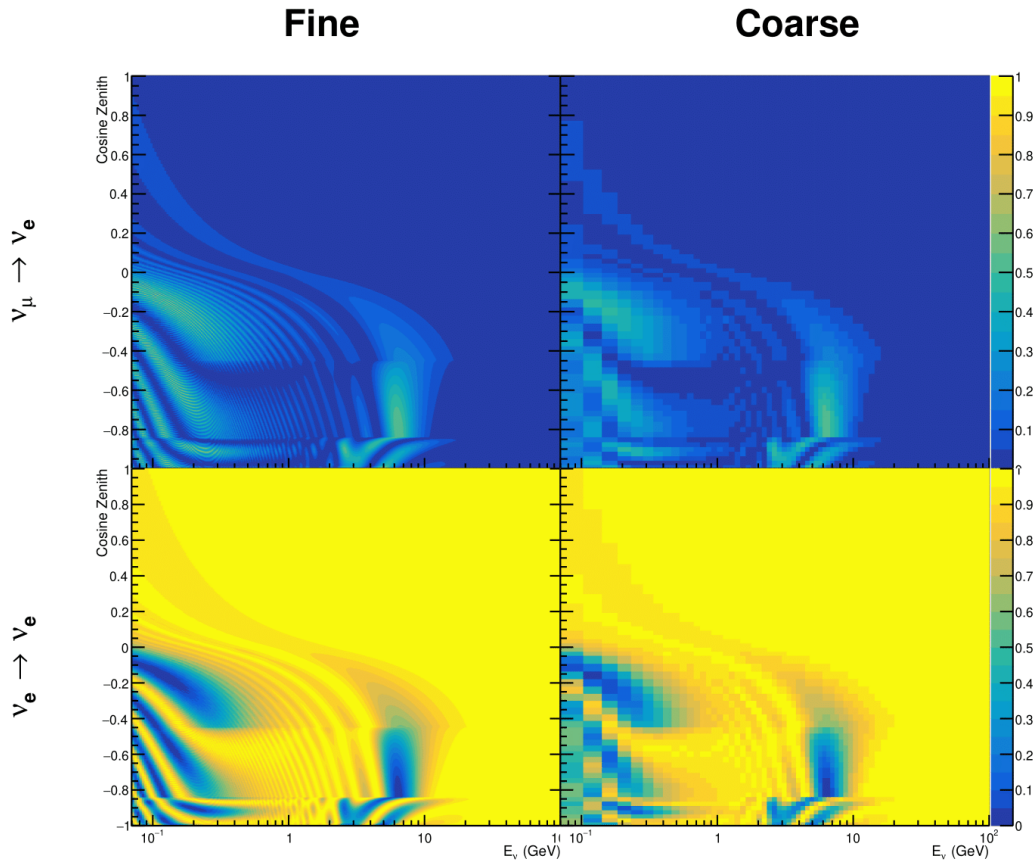


**Figure 5.11:** The oscillation probability,  $P(\nu_\mu \rightarrow \nu_e)$  (top row) and  $P(\nu_e \rightarrow \nu_e)$  (bottom row), given as a function of neutrino energy and zenith angle. The left column gives the “fine” binning used to calculate the oscillation probabilities and the right column illustrates the “coarse” binning used to reweight the MC events. The fine binning choice is given with  $N = 10$ , which was determined to be below threshold from Figure 5.9 and Figure 5.10.

## 1840 5.3 Calculation Engine

1841 As previously discussed in section 5.2, the calculation of oscillation probabilities is per-  
1842 formed at run-time due to utilising continuous oscillation parameters. Consequently,  
1843 the time per calculation is crucial for fit performance. The fitting framework used for  
1844 this analysis was developed with ProbGPU [189]. This is a GPU-only implementation  
1845 of the prob3 engine [190]. It is primarily designed for neutrino propagation in a beam  
1846 experiment (single layer of constant density) with the atmospheric propagation code  
1847 not being used prior to the analysis in this thesis.

1848 Another engine, CUDAProb3 [191], has been implemented within the fitting frame-  
1849 work used within this analysis. It has been specifically optimised for atmospheric  
1850 neutrino oscillation calculation so unfortunately does not contain the code to replace  
1851 the beam oscillation calculation. Based on the benefits shown by the implementation  
1852 in this chapter, efforts are being placed into including linear propagation for beam  
1853 neutrino propagation into the engine [192]. The engine utilises object-orientated tech-  
1854 niques as compared to the functional implementation of ProbGPU. This allows the  
1855 energy and cosine zenith arrays to be kept on GPU memory, rather than having to  
1856 load these arrays onto GPU memory for each calculation. General memory interfacing  
1857 is one of the slowest tasks which GPUs can do, so being able to eliminate this signifi-  
1858 cantly reduces the time required for calculation. This can be seen in Figure 5.12, where  
1859 the GPU implementation of CUDAProb3 is approximately three times faster than the  
1860 ProbGPU engine.

1861 Another significant advantage of CUDAProb3 is that it contains a CPU multithreaded  
1862 implementation which is not possible with the ProbGPU or prob3 engines. This elimi-  
1863 nates the requirement for GPU resources when submitting jobs to batch systems. As  
1864 illustrated in Figure 5.12, the calculation speed depends on the number of available

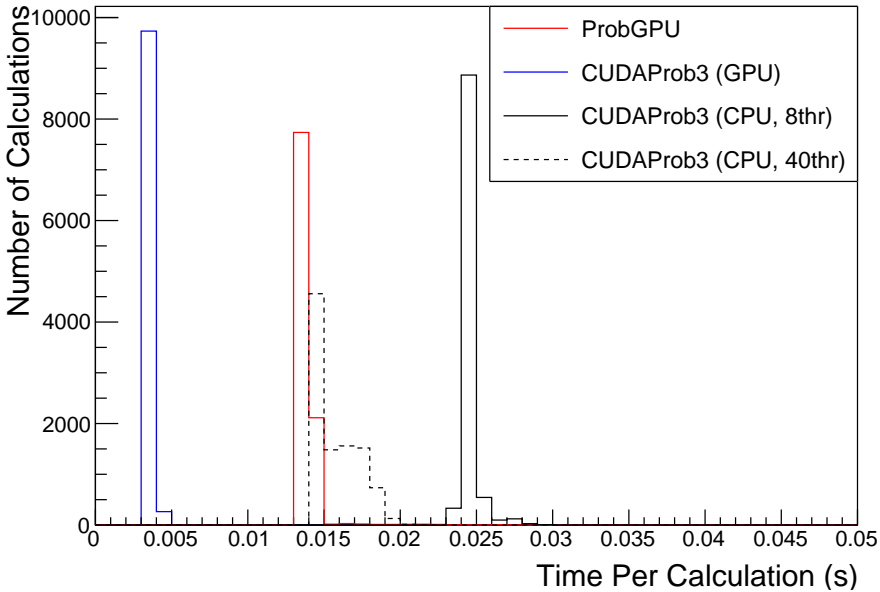


**Figure 5.12:** The calculation time taken to both calculate the oscillation probabilities and fill the “coarse” oscillograms, following the technique given in section 5.2, for the CUDAProb3 and ProbGPU (Red) calculation engines. CUDAProb3 has both a GPU (Blue) and CPU (Black) implementation, where the CPU implementation is multithreaded. Therefore, 8-threads (solid) and 40-threads (dashed) configurations have been used. Prob3, which is a CPU single-thread implementation has a mean step time of 1.142s.

1865 threads. Using 8 threads (which is typical of the batch systems being used) is ap-  
 1866 proximately twice as slow as the ProbGPU engine implementation, but would allow  
 1867 the fitting framework to be run on many more resources. This fact is utilised for any  
 1868 SK-only fits but GPU resources are required for any fits which include beam samples  
 1869 due to the ProbGPU requirement.

## 1870 5.4 Matter Density Profile

1871 For an experiment observing atmospheric neutrinos propagating through the Earth,  
 1872 such as the studies presented in this thesis, a model of the Earth’s density and layering  
 1873 is required. The model used within this analysis is the Preliminary Reference Earth  
 1874 Model (PREM) [193]. This model provides piecewise cubic polynomials as a function

of radius which results in the density profile illustrated in Figure 5.13. As will be discussed in section 5.5, the propagator used within the calculation engine requires constant density layers. To follow the official SK-only analysis [188], the average density of each layer has been taken from the PREM model. Table 5.2 documents the density and radii of the layers used within this approximation.

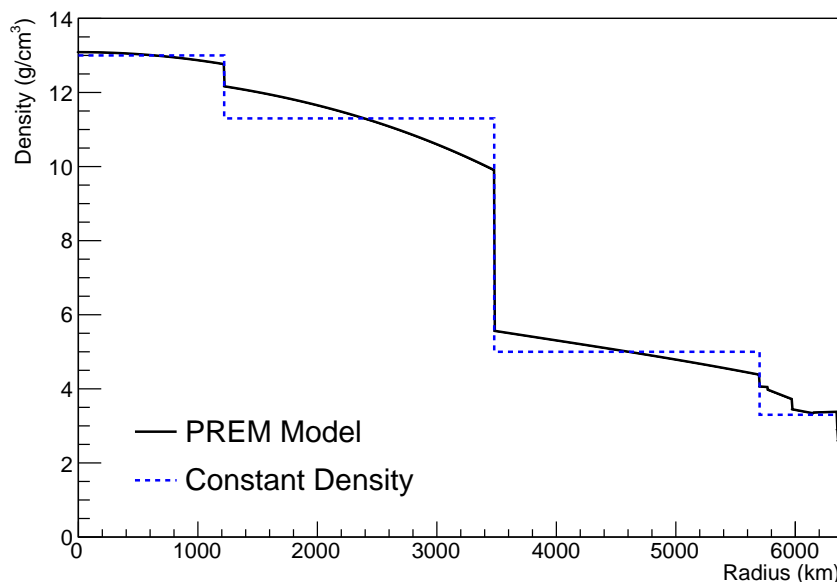


**Figure 5.13:** The density of the Earth given as a function of the radius, as given by the PREM model (Black) and the constant density four-layer approximation (Blue), as used in the official SK-only analysis.

Layer	Outer Radius [km]	Density [g/cm <sup>3</sup> ]	Chemical composition (Z/A)
Inner Core	1220	13	$0.468 \pm 0.029$
Outer Core	3480	11.3	$0.468 \pm 0.029$
Lower Mantle	5701	5.0	0.496
Transition Zone	6371	3.3	0.496

**Table 5.2:** Description of the four layers of the Earth invoked within the average constant density approximation of the PREM model [193].

The density measurements provided in the PREM model are provided in terms of mass density, whereas neutrino oscillations are sensitive to the electron number density. This value can be computed as the product of the chemical composition, or

1883 the  $Z/A$  value, and the mass density of each layer. Currently, the only way to calculate  
 1884 this value for layers close to the Earth's core is through neutrino oscillations. The  
 1885 chemical composition of the upper layers of the Earth's Mantle and the Transition  
 1886 zone is well known due to it being predominantly pyrolite which has a chemical  
 1887 composition value of 0.496 [194]. The components of the Earth's core region are less  
 1888 well known. Consequently, the chemical composition dial for the core layers is set  
 1889 to a value of 0.468 [195]. This value is assigned a Gaussian error with a standard  
 1890 deviation equivalent to the difference in chemical composition in core and mantle  
 1891 layers. Figure 5.14 illustrates the effect of moving from the  $Z/A = 0.5$  method which  
 1892 is used in the official SK-only analysis [188] to more precise values recorded by other  
 1893 neutrino experiments.

1894 The beam oscillation probability in this thesis uses a baseline of 295km, density  
 1895  $2.6\text{g/cm}^3$  [196], and chemical composition 0.5 as is done by the official T2K-only  
 1896 analysis.

1897 Whilst the propagator requires a fixed density layer model of the Earth, the density  
 1898 only has to be fixed for a specific neutrino energy  $\times \cos(\theta_Z)$  bin in a given layer (I.e.  
 1899 set of values at which to calculate the oscillation probability). As the density is a  
 1900 function of radius, which is a function of the direction in which a neutrino propagates,  
 1901 a better approximation of the PREM model can be made if a  $\cos(\theta_Z)$ -specific density is  
 1902 calculated.

1903 To achieve this, the average density,  $\langle \rho \rangle_i$ , in the  $i^{th}$  layer, is calculated as the density,  
 1904  $\rho$ , integrated over the track a given  $\cos(\theta_Z)$ ,

$$\langle \rho \rangle_i = \frac{1}{t_{i+1} - t_i} \int_{t_i}^{t_{i+1}} \rho(t) dt \quad (5.5)$$

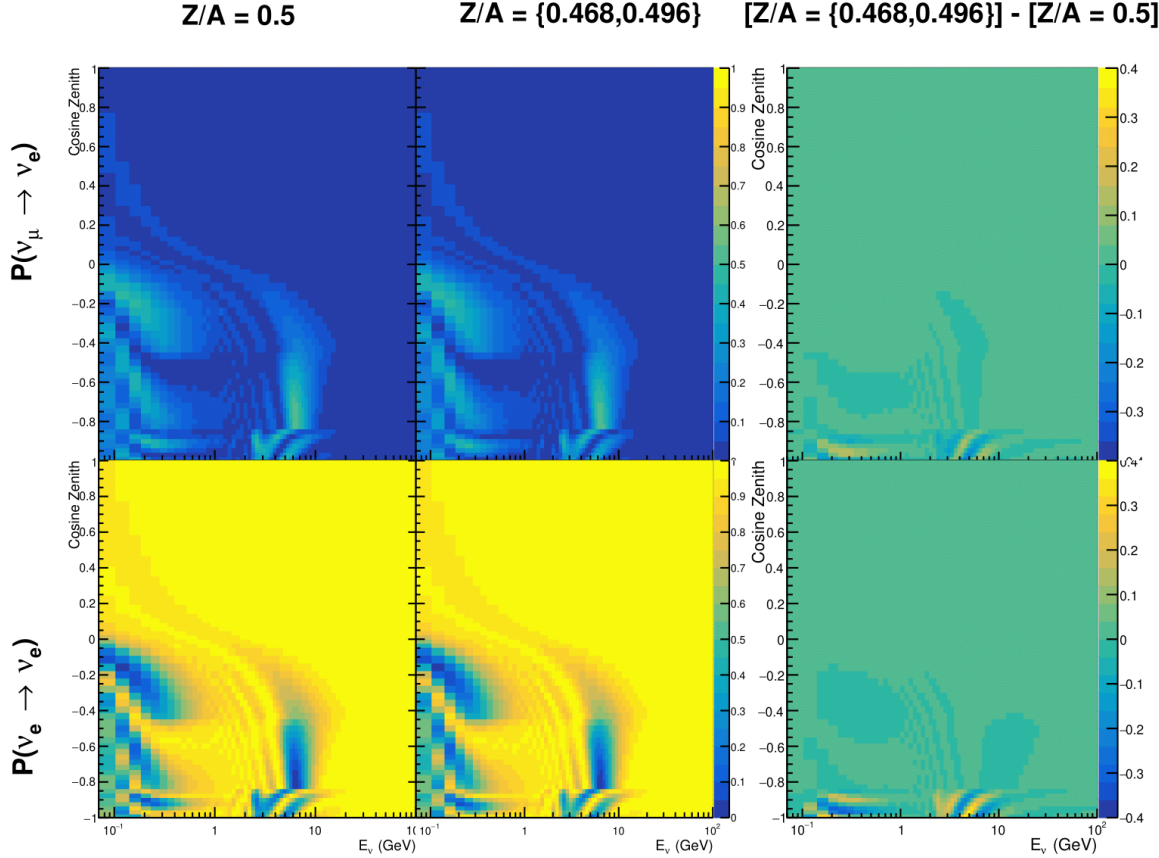


**Figure 5.14:** The oscillation probability,  $P(\nu_\mu \rightarrow \nu_e)$  (top row) and  $P(\nu_e \rightarrow \nu_\mu)$  (bottom row), given as a function of neutrino energy and zenith angle. The left column gives probabilities where the constant  $Z/A = 0.5$  approximation which is used in the official SK-only analysis. The middle column gives the probabilities where the more accurate  $Z/A = [0.468, 0.498]$  values as given in Table 5.2. The right column illustrates the difference in oscillation probability between the two different techniques.

where  $t_i$  are the intersection points between each layer and  $t$  is the path length of

the trajectory across the layer which is dependent upon  $\cos(\theta_Z)$ .

The oscillation probability calculation speed is approximately linear in the number of layers invoked within the Earth model. Therefore a four-layer model is still utilized with the only difference to the above example being that the four-layer model used for each value of  $\cos(\theta_Z)$  is different. Following the method outlined in [197], a four-layer piecewise quadratic polynomial is fit to the PREM model for the four layers defined in

<sup>1912</sup> Table 5.2. This fit was not performed by the author of the thesis and is documented  
<sup>1913</sup> in [198]. The coefficients of the quadratic fit to each layer are given in Table 5.3 with  
<sup>1914</sup> the final distribution illustrated in Figure 5.15. The quadratic approximation is clearly  
<sup>1915</sup> much closer to the PREM model as compared to the constant density approximation.

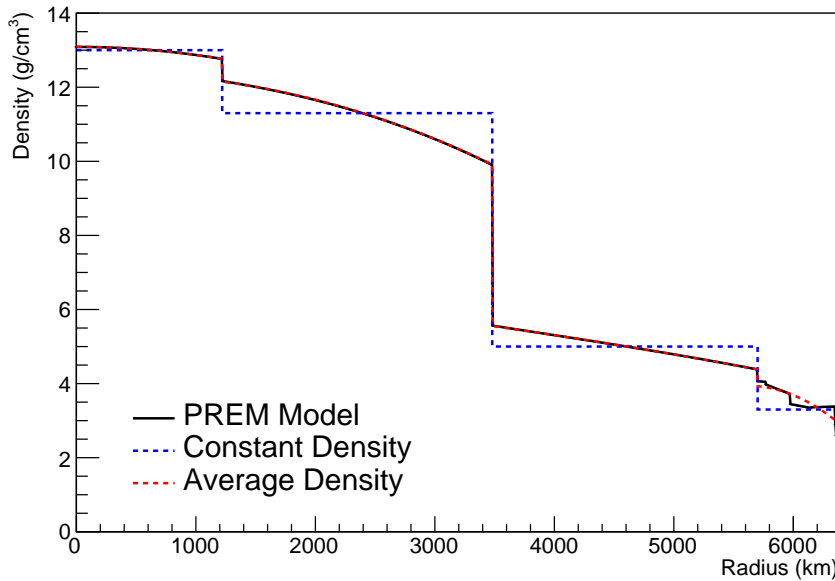


**Figure 5.15:** The density of the Earth given as a function of the radius, as given by the PREM model (Black), the constant density four-layer approximation (Blue), as used in the official SK-only analysis, and the quadratic approximation of the PREM model (Red).

Layer	Outer Radius [km]	Density [g/cm <sup>3</sup> ]
Inner Core	1220	$13.09 - 8.84x^2$
Outer Core	3480	$12.31 + 1.09x - 10.02x^2$
Lower Mantle	5701	$6.78 - 1.56x - 1.25x^2$
Transition Zone	6371	$-50.42 + 123.33x - 69.95x^2$

**Table 5.3:** The quadratic polynomial fits to the PREM model for four assumed layers of the PREM model. The fit to calculate the coefficients is given in [198], where  $x = R/R_{Earth}$ .

<sup>1916</sup> The effect of using the average density per  $\cos(\theta_Z)$  model is highlighted in Fig-  
<sup>1917</sup> ure 5.16. The slight discontinuity in the oscillation probability around  $\cos(\theta_Z) \sim -0.45$   
<sup>1918</sup> in the fixed density model, which is due to the transition to mantle layer boundary, has

1919 been reduced. This is expected as the difference in the density across this boundary is  
1920 significantly smaller in the average density model as compared to the constant density  
1921 model. Whilst the difference in density across the other layer transitions is reduced,  
1922 there is still a significant difference. This means the discontinuities in the oscillation  
1923 probabilities remain but are significantly reduced. However, as the average density  
1924 approximation matches the PREM model well in this region, these discontinuities are  
1925 due to the Earth model rather than an artifact of the oscillation calculation.

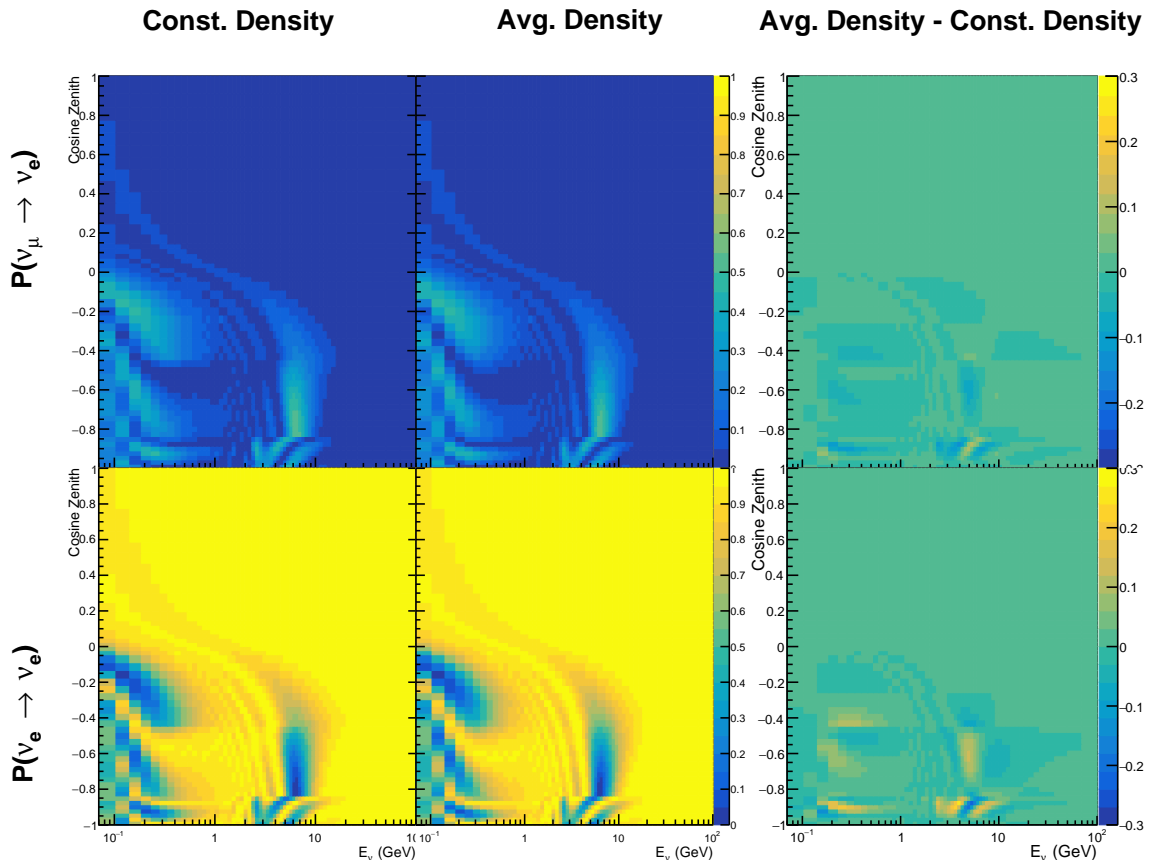


**Figure 5.16:** The oscillation probability,  $P(\nu_\mu \rightarrow \nu_e)$  (top row) and  $P(\nu_e \rightarrow \nu_\mu)$  (bottom row), given as a function of neutrino energy and zenith angle. The left column gives probabilities where the four-layer constant density approximation is used. The middle column gives the probabilities where the density is integrated over the trajectory, using the quadratic PREM approximation, for each  $\cos(\theta_Z)$  is used. The right column illustrates the difference in oscillation probability between the two different techniques.

## <sup>1926</sup> 5.5 Production Height Averaging

<sup>1927</sup> As discussed in section 5.1, the height at which the cosmic ray flux interacts in the  
<sup>1928</sup> atmosphere is not known on an event-by-event basis. The production height can  
<sup>1929</sup> vary from the Earth's surface to 50km above that. The SK-only analysis methodol-  
<sup>1930</sup> ogy (described in section 5.2) for including the uncertainty on the production height  
<sup>1931</sup> is to include variations from the Honda model when pre-calculating the oscillation  
<sup>1932</sup> probabilities prior to the fit. This technique is not possible for this analysis which  
<sup>1933</sup> uses continuous oscillation parameters that can not be known prior to the fit. Conse-  
<sup>1934</sup> quently, an analytical averaging technique was developed in [198]. The author of this  
<sup>1935</sup> thesis was not responsible for the derivation of the technique but has performed the  
<sup>1936</sup> implementation and validation of the technique for this analysis alone.

<sup>1937</sup> The oscillation probability used within this analysis is based on [21]. The neutrino  
<sup>1938</sup> wavefunction in the vacuum Hamiltonian evolves in each layer of constant matter  
<sup>1939</sup> density via

$$i \frac{d\psi_j(t)}{dt} = \frac{m_j^2}{2E_\nu} \psi_j(t) - \sum_k \sqrt{2} G_F N_e U_{ej} U_{ke}^\dagger \psi_k(t), \quad (5.6)$$

<sup>1940</sup> where  $m_j^2$  is the square of the  $j^{th}$  vacuum eigenstate mass,  $E_\nu$  is the neutrino energy,  
<sup>1941</sup>  $G_F$  is Fermi's constant,  $N_e$  is the electron number density and  $U$  is the PMNS matrix.  
<sup>1942</sup>  $N_e \rightarrow -N_e$  and  $\delta_{CP} \rightarrow -\delta_{CP}$  for antineutrino propagation.

<sup>1943</sup> Using the 20 production heights per MC neutrino event, provided as 5% percentiles  
<sup>1944</sup> from the Honda flux model, a production height distribution  $p_j(h|E_\nu, \cos \theta_Z)$  is built  
<sup>1945</sup> for each neutrino flavour  $j = \nu_e, \bar{\nu}_e, \nu_\mu, \bar{\nu}_\mu$ . In practice, a histogram is filled with 20  
<sup>1946</sup> evenly spaced bins in production height  $h$  between 0 and 50km. The neutrino energy

<sup>1947</sup> and cosine zenith binning is the same as that provided in section 5.2. The average  
<sup>1948</sup> production height,  $\bar{h} = \int dh \frac{1}{4} \sum_j p_j(h|E_\nu, \cos(\theta_Z))$ , is calculated. The production height  
<sup>1949</sup> binning of this histogram is then translated into  $\delta t(h) = t(z, \bar{h}) - t(z, h)$ , where  $t(z, h)$   
<sup>1950</sup> is the distance travelled along the trajectory.

<sup>1951</sup> For the  $i^{th}$  traversed layer, the transition amplitude,  $D_i(t_{i+1}, t_i)$ , is computed. The  
<sup>1952</sup> time ordered product of these is then used as the overall transition amplitude via

$$A(t_{n+1}, t_0) = D_n(t_{n+1}, t_n) \dots D_1(t_2, t_1) D_0(t_1, t_0), \quad (5.7)$$

<sup>1953</sup> where,

$$\begin{aligned} D_n(t_{n+1}, t_n) &= \exp[-iH_n(t_{n+1} - t_n)] \\ &= \sum_{k=1}^3 C_k \exp[ia_k \delta t] \end{aligned} \quad (5.8)$$

<sup>1954</sup> is expressed as a diagonalised time-dependent solution to the schrodinger equation.  
<sup>1955</sup> The  $0^{th}$  layer is the propagation through the atmosphere and is the only term which  
<sup>1956</sup> depends on the production height. Using the substitution  $t_0 = t(\bar{h}) - \delta t(h)$ , it can be  
<sup>1957</sup> shown that

$$D_0(t_1, t_0) = D_0(t_1, \bar{h}) D_0(\delta t). \quad (5.9)$$

<sup>1958</sup> Thus Equation 5.7 becomes

$$\begin{aligned}
A(t_{n+1}, t_0) &= D_n(t_{n+1}, t_n) \dots D_1(t_2, t_1) D_0(t_1, \bar{h}) D(\delta t) \\
&= A(t_{n+1}, \bar{h}) \sum_{k=1}^3 C_k \exp[i a_k \delta t], \\
&= \sum_{k=1}^3 B_k \exp[i a_k \delta t].
\end{aligned} \tag{5.10}$$

<sup>1959</sup> The oscillation probability averaged over production height is calculated as

$$\begin{aligned}
\bar{P}(\nu_j \rightarrow \nu_i) &= \int d(\delta t) p_j(\delta t | E_\nu, \cos \theta_Z) P(\nu_j \rightarrow \nu_i) \\
&= \int d(\delta t) p_j(\delta t | E_\nu, \cos \theta_Z) A(t_{n+1}, t_0) A^*(t_{n+1}, t_0) \\
&= \sum_{km} (B_k)_{ij} (B_m)_{ij}^* \int d(\delta t) p_j(\delta t | E_\nu, \cos \theta_Z) \exp[i(a_k - a_m)\delta t]
\end{aligned} \tag{5.11}$$

<sup>1960</sup> In practice, implementation in CUDAProb3 [191] is relatively straightforward as  
<sup>1961</sup> the majority of these terms are already calculated in the standard oscillation calculation.  
<sup>1962</sup> Figure 5.17 illustrates the results of the production height averaging. As expected,  
<sup>1963</sup> the main effect is observed in the low-energy downward-going and horizontal-going  
<sup>1964</sup> events. Upward-going events have to travel the radius of the Earth,  $R_E = 6371\text{km}$ ,  
<sup>1965</sup> where the production height uncertainty is a small fraction of the total path length.

<sup>1966</sup>

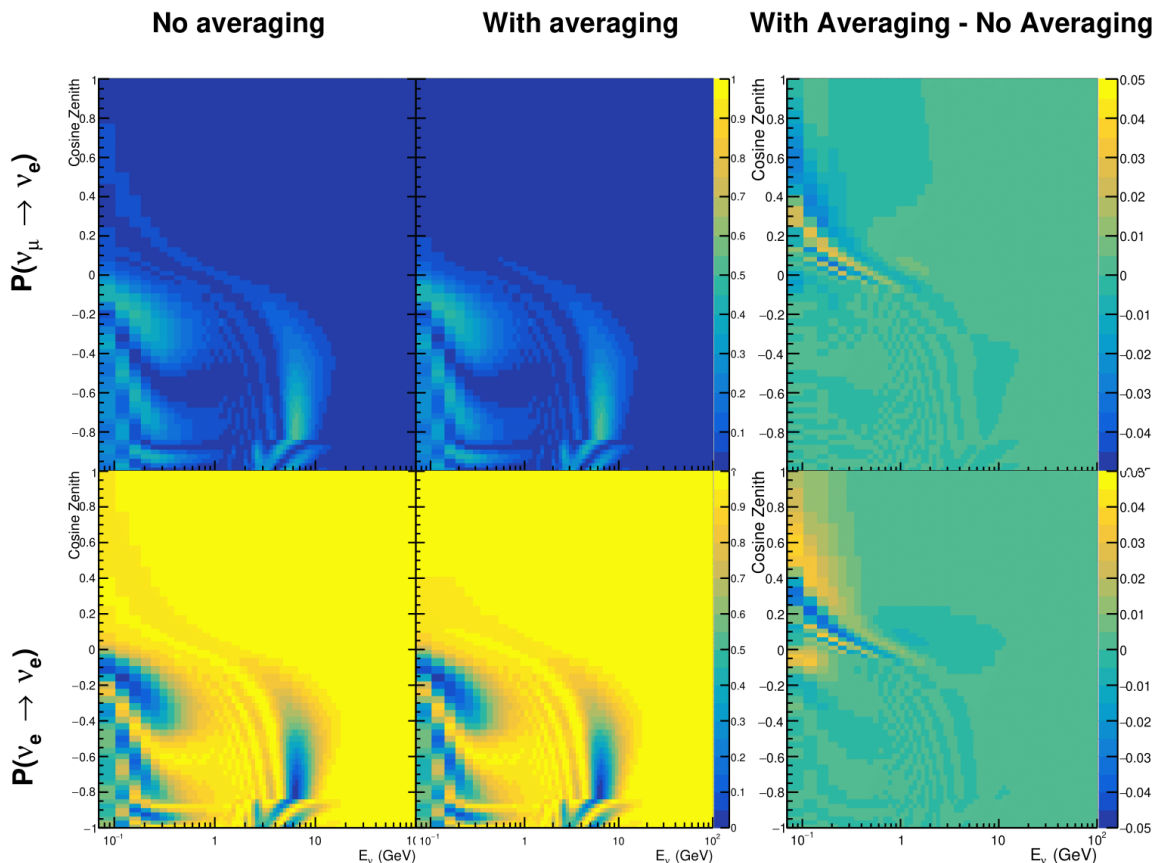


**Figure 5.17:** The oscillation probability,  $P(\nu_\mu \rightarrow \nu_e)$  (top row) and  $P(\nu_e \rightarrow \nu_\mu)$  (bottom row), given as a function of neutrino energy and zenith angle. The left column gives probabilities where a fixed production height of 25km is used. The middle column gives the probabilities where the production height is analytically averaged. The right column illustrates the difference in oscillation probability between the two different techniques.

# <sup>1967</sup> Bibliography

- <sup>1968</sup> [1] J. Chadwick, Verhandl. Dtsc. Phys. Ges. **16**, 383 (1914).
- <sup>1969</sup> [2] C. D. Ellis and W. A. Wooster, Proc. R. Soc. Lond. A Math. Phys. Sci. **117**, 109 (1927).
- <sup>1970</sup>
- <sup>1971</sup> [3] W. Pauli, Phys. Today **31N9**, 27 (1978).
- <sup>1972</sup> [4] E. Fermi, Z. Phys. **88**, 161 (1934).
- <sup>1973</sup> [5] F. Reines and C. L. Cowan, Phys. Rev. **92**, 830 (1953).
- <sup>1974</sup> [6] C. L. Cowan, F. Reines, F. B. Harrison, H. W. Kruse, and A. D. McGuire, Science **124**, 103 (1956), <http://science.sciencemag.org/content/124/3212/103.full.pdf>.
- <sup>1975</sup>
- <sup>1976</sup> [7] G. Danby *et al.*, Phys. Rev. Lett. **9**, 36 (1962).
- <sup>1977</sup> [8] K. Kodama *et al.*, Physics Letters B **504**, 218 (2001).
- <sup>1978</sup> [9] LSND, A. Aguilar-Arevalo *et al.*, Phys. Rev. **D64**, 112007 (2001), hep-ex/0104049.
- <sup>1979</sup> [10] MiniBooNE Collaboration, A. A. Aguilar-Arevalo *et al.*, Phys. Rev. Lett. **110**, 161801 (2013).
- <sup>1980</sup>
- <sup>1981</sup> [11] Planck Collaboration *et al.*, aap **641** (2020).
- <sup>1982</sup> [12] The ALEPH Collaboration, The Delphi Collaboration, The L3 Collaboration, The SLD Collaboration, The LEP Electroweak Working Group, The SLD Electroweak and Heavy Flavour Groups, J. A. Bagger *et al.*, Physics Reports **427**, 257 (2006).
- <sup>1983</sup>
- <sup>1984</sup>
- <sup>1985</sup> [13] B. Pontecorvo, Sov. Phys. JETP **26**, 984 (1968), [Zh. Eksp. Teor. Fiz. 53, 1717 (1967)].
- <sup>1986</sup> [14] B. Pontecorvo, Sov. Phys. JETP **7**, 172 (1958), [Zh. Eksp. Teor. Fiz. 34, 247 (1957)].
- <sup>1987</sup> [15] M. Kobayashi and T. Maskawa, Progress of Theoretical Physics **49**, 652 (1973).
- <sup>1988</sup> [16] N. Cabibbo, Phys. Rev. Lett. **10**, 531 (1963).
- <sup>1989</sup> [17] A. M. and, Journal of Physics: Conference Series **587**, 012030 (2015).
- <sup>1990</sup> [18] A. Y. Smirnov, (2003).
- <sup>1991</sup> [19] S. Mikheyev and A. Smirnov, Soviet Journal of Nuclear Physics **42**, 913 (1985).

- 1992 [20] L. Wolfenstein, Phys. Rev. D **17**, 2369 (1978).
- 1993 [21] V. D. Barger, K. Whisnant, S. Pakvasa, and R. J. N. Phillips, Phys. Rev. D **22**, 2718  
1994 (1980).
- 1995 [22] The Super-Kamiokande Collaboration, Y. Ashie *et al.*, Phys. Rev. Lett. **93**, 101801  
1996 (2004).
- 1997 [23] SNO Collaboration, Q. R. Ahmad *et al.*, Phys. Rev. Lett. **89**, 011301 (2002).
- 1998 [24] 2015 Nobel prize in Physics as listed by Nobelprize.org, [https://www.  
1999 nobelprize.org/nobel\\_prizes/physics/laureates/2015/](https://www.nobelprize.org/nobel_prizes/physics/laureates/2015/), Accessed: 22-06-  
2000 2022.
- 2001 [25] J. A. Formaggio and G. P. Zeller, Rev. Mod. Phys. **84**, 1307 (2012), 1305.7513.
- 2002 [26] A. Bellerive, Int. J. Mod. Phys. A **19**, 1167 (2004).
- 2003 [27] R. Davis, D. S. Harmer, and K. C. Hoffman, Phys. Rev. Lett. **20**, 1205 (1968).
- 2004 [28] N. Vinyoles *et al.*, Astrophys. J. **835**, 202 (2017).
- 2005 [29] V. Gribov and B. Pontecorvo, Phys. Lett. B **28**, 493 (1969).
- 2006 [30] K. S. Hirata *et al.*, Phys. Rev. Lett. **63**, 16 (1989).
- 2007 [31] W. Hampel *et al.*, Phys. Lett. B **447**, 127 (1999).
- 2008 [32] SAGE Collaboration, J. N. Abdurashitov *et al.*, Phys. Rev. C **60**, 055801 (1999).
- 2009 [33] Q. R. Ahmad *et al.*, Phys. Rev. Lett. **89** (2002).
- 2010 [34] Borexino Collaboration, Nature **562**, 505 (2018).
- 2011 [35] B. Aharmim *et al.*, Astrophys. J. **653**, 1545 (2006).
- 2012 [36] M. Agostini *et al.*, (2020).
- 2013 [37] S. Andringa *et al.*, Adv. High Energy Phys. **2016**, 1 (2016).
- 2014 [38] J. F. Beacom *et al.*, Chin. phys. C **41**, 023002 (2017).
- 2015 [39] F. An *et al.*, J. Phys. G Nucl. Part. Phys. **43**, 030401 (2016).
- 2016 [40] J. Aalbers *et al.*, (2020), 2006.03114.
- 2017 [41] T. K. Gaisser and M. Honda, (2002).

- 2018 [42] G. D. Barr, T. K. Gaisser, P. Lipari, S. Robbins, and T. Stanev, Physical Review D **70** (2004).
- 2019 [43] M. Honda, T. Kajita, K. Kasahara, S. Midorikawa, and T. Sanuki, Physical Review D **75** (2007).
- 2020 [44] M. Honda, T. Kajita, K. Kasahara, and S. Midorikawa, Phys. Rev. D **70**, 043008 (2004).
- 2021 [45] M. Honda, T. Kajita, K. Kasahara, and S. Midorikawa, Phys. Rev. D **83**, 123001 (2011).
- 2022 [46] A. Fasso, A. Ferrari, P. R. Sala, and J. Ranft, (2001).
- 2023 [47] Y. Ashie *et al.*, Physical Review D **71** (2005).
- 2024 [48] F. Reines *et al.*, Phys. Rev. Lett. **15**, 429 (1965).
- 2025 [49] D. Casper *et al.*, Phys. Rev. Lett. **66**, 2561 (1991).
- 2026 [50] K. S. Hirata *et al.*, Phys. Lett. B **280**, 146 (1992).
- 2027 [51] Z. Li *et al.*, Physical Review D **98** (2018).
- 2028 [52] Kamiokande Collaboration *et al.*, (2017).
- 2029 [53] T2K Collaboration, Nature **580**, 339 (2020).
- 2030 [54] M. A. Acero *et al.*, Phys. Rev. Lett. **123**, 151803 (2019).
- 2031 [55] M. G. Aartsen *et al.*, Phys. Rev. Lett. **120** (2018).
- 2032 [56] P. Adamson *et al.*, Phys. Rev. Lett. **112** (2014).
- 2033 [57] M. S. Athar *et al.*, Progress in Particle and Nuclear Physics **124**, 103947 (2022).
- 2034 [58] G. Danby *et al.*, Phys. Rev. Lett. **9**, 36 (1962).
- 2035 [59] K. Abe *et al.*, Physical Review D **87** (2013).
- 2036 [60] MINOS Collaboration, D. G. Michael *et al.*, Phys. Rev. Lett. **97**, 191801 (2006).
- 2037 [61] G. Danby *et al.*, Phys. Rev. Lett. **9**, 36 (1962).
- 2038 [62] NOvA Collaboration, M. A. Acero *et al.*, Phys. Rev. Lett. **123**, 151803 (2019).
- 2039 [63] B. Abi, R. Acciarri, M. A. Acero, and G. e. a. Adamov, Eur. Phys. J. C Part. Fields

- 2044       **80** (2020).
- 2045 [64] Hyper-Kamiokande Proto-Collaboration *et al.*, Prog. Theor. Exp. Phys. **2015**,  
2046       53C02 (2015).
- 2047 [65] C. Blanco, D. Hooper, and P. Machado, Physical Review D **101** (2020).
- 2048 [66] MicroBooNE Collaboration *et al.*, Search for an Excess of Electron Neutrino  
2049       Interactions in MicroBooNE Using Multiple Final State Topologies, 2021.
- 2050 [67] KARMEN Collaboration, B. Armbruster *et al.*, Phys. Rev. D **65**, 112001 (2002).
- 2051 [68] S.-B. Kim, T. Lasserre, and Y. Wang, Adv. High Energy Phys. **2013**, 1 (2013).
- 2052 [69] M. Sajjad Athar *et al.*, Prog. Part. Nucl. Phys. **124**, 103947 (2022), 2111.07586.
- 2053 [70] K. Abe *et al.*, Nucl. Instrum. Methods Phys. Res. A **1027**, 166248 (2022).
- 2054 [71] F. P. An *et al.*, Phys. Rev. Lett. **108**, 171803 (2012).
- 2055 [72] RENO Collaboration, J. K. Ahn *et al.*, Phys. Rev. Lett. **108**, 191802 (2012).
- 2056 [73] Double Chooz Collaboration, Y. Abe *et al.*, Phys. Rev. Lett. **108**, 131801 (2012).
- 2057 [74] J. Collaboration *et al.*, TAO Conceptual Design Report: A Precision Measurement  
2058       of the Reactor Antineutrino Spectrum with Sub-percent Energy Resolution, 2020,  
2059       2005.08745.
- 2060 [75] for the RENO Collaboration, New results from RENO and the 5 MeV excess,  
2061       AIP Publishing LLC, 2015.
- 2062 [76] Y. Abe *et al.*, Journal of High Energy Physics **2014** (2014).
- 2063 [77] Daya Bay Collaboration, D. Adey *et al.*, Phys. Rev. Lett. **123**, 111801 (2019).
- 2064 [78] M. P. Decowski, Nucl. Phys. B. **908**, 52 (2016).
- 2065 [79] The KamLAND Collaboration, A. Gando *et al.*, Phys. Rev. D **83**, 052002 (2011).
- 2066 [80] P. Dunne, Latest Neutrino oscillation results from T2K, 2020.
- 2067 [81] M. Tanabashi *et al.*, Phys. Rev. D. **98** (2018).
- 2068 [82] Particle Data Group, R. L. Workman and Others, PTEP **2022**, 083C01 (2022).
- 2069 [83] Y. Fukuda *et al.*, Phys. Rev. Lett. **81**, 1562 (1998).

- 2070 [84] Linyan Wan, (2022).
- 2071 [85] K. Abe *et al.*, Nuclear Instruments and Methods in Physics Research Section  
2072 A: Accelerators, Spectrometers, Detectors and Associated Equipment **737**, 253  
2073 (2014).
- 2074 [86] S. Fukuda *et al.*, Nucl. Instrum. Methods Phys. Res. A **501**, 418 (2003).
- 2075 [87] Y. Itow *et al.*, (2001).
- 2076 [88] M. Jiang *et al.*, Prog. Theor. Exp. Phys. **2019** (2019).
- 2077 [89] S. Fukuda *et al.*, Nuclear Instruments and Methods in Physics Research Section  
2078 A: Accelerators, Spectrometers, Detectors and Associated Equipment **501**, 418  
2079 (2003), <http://www.sciencedirect.com/science/article/pii/S016890020300425X>.
- 2080 [90] Y. Nakano *et al.*, Nucl. Instrum. Methods Phys. Res. A **977**, 164297 (2020).
- 2081 [91] Hamamatsu, Hamamatsu Photonics Photomultiplier Tubes Handbook.
- 2082 [92] K. Abe *et al.*, Nucl. Instrum. Methods Phys. Res. A **1027**, 166248 (2022).
- 2083 [93] J. F. Beacom and M. R. Vagins, Phys. Rev. Lett. **93**, 171101 (2004).
- 2084 [94] L. Marti *et al.*, Nucl. Instrum. Methods Phys. Res. A **959**, 163549 (2020).
- 2085 [95] L. Marti *et al.*, (2019).
- 2086 [96] M. Vagins, Solar/DSNB Neutrino\_SK-Gd, 2022.
- 2087 [97] T. Tanimori *et al.*, IEEE Transactions on Nuclear Science **36**, 497 (1989).
- 2088 [98] Super-Kamiokande Collaboration, J. Hosaka *et al.*, Phys. Rev. D **73**, 112001  
2089 (2006).
- 2090 [99] H. Nishino *et al.*, Nucl. Instrum. Methods Phys. Res. A **610**, 710 (2009).
- 2091 [100] S. Yamada *et al.*, IEEE Transactions on Nuclear Science **57**, 428 (2010).
- 2092 [101] S. Yamada, Y. Hayato, Y. Obayashi, and M. Shiozawa, New online system  
2093 without hardware trigger for the Super-Kamiokande experiment, in *2007 IEEE*  
2094 *Nuclear Science Symposium Conference Record*, IEEE, 2007.
- 2095 [102] G. Carminati, Phys. Procedia **61**, 666 (2015).
- 2096 [103] P. A. Čerenkov, Phys. Rev. **52**, 378 (1937).

- 2097 [104] I. Frank and I. Tamm, Coherent visible radiation of fast electrons passing  
2098 through matter, in *Selected Papers*, pp. 29–35, Springer Berlin Heidelberg, Berlin,  
2099 Heidelberg, 1991.
- 2100 [105] The T2K Collaboration, KEK Proposal (2001),  
2101 <http://neutrino.kek.jp/jhfnu/loi/loi.v2.030528.pdf>.
- 2102 [106] Y. Itow *et al.*, (2001), hep-ex/0106019.
- 2103 [107] The K2K Collaboration and S. H. Ahn, (2001), hep-ex/0103001.
- 2104 [108] The T2K Collaboration, KEK Proposal (2006), [http://j-parc.jp/researcher/Hadron/en/pac\\_0606/pdf/p11-Nishikawa.pdf](http://j-parc.jp/researcher/Hadron/en/pac_0606/pdf/p11-Nishikawa.pdf).
- 2106 [109] C. Bronner, Accelerator Neutrino I\_Recent results from T2K, 2022.
- 2107 [110] T2K Collaboration, K. Abe *et al.*, Phys. Rev. Lett. **112**, 061802 (2014),  
2108 <https://link.aps.org/doi/10.1103/PhysRevLett.112.061802>.
- 2109 [111] NINJA Collaboration, T. Fukuda *et al.*, Proposal for precise measurement of  
2110 neutrino-water cross-section in NINJA physics run, Proposal for J-PARC and  
2111 KEK, 2017.
- 2112 [112] T. Ovsiannikova *et al.*, Physics of Particles and Nuclei **48**, 1014 (2017),  
2113 <https://doi.org/10.1134/S1063779617060478>.
- 2114 [113] M. Antonova *et al.*, Journal of Instrumentation **12**, C07028 (2017),  
2115 <http://stacks.iop.org/1748-0221/12/i=07/a=C07028>.
- 2116 [114] The T2K Collaboration, K. Abe *et al.*, Phys. Rev. D **102**, 012007 (2020).
- 2117 [115] K. Abe *et al.*, Progress of Theoretical and Experimental Physics **2021** (2021).
- 2118 [116] The T2K Collaboration, K. Abe *et al.*, Nuclear Instruments  
2119 and Methods in Physics Research Section A: Accelerators, Spec-  
2120 trometers, Detectors and Associated Equipment **659**, 106 (2011),  
2121 <http://www.sciencedirect.com/science/article/pii/S0168900211011910>.
- 2122 [117] K. Matsuoka *et al.*, Nuclear Instruments and Methods in Physics Research Section  
2123 A: Accelerators, Spectrometers, Detectors and Associated Equipment **624**, 591  
2124 (2010), <http://www.sciencedirect.com/science/article/pii/S016890021002098X>.
- 2125 [118] K. Abe *et al.*, Phys. Rev. D. **103** (2021).

- [2126] [119] T. Vladisavljevic, *Predicting the T2K neutrino flux and measuring oscillation parameters* Springer theses, 1 ed. (Springer Nature, Cham, Switzerland, 2020).
- [2127]
- [2128] [120] D. Beavis, A. Carroll, and I. Chiang, (1995).
- [2129] [121] P.-A. Amaudruz *et al.*, Nuclear Instruments and Methods in Physics Research Section A: Accelerators, Spectrometers, Detectors and Associated Equipment **696**, 1 (2012).
- [2130]
- [2131]
- [2132] [122] N. Abgrall *et al.*, Nuclear Instruments and Methods in Physics Research Section A: Accelerators, Spectrometers, Detectors and Associated Equipment **637**, 25 (2011).
- [2133]
- [2134]
- [2135] [123] S. Assylbekov *et al.*, Nuclear Instruments and Methods in Physics Research Section A: Accelerators, Spectrometers, Detectors and Associated Equipment **686**, 48 (2012).
- [2136]
- [2137]
- [2138] [124] D. Allan *et al.*, Journal of Instrumentation **8**, P10019 (2013).
- [2139] [125] F. Vannucci, Advances in High Energy Physics **2014**, 1 (2014).
- [2140] [126] UA1 magnet sets off for a second new life, 2022.
- [2141] [127] S. Aoki *et al.*, Nuclear Instruments and Methods in Physics Research Section A: Accelerators, Spectrometers, Detectors and Associated Equipment **698**, 135 (2013).
- [2142]
- [2143]
- [2144] [128] K. Suzuki *et al.*, Progress of Theoretical and Experimental Physics **2015**, 53C01 (2015).
- [2145]
- [2146] [129] S. Brooks, A. Gelman, G. L. Jones, and X.-L. Meng, *Handbook of Markov Chain Monte Carlo* (CRC Press, 2011).
- [2147]
- [2148] [130] W. R. Gilks, S. Richardson, and D. J. Spiegelhalter, *Markov Chain Monte Carlo in Practice* (Chapman & Hall/CRC Interdisciplinary Statistics, 1995).
- [2149]
- [2150] [131] C. Wret, *Minimising systematic uncertainties in the T2K experiment using near-detector and external data*, PhD thesis, Imperial College London, 2018.
- [2151]
- [2152] [132] K. E. Duffy, *Measurement of the Neutrino Oscillation Parameters  $\sin^2 \theta_{23}$ ,  $\Delta m_{32}^2$ ,  $\sin^2 \theta_{13}$ , and  $\delta_{CP}$  in Neutrino and Antineutrino Oscillation at T2K*, PhD thesis, Oriel College, University of Oxford, 2016.
- [2153]
- [2154]

- <sup>2155</sup> [133] T. Bayes, Rev. Phil. Trans. Roy. Soc. Lond. **53**, 370 (1764).
- <sup>2156</sup> [134] N. Metropolis, A. W. Rosenbluth, M. N. Rosenbluth, A. H. Teller, and E. Teller, Journal of Chemical Physics **21** (1970).
- <sup>2158</sup> [135] W. K. Hastings, Biometrika **57** (1970).
- <sup>2159</sup> [136] J. Dunkley, M. Bucher, P. G. Ferreira, K. Moodley, and C. Skordis, Mon. Not. R. Astron. Soc. **356**, 925 (2005).
- <sup>2161</sup> [137] Particle Data Group *et al.*, Prog. Theor. Exp. Phys. **2020** (2020).
- <sup>2162</sup> [138] H. Jeffreys, *The Theory of Probability* Oxford Classic Texts in the Physical Sciences (, 1939).
- <sup>2164</sup> [139] R. E. Kass and A. E. Raftery, J. Am. Stat. Assoc. **90**, 773 (1995).
- <sup>2165</sup> [140] T. Böhlen *et al.*, Nuclear Data Sheets **120**, 211 (2014),  
<sup>2166</sup> <http://www.sciencedirect.com/science/article/pii/S0090375214005018>.
- <sup>2167</sup> [141] R. Brun *et al.*, GEANT: Detector Description and Simulation Tool; Oct 1994CERN Program Library (CERN, Geneva, 1993), <http://cds.cern.ch/record/1082634>, Long Writeup W5013.
- <sup>2170</sup> [142] T2K Collaboration, K. Abe *et al.*, Phys. Rev. D **87**, 012001 (2013).
- <sup>2171</sup> [143] C. Zeitnitz and T. Gabriel, Nuclear Instruments and Methods in Physics Research Section A: Accelerators, Spectrometers, Detectors and Associated Equipment **349**, 106 (1994),  
<sup>2174</sup> <http://www.sciencedirect.com/science/article/pii/0168900294906130>.
- <sup>2175</sup> [144] N. Abgrall *et al.*, Physical Review C **84** (2011).
- <sup>2176</sup> [145] N. Abgrall *et al.*, Physical Review C **85** (2012).
- <sup>2177</sup> [146] N. Abgrall *et al.*, Nuclear Instruments and Methods in Physics Research Section A: Accelerators, Spectrometers, Detectors and Associated Equipment **701**, 99 (2013), <http://www.sciencedirect.com/science/article/pii/S016890021201234X>.
- <sup>2180</sup> [147] HARP Collaboration, M. Apollonio *et al.*, Phys. Rev. C **80**, 035208 (2009),  
<sup>2181</sup> <https://link.aps.org/doi/10.1103/PhysRevC.80.035208>.
- <sup>2182</sup> [148] A. Fiorentini *et al.*, T2K Technical Note **217** (2017).

- <sup>2183</sup> [149] B. Blau *et al.*, Nuclear Physics B - Proceedings Supplements **113**, 125 (2002).
- <sup>2184</sup> [150] S. Haino *et al.*, Physics Letters B **594**, 35 (2004).
- <sup>2185</sup> [151] NASA, U.S. Standard Atmosphere, 1976, 1976.
- <sup>2186</sup> [152] S. Roesler, R. Engel, and J. Ranft, The Monte Carlo Event Generator DPMJET-III, in *Advanced Monte Carlo for Radiation Physics, Particle Transport Simulation and Applications*, pp. 1033–1038, Springer Berlin Heidelberg, 2001.
- <sup>2189</sup> [153] K. Niita *et al.*, Radiation Measurements **41**, 1080 (2006).
- <sup>2190</sup> [154] T. Sanuki *et al.*, Physics Letters B **541**, 234 (2002).
- <sup>2191</sup> [155] P. Achard *et al.*, Physics Letters B **598**, 15 (2004).
- <sup>2192</sup> [156] Y. Hayato and L. Pickering, The European Physical Journal Special Topics **230**, 4469 (2021).
- <sup>2194</sup> [157] Y. Hayato, Acta Physica Polonica B **40** (2009).
- <sup>2195</sup> [158] C. L. Smith, Physics Reports **3**, 261 (1972),  
<sup>2196</sup> <http://www.sciencedirect.com/science/article/pii/0370157372900105>.
- <sup>2197</sup> [159] O. Benhar, A. Fabrocini, and S. Fantoni, Nuclear Physics A **497**, 423 (1989).
- <sup>2198</sup> [160] R. Bradford, A. Bodek, H. Budd, and J. Arrington, Nuclear Physics B - Proceedings Supplements **159**, 127 (2006),  
<sup>2199</sup> <http://www.sciencedirect.com/science/article/pii/S0920563206005184>,  
<sup>2200</sup> Proceedings of the 4th International Workshop on Neutrino-Nucleus Interactions  
<sup>2201</sup> in the Few-GeV Region.
- <sup>2203</sup> [161] A. A. Aguilar-Arevalo *et al.*, Physical Review D **81** (2010).
- <sup>2204</sup> [162] R. Gran, J. Nieves, F. Sanchez, and M. J. V. Vacas, Phys. Rev. D **88**, 113007 (2013),  
<sup>2205</sup> <https://link.aps.org/doi/10.1103/PhysRevD.88.113007>.
- <sup>2206</sup> [163] C. Berger and L. M. Sehgal, Phys. Rev. D **76**, 113004 (2007).
- <sup>2207</sup> [164] C. Berger and L. M. Sehgal, Phys. Rev. D **79**, 053003 (2009),  
<sup>2208</sup> <https://link.aps.org/doi/10.1103/PhysRevD.79.053003>.
- <sup>2209</sup> [165] T. Sjöstrand, Computer Physics Communications **82**, 74 (1994).
- <sup>2210</sup> [166] C. Bronner and M. Hartz, Tuning of the Charged Hadrons Multiplicities for Deep

- <sup>2211</sup> Inelastic Interactions in NEUT, in *Proceedings of the 10th International Workshop on Neutrino-Nucleus Interactions in Few-GeV Region (NuInt15)*, Journal of the Physical Society of Japan, 2016.
- <sup>2214</sup> [167] M. Glück, E. Reya, and A. Vogt, The European Physical Journal C **5**, 461 (1998).
- <sup>2215</sup> [168] A. Bodek and U.-k. Yang, Axial and Vector Structure Functions for Electron- and Neutrino- Nucleon Scattering Cross Sections at all  $Q^2$  using Effective Leading order Parton Distribution Functions, 2010.
- <sup>2218</sup> [169] A. Bodek and U.-K. Yang, (2010).
- <sup>2219</sup> [170] S. Gollapinni, (2016).
- <sup>2220</sup> [171] E. S. P. Guerra *et al.*, Phys. Rev. D **99**, 052007 (2019).
- <sup>2221</sup> [172] GEANT4, S. Agostinelli *et al.*, Nucl. Instrum. Meth. **A506**, 250 (2003).
- <sup>2222</sup> [173] R. Brun, F. Bruyant, M. Maire, A. C. McPherson, and P. Zanarini, (1987).
- <sup>2223</sup> [174] K. Abe *et al.*, Physical Review Letters **121** (2018).
- <sup>2224</sup> [175] K. Abe *et al.*, Physical Review D **91** (2015).
- <sup>2225</sup> [176] R. Patterson *et al.*, Nuclear Instruments and Methods in Physics Research Section A: Accelerators, Spectrometers, Detectors and Associated Equipment **608**, 206 (2009).
- <sup>2228</sup> [177] e. a. S. Berkman, T2K Technical Note **146** (2013).
- <sup>2229</sup> [178] e. a. A. Himmel, T2K Technical Note **219** (2015).
- <sup>2230</sup> [179] F. a. James, (1998), CERN Program Library Long Writeups.
- <sup>2231</sup> [180] e. a. D. Barrow, T2K Technical Note **326** (2020).
- <sup>2232</sup> [181] A. Maghrabi, A. Aldosari, and M. Almutairi, Advances in Space Research **68**, 2941 (2021).
- <sup>2234</sup> [182] Super-Kamiokande Collaboration, K. Abe *et al.*, Phys. Rev. D **97**, 072001 (2018), <https://link.aps.org/doi/10.1103/PhysRevD.97.072001>.
- <sup>2236</sup> [183] Particle Data Group, J. Beringer *et al.*, Phys. Rev. D **86**, 010001 (2012).
- <sup>2237</sup> [184] Y. N. and, Journal of Physics: Conference Series **888**, 012191 (2017).

- 2238 [185] M. Jiang, *Study of the neutrino mass hierarchy with the atmospheric neutrino data*  
2239       *collected in Super-Kamiokande IV*, PhD thesis, Kyoto University, 2019.
- 2240 [186] P. Machado, H. Schulz, and J. Turner, Physical Review D **102** (2020).
- 2241 [187] T2K Collaboration, K. Abe *et al.*, Phys. Rev. Lett. **112**, 181801 (2014).
- 2242 [188] R. Wendell, *Three Flavor Oscillation Analysis of Atmospheric Neutrinos in Super-*  
2243       *Kamiokande*, PhD thesis, University of North Carolina, 2008.
- 2244 [189] R. G. Calland, A. C. Kaboth, and D. Payne, **9**, P04016 (2014).
- 2245 [190] R. Wendell, <http://www.phy.duke.edu/raw22/public/Prob3++/>.
- 2246 [191] F. Kallenborn, C. Hundt, S. Böser, and B. Schmidt, Computer Physics Communi-  
2247       cations **234**, 235 (2019).
- 2248 [192] L. Warsame, MaCh3 Analysis Progress.
- 2249 [193] A. M. Dziewonski and D. L. Anderson, Phys. Earth Planet. Inter. **25**, 297 (1981).
- 2250 [194] S. Bourret, J. A. B. Coelho, and V. V. E. and, Journal of Physics: Conference Series  
2251       **888**, 012114 (2017).
- 2252 [195] C. Rott, A. Taketa, and D. Bose, Scientific Reports **5** (2015).
- 2253 [196] K. Hagiwara, N. Okamura, and K. ichi Senda, Journal of High Energy Physics  
2254       **2011** (2011).
- 2255 [197] D. Typinski, Earth Gravity, [http://www.typnet.net/Essays/  
2256       EarthGravGraphics/EarthGrav.pdf](http://www.typnet.net/Essays/EarthGravGraphics/EarthGrav.pdf), Accessed: 24-06-2022.
- 2257 [198] e. a. D. Barrow, T2K Technical Note **425** (2022).

# <sup>2258</sup> List of Figures

<sup>2259</sup>	1.1	The cross-section of neutrinos from various natural and man-made sources as a function of neutrino energy. Taken from [25] . . . . .	10
<sup>2260</sup>			
<sup>2261</sup>	1.2	The solar neutrino flux as a function of neutrino energy for various fusion reactions and decay chains as predicted by the Standard Solar Model. Taken from [26]. . . . .	11
<sup>2262</sup>			
<sup>2263</sup>			
<sup>2264</sup>	1.3	Left panel: The atmospheric neutrino flux for different neutrino flavours as a function of neutrino energy as predicted by the 2007 Honda model (“This work”) [43], the 2004 Honda model (“HKKM04”) [44], the Bartol model [42] and the FLUKA model [46]. Right panel: The ratio of the muon to electron neutrino flux as predicted by all the quoted models. Both figures taken from [43]. . . . .	13
<sup>2265</sup>			
<sup>2266</sup>			
<sup>2267</sup>			
<sup>2268</sup>			
<sup>2269</sup>			
<sup>2270</sup>	1.4	A diagram illustrating the definition of zenith angle as used in the Super Kamiokande experiment [47]. . . . .	13
<sup>2271</sup>			
<sup>2272</sup>	1.5	Prediction of $\nu_e, \bar{\nu}_e, \nu_\mu, \bar{\nu}_\mu$ fluxes as a function of zenith angle as calculated by the HKKM model [45]. The left, middle and right panels represent three values of neutrino energy, 0.32GeV, 1.0GeV and 3.2GeV respectively. Predictions for other models including Bartol [42], Honda [43] and FLUKA [46] are given in [47]. . . . .	14
<sup>2273</sup>			
<sup>2274</sup>			
<sup>2275</sup>			
<sup>2276</sup>			
<sup>2277</sup>	1.6	Constraints on the atmospheric oscillation parameters, $\sin^2(\theta_{23})$ and $\Delta m_{23}^2$ , from atmospheric and long baseline experiments: SK [52], T2K [53], NO $\nu$ A [54], IceCube [55] and MINOS [56]. Figure taken from [57].	15
<sup>2278</sup>			
<sup>2279</sup>			
<sup>2280</sup>	1.7	Reactor electron antineutrino fluxes for $^{235}\text{U}$ (Black), $^{238}\text{U}$ (Green), $^{239}\text{Pu}$ (Purple), and $^{241}\text{Pu}$ (Orange) isotopes. The inverse $\beta$ -decay cross-section (Blue) and corresponding measurable neutrino spectrum (Red) are also given. Top panel: Schematic of Inverse $\beta$ -decay interaction including the eventual capture of the emitted neutron. This capture emits a $\gamma$ -ray which provides a second signal of the event. Taken from [69]. . . . .	18
<sup>2281</sup>			
<sup>2282</sup>			
<sup>2283</sup>			
<sup>2284</sup>			
<sup>2285</sup>			
<sup>2286</sup>	2.1	A schematic diagram of the Super-Kamiokande Detector. Taken from [87].	24

2287	2.2	The location of “standard PMTs” (red) inside the SK detector. Taken from [85]. . . . .	28
2288			
2289	2.3	Schematic view of the data flow through the data acquisition and online system. Taken from [100]. . . . .	31
2290			
2291	2.4	The cross-section view of the Tokai to Kamioka experiment illustrating the beam generation facility at J-PARC, the near detector situated at a baseline of 280m and the Super Kamiokande far detector situated 295km from the beam target. . . . .	35
2292			
2293			
2294			
2295	2.5	The near detector suite for the T2K experiment showing the ND280 and INGRID detectors. The distance between the detectors and the beam target is 280m. . . . .	36
2296			
2297			
2298	2.6	Top panel: Bird’s eye view of the most relevant part of primary and secondary beamline used within the T2K experiment. The primary beamline is the main-ring proton synchrotron, kicker magnet, and graphite target. The secondary beamline consists of the three focusing horns, decay volume, and beam dump. Figure taken from [116]. Bottom panel: The side-view of the secondary beamline including the focusing horns, beam dump and neutrino detectors. Figure taken from [117]. . . . .	37
2299			
2300			
2301			
2302			
2303			
2304			
2305	2.7	The Monte Carlo prediction of the energy spectrum for each flavour of neutrino ( $\nu_e$ , $\bar{\nu}_e$ , $\nu_\mu$ and $\bar{\nu}_\mu$ ) in the neutrino dominated beam FHC mode (Left) and antineutrino dominated beam RHC mode (Right) expected at SK. Taken from [118]. . . . .	39
2306			
2307			
2308			
2309	2.8	Top panel: T2K muon neutrino disappearance probability as a function of neutrino energy. Middle panel: T2K electron neutrino appearance probability as a function of neutrino energy. Bottom panel: The neutrino flux distribution for three different off-axis angles (Arbitrary units) as a function of neutrino energy. . . . .	40
2310			
2311			
2312			
2313			
2314	2.9	The components of the ND280 detector. The neutrino beam travels from left to right. Taken from [116]. . . . .	41
2315			
2316	2.10	Comparison of data to Monte Carlo prediction of integrated deposited energy as a function of track length for particles that stopped in FGD1. Taken from [121]. . . . .	43
2317			
2318			

2319	2.11 Schematic design of a Time Projection Chamber detector. Taken from [122].	44
2320	2.12 The distribution of energy loss as a function of reconstructed momentum for charged particles passing through the TPC, comparing data to Monte Carlo prediction. Taken from [122].	45
2321		
2322		
2323	2.13 A schematic of the P0D side-view. Taken from [123].	46
2324	2.14 Left panel: The Interactive Neutrino GRID on-axis Detector. 14 modules are arranged in a cross-shape configuration, with the center modules being directly aligned with the on-axis beam. Right panel: The layout of a single module of the INGRID detector. Both figures are recreated from [116].	49
2325		
2326		
2327		
2328		
2329	3.1 Example of using Monte Carlo techniques to find the area under the blue line. The gradient and intercept of the line are 0.4 and 1.0 respectively. The area found to be under the curve using one thousand samples is 29.9 units.	54
2330		
2331		
2332		
2333	3.2 The area under a line of gradient 0.4 and intercept 1.0 for the range $0 \leq x \leq 10$ as calculated using Monte Carlo techniques as a function of the number of samples used in each repetition. The analytical solution to the area is 30 units as given by the red line.	55
2334		
2335		
2336		
2337	3.3 Three MCMC chains, each with a stationary distribution equal to a Gaussian centered at 0 and width 1 (As indicated by the black dotted lines). All of the chains use a Gaussian proposal function but have different widths (or 'step size $\sigma$ '). The top panel has $\sigma = 0.1$ , middle panel has $\sigma = 0.5$ and the bottom panel has $\sigma = 5.0$ .	60
2338		
2339		
2340		
2341		
2342	3.4 The log-likelihood from the fit detailed in <a href="#">DB: Link to AsimovA Sensitivity Section</a> as a function of the number of steps accumulated in each fit. Many independent MCMC chains were run in parallel and overlaid on this plot. The red line indicates the $1 \times 10^5$ step burn-in period after which the log-likelihood becomes stable.	61
2343		
2344		
2345		
2346		

2347      3.5	Left: The two dimensional probability distribution for two correlated parameters $x$ and $y$ . The red distribution shows the two dimensional probability distribution when $0 \leq x \leq 5$ . Right: The marginalised probability distribution for the $y$ parameter found when requiring the $x$ to be bound between $-5 \leq x \leq 5$ and $0 \leq x \leq 5$ for the black and red distribution, respectively. . . . .	64
2353      4.1	The NEUT prediction of the $\nu_\mu$ -H <sub>2</sub> O cross-section overlaid on the T2K $\nu_\mu$ flux. The charged current (black, solid) and neutral current (black, dashed) inclusive, charged current quasi-elastic (blue, solid), charged current 2p2h (blue, dashed), charged current single pion production (pink), and charged current multi- $\pi$ and DIS (Purple) cross-sections are illustrated. Taken from [156]. . . . .	71
2359      4.2	Illustration of the various processes which a pion can undergo before exiting the nucleus. Taken from [170]. . . . .	73
2361      4.3	Event displays from Super Kamiokande illustrating the “crisp” ring from a muon and the typically “fuzzier” electron ring. Each pixel represents a PMT and the color scheme denotes the accumulated charge deposited on that PMT. Figures taken from [178]. . . . .	75
2365      4.4	The electron/muon PID separation parameter for all sub-GeV single-ring events in SK-IV. The charged current (CC) component is broken down in four flavours of neutrino ( $\nu_\mu, \bar{\nu}_\mu, \nu_e$ and $\bar{\nu}e$ ). Events with positive values of the parameter are determined to be electron-like. . . . .	79
2369      4.5	The variation of the measured dark rate as a function of date, broken down by PMT type. The SK-IV and SK-V periods span September 2008 to May 2018 and January 2019 to July 2020 respectively. The break in measurement between 2018 corresponds to the period of tank repair and refurbishment. Figure adapted from [180]. . . . .	81
2374      4.6	Comparison of the measured raw charge deposited per event from the stopping muon data samples between SK-IV (Blue) and SK-V (Red), split by the primary muon subevent and the associated decay electron subevent. . . . .	82

2378	4.7	The distribution of the reconstructed momentum from the muon ring divided by the distance between the reconstructed muon and decay elec- tron vertices as found in the stopping muon data sets of SK-IV (Black) and SK-IV (Red). Only events with one tagged decay electron and con- sidered. A Gaussian fit is considered in the range [2.0, 2.4] MeV/cm and illustrated as the solid curve. . . . .	83
2384	4.8	The $\chi^2$ difference between the SK-IV and SK-V reconstructed muon momentum divided by range when the SK-V is modified by the scaling parameter $\alpha$ . Both additive (Blue) and multiplicative (Black) scaling factors have been considered. In practice, the additive scaling factor actually uses the value of $(\alpha - 1.0)$ . . . . .	84
2389	4.9	A depiction of the topology patterns for fully-contained (FC), partially- contained (PC) and up-going muon (Up- $\mu$ ) samples included in this analysis. . . . .	85
2392	4.10	The predicted neutrino flux of the fully contained (FC) sub-GeV and multi-GeV, partially contained (PC) and upward-going muon (Up- $\mu$ ) events. The prediction is broken down by the $\nu_x \rightarrow \nu_e$ prediction (top left), $\nu_x \rightarrow \nu_\mu$ prediction (top right) and $\nu_x \rightarrow \nu_\tau$ prediction (bottom). All systematic dials are set to their nominal values and the Asimov A oscillation parameters are assumed. . . . .	87
2398	5.1	An “Oscillogram” that depicts the $P(\nu_\mu \rightarrow \nu_e)$ oscillation probability as a function of neutrino energy and cosine of the zenith angle. The zenith angle is defined such that $\cos(\theta_Z) = 1.0$ represents neutrinos that travel from directly above the detector. The four-layer constant density PREM model approximation is used and Asimov A oscillation parameters are assumed. . . . .	91
2404	5.2	The effect of $\delta_{CP}$ for atmospheric neutrinos given in terms of the neu- trino energy and zenith angle. The oscillogram compares the $P(\nu_\mu \rightarrow \nu_e)$ oscillation probability for a CP conserving ( $\delta_{CP} = 0.0$ ) and CP violating ( $\delta_{CP} = -1.601$ ) value of $\delta_{CP}$ . The other oscillation parameters assume the “Asimov A” oscillation parameter set given in Table 5.1. . . . .	93

2409      5.3	An illustration of the matter-induced effects on the oscillation probability, given as a function of neutrino energy and zenith angle. The top row 2410 of panels gives the $P(\nu_e \rightarrow \nu_e)$ oscillation probability and the bottom 2411 row illustrates the $P(\bar{\nu}_e \rightarrow \bar{\nu}_e)$ oscillation probability. The left column 2412 highlights the oscillation probability in a vacuum, whereas the middle 2413 and right column represents the oscillation probabilities when the four 2414 layer fixed density PREM model is assumed. All oscillation probabilities 2415 assume the “Asimov A” set given in Table 5.1, but importantly, the right 2416 column sets an inverted mass hierarchy. The “matter resonance” effects 2417 at $E_\nu \sim 5\text{GeV}$ can be seen in the $P(\nu_e \rightarrow \nu_e)$ for normal mass hierarchy 2418 and $P(\bar{\nu}_e \rightarrow \bar{\nu}_e)$ for inverted hierarchy. . . . .	94
2420      5.4	The oscillation probability for beam neutrino events given as a function 2421 of neutrino energy. All oscillation parameters assume the “Asimov A” 2422 set given in Table 5.1 unless otherwise stated. Each panel represents a 2423 change in one of the oscillation parameters whilst keeping the remaining 2424 parameters fixed. . . . .	95
2425      5.5	The number of electron-like events in the FHC and RHC operating 2426 mode of the beam, as a function of the oscillation probabilities. Both 2427 normal hierarchy (Solid) and inverse hierarchy (Dashed) values of 2428 $\Delta m_{23}^2$ are given. . . . .	96
2429      5.6	The oscillation probability $P(\nu_\mu \rightarrow \nu_e)$ , given as a function of neutrino 2430 energy and zenith angle, which highlights an example of the “fast” 2431 oscillations in the sub-GeV upgoing region. . . . .	98
2432      5.7	Illustration of the averaging procedure for $N = 2$ . The oscillation 2433 probabilities calculated on the finer left binning are averaged to obtain 2434 the oscillation probabilities in the coarser right binning. These averaged 2435 oscillation probabilities with the coarser binning are then applied to 2436 each event during the fit. . . . .	100
2437      5.8	Event rate of the SubGeV_elike_0dcy sample as a function of the num- 2438 ber of sub-divisions per coarse bin. Each subplot represents the event 2439 rate of the sample at a different oscillation parameter set (thrown from 2440 the PDG priors). The red line in each subplot represents the mean of the 2441 event rate over the different values of sub-divisions for that particular 2442 oscillation parameter throw. . . . .	102

2443	5.9	Variance of event rate for each atmospheric sample as a function of the number of sub-divisions per coarse bin. The solid red line indicates the 0.1% threshold and the dashed red line is a graphical indication of the variance at a sub-division $N = 10$ . . . . .	103
2444			
2445			
2446			
2447	5.10	Variance of sample likelihood, when compared to ‘Asimov data’ set at Asimov A, for each atmospheric sample as a function of the number of sub-divisions per coarse bin. The solid red line indicates the 0.1% threshold and the dashed red line is a graphical indication of the variance at a sub-division $N = 10$ . . . . .	104
2448			
2449			
2450			
2451			
2452	5.11	The oscillation probability, $P(\nu_\mu \rightarrow \nu_e)$ (top row) and $P(\nu_e \rightarrow \nu_e)$ (bottom row), given as a function of neutrino energy and zenith angle. The left column gives the “fine” binning used to calculate the oscillation probabilities and the right column illustrates the “coarse” binning used to reweight the MC events. The fine binning choice is given with $N = 10$ , which was determined to be below threshold from Figure 5.9 and Figure 5.10. . . . .	105
2453			
2454			
2455			
2456			
2457			
2458			
2459	5.12	The calculation time taken to both calculate the oscillation probabilities and fill the “coarse” oscillograms, following the technique given in section 5.2, for the CUDAProb3 and ProbGPU (Red) calculation engines. CUDAProb3 has both a GPU (Blue) and CPU (Black) implementation, where the CPU implementation is multithreaded. Therefore, 8-threads (solid) and 40-threads (dashed) configurations have been used. Prob3, which is a CPU single-thread implementation has a mean step time of 1.142s. . . . .	107
2460			
2461			
2462			
2463			
2464			
2465			
2466			
2467	5.13	The density of the Earth given as a function of the radius, as given by the PREM model (Black) and the constant density four-layer approximation (Blue), as used in the official SK-only analysis. . . . .	108
2468			
2469			

2470	5.14 The oscillation probability, $P(\nu_\mu \rightarrow \nu_e)$ (top row) and $P(\nu_e \rightarrow \nu_e)$ (bottom row), given as a function of neutrino energy and zenith angle. The left column gives probabilities where the constant $Z/A = 0.5$ approximation which is used in the official SK-only analysis. The middle column gives the probabilities where the more accurate $Z/A = [0.468, 0.498]$ values as given in Table 5.2. The right column illustrates the difference in oscillation probability between the two different techniques. . . . .	110
2478	5.15 The density of the Earth given as a function of the radius, as given by the PREM model (Black), the constant density four-layer approximation (Blue), as used in the official SK-only analysis, and the quadratic approximation of the PREM model (Red). . . . .	111
2482	5.16 The oscillation probability, $P(\nu_\mu \rightarrow \nu_e)$ (top row) and $P(\nu_e \rightarrow \nu_e)$ (bottom row), given as a function of neutrino energy and zenith angle. The left column gives probabilities where the four-layer constant density approximation is used. The middle column gives the probabilities where the density is integrated over the trajectory, using the quadratic PREM approximation, for each $\cos(\theta_Z)$ is used. The right column illustrates the difference in oscillation probability between the two different techniques.	113
2489	5.17 The oscillation probability, $P(\nu_\mu \rightarrow \nu_e)$ (top row) and $P(\nu_e \rightarrow \nu_e)$ (bottom row), given as a function of neutrino energy and zenith angle. The left column gives probabilities where a fixed production height of 25km is used. The middle column gives the probabilities where the production height is analytically averaged. The right column illustrates the difference in oscillation probability between the two different techniques.	117

# <sup>2495</sup> List of Tables

<sup>2496</sup>	1.1	The 2018 Particle Data Group constraints of the oscillation parameters taken from [81]. The value of $\Delta m_{23}^2$ is given for both normal hierarchy (N.H.) and inverted hierarchy (I.H.) and $\sin^2(\theta_{23})$ is broken down by whether its value is below (Q1) or above (Q2) 0.5. . . . .	20
<sup>2500</sup>	2.1	The various SK periods and respective live-time. The SK-VI live-time is calculated until 1 <sup>st</sup> April 2022. SK-VII started during the writing of this thesis. . . . .	23
<sup>2503</sup>	2.2	The trigger thresholds and extended time windows saved around an event which were utilised throughout the SK-IV period. The exact thresholds can change and the values listed here represent the thresholds at the start and end of the SK-IV period. . . . .	32
<sup>2507</sup>	2.3	The threshold momentum and energy for a particle to generate Cherenkov light in ultrapure water, as calculated in Equation 2.2 in ultrapure water which has refractive index $n = 1.33$ . . . . .	33
<sup>2510</sup>	3.1	Jeffreys scale for strength of preference for two models $A$ and $B$ as a function of the calculated Bayes factor ( $B_{AB} = B(A/B)$ ) between the two models [138]. The original scale is given in terms of $\log_{10}(B(A/B))$ but converted to linear scale for easy comparison throughout this thesis.	66
<sup>2514</sup>	5.1	Reference values of the neutrino oscillation parameters for two different oscillation parameter sets. . . . .	96
<sup>2516</sup>	5.2	Description of the four layers of the Earth invoked within the average constant density approximation of the PREM model [193]. . . . .	108
<sup>2518</sup>	5.3	The quadratic polynomial fits to the PREM model for four assumed layers of the PREM model. The fit to calculate the coefficients is given in [198], where $x = R/R_{Earth}$ . . . . .	111